Wavefront Sensing and Phase Retrieval for Astronomical Imaging

Richard M. Clare, B.E.(Hons. I)

Department of Electrical and Computer Engineering

A thesis presented for the degree of
Doctor of Philosophy

University of Canterbury
Christchurch, New Zealand
September 2004

STATEMENT OF ORIGINALITY

This thesis contains no material which has been accepted for the award of any other degree or diploma in any tertiary institution. To the best of my knowledge and belief, the thesis contains no material previously published or written by another person, except when due reference is made in the text.

Richard Clare

The star

Twinkle, twinkle, little star,
How I wonder what you are!
Up above the world so high,
Like a diamond in the sky.

When the blazing sun is gone,
When he nothing shines upon,
Then you show your little light,
Twinkle, twinkle, all the night.

Then the trav'ller in the dark,
Thanks you for your tiny spark,
He could not see which way to go,
If you did not twinkle so.

In the dark blue sky you keep,
And often thro' my curtains peep,
For you never shut your eye,
Till the sun is in the sky.

'Tis your bright and tiny spark,
Lights the trav'ller in the dark:
Tho' I know not what you are,
Twinkle, twinkle, little star.

Ann and Jane Taylor (1806).

Abstract

Images of astronomical objects captured by ground-based telescopes are distorted by the earth's atmosphere. The atmosphere consists of random time-varying layers of air of differing density and hence refractive index. These refractive index fluctuations cause wavefronts that propagate through the atmosphere to become aberrated, resulting in a loss in resolution of the astronomical images.

The wavefront aberrations that are induced by the atmosphere can be compensated by either real-time adaptive optics, where a deformable mirror is placed in the optical path, or by computer post-processing algorithms on the distorted images. In an adaptive optics system, the wavefront sensor is the element that estimates the wavefront phase aberration. The wavefront cannot be measured directly, and instead an aberration is introduced to the optical path to produce two or more intensity distributions, from which the wavefront slope or curvature can be estimated. Wavefront sensing is one of the topics of this thesis. A number of computer post-processing algorithms exist to deblur astronomical images, such as phase diversity, deconvolution from wavefront sensing (DWFS) and phase retrieval, with improvements to the latter two published in this thesis.

The pyramid wavefront sensor consists of a four-sided glass prism placed in the focal plane of the telescope, which subdivides the focal plane in four, and a relay lens which re-images the four sections of the focal plane to form four images of the aperture at the conjugate aperture plane. The wavefront slope is estimated as a linear combination of the aperture images. The pyramid sensor can be generalised to a class of N-sided glass prism wavefront sensors that subdivide the focal plane into N equal sections, forming N aperture images at the conjugate aperture plane. The minimum number of sides required to estimate the slope in two orthogonal directions is three, and the cone sensor is derived by letting N tend to infinity. Simulation results show that in the presence of photon, but not read, noise the cone sensor provides the best wavefront estimate.

For the pyramid sensor, the wavefront is typically reconstructed from the estimate of the wavefront slope in two orthogonal directions. Some information is inherently lost when

the four measurements (aperture images) are reduced to two slope estimates. A new method is proposed to reconstruct the wavefront directly from the aperture images, removing the intermediate step of forming the slope estimates. Reconstructing the wavefront directly from the images is shown through simulation of atmospheric phase screens to give a better wavefront estimate than reconstructing from the slope estimates. This result is true for all pyramid type sensors tested.

The pyramid wavefront sensor can be generalised by placing the lenslet array at the focal plane to subdivide the complex field in the focal plane into more than four sections. Using this framework, the pyramid sensor can be considered as the dual of the Shack-Hartmann sensor, which subdivides the aperture plane with a lenslet array, since the two sensors subdivide each one of a Fourier pair. Both sensors estimate the wavefront slope with a centroid operator on the low resolution images. Also, in both sensors there exists a trade-off between the spatial resolution obtainable and the accuracy of the slope estimates. This trade-off is determined by the size of the lenslets in the array for both sensors, and is inverted between the two sensors. Simulation results run in open loop demonstrate that the lenslet array at the aperture (Shack-Hartmann) and focal (pyramid) planes do provide wavefront estimates of equivalent quality. The lenslet array at the focal plane, however, can be modulated so as to increase its linear range and thus provide a better wavefront estimate than the Shack-Hartmann sensor in open loop simulations.

Phase retrieval is a non-linear iterative technique that is used to recover the phase in the aperture plane from intensity measurements at the focal plane and other constraints. A novel phase retrieval algorithm, which subdivides the focal plane of the telescope with a lenslet array and uses the aperture images formed at the conjugate aperture plane as a magnitude constraint, is proposed. This algorithm is more heavily constrained than conventional phase retrieval or phase retrieval in conjunction with the Shack-Hartmann sensor, with constraints applied at three Fourier planes: the aperture, focal and conjugate aperture planes. The subdivision of the focal plane means that the ambiguity problem that exists in other phase retrieval algorithms between an object $A(x, y)$ and its twin $A^*(x, y)$ is removed, and this is supported by simulation results. Simulation results also show that the performance of the algorithm is dependent on the starting point, and that starting with the linear estimate from the aperture images gives a better wavefront estimate than starting with zero phase.

DWFS is a computer post-processing algorithm that combines the distorted image and wavefront sensing measurements in order to compensate the image for the atmospheric turbulence. An accurate calibration of the reference positions for the centroids of the Shack-Hartmann sensor is essential for an accurate estimate of the wavefront, and hence astronomical object, with DWFS. The conventional method for estimating these reference posi-

tions is to image a laser beam through the Shack-Hartmann lenslet array but not through the atmosphere. An alternative calibration technique is to observe a single bright star and optimise the Strehl ratio with respect to the reference positions. Results using DWFS on data captured at the Observatoire de Lyon show that this new technique can provide wavefront estimates of similar quality as the grid calibration technique, but without the need for a separate calibration laser.

Acknowledgements

I would like to thank my supervisor Richard Lane for his guidance throughout this research. I would also like to acknowledge my associate supervisor Phil Bones for his support.

In 2002 I was fortunate enough to spend three months with the adaptive optics groups at Imperial College, London and the National University of Ireland (NUI), Galway. I would like to thank Richard Lane for the Marsden funding which made this trip possible, and Carl Paterson of Imperial College and Chris Dainty of NUI for making my time in their respective groups enjoyable and productive.

I gratefully acknowledge the New Zealand government through the Foundation for Research, Science and Technology for funding my research with a Bright Future Top Achiever Doctoral scholarship. In particular, the travel and conference allowance has been invaluable, allowing me to present my research to the international research community at SPIE conferences in Seattle (2002), San Diego (2003) and Glasgow (2004), as well as attend the Centre for Adaptive Optics summer school at Santa Cruz in 2003.

I would like to acknowledge Nic Blakely for letting me use his latex style files as a template for this thesis.

Lastly, and most importantly, I would like to thank all my friends and family for keeping me sane these past three years.

Contents

Preface

The resolution of astronomical images captured by ground-based telescopes is limited by atmospheric turbulence. Planar wavefronts of light from astronomical objects become aberrated as they pass through the earth's atmosphere, which consists of random time-varying layers of air of differing density. It is possible to improve the resolution of the telescope by estimating, and then compensating, the wavefront aberrations. The wavefront aberrations can be estimated by either wavefront sensing, which is a set of linear methods, or phase retrieval, which is a set of non-linear iterative algorithms. The aim of this thesis is to give an overview of the current methods of wavefront sensing and phase retrieval, and to outline my original contributions to the field.

I began my doctoral studies in June 2001. My supervisor, Richard Lane, was then on sabbatical at the Observatoire de Lyon, and my initial topic for research was deconvolution from wavefront sensing (DWFS) using data captured with the observatory's one metre telescope. This work on DWFS resulted in two papers, which were presented at the SPIE conferences in Seattle and Hawaii, both in 2002.

The remainder of the work for my Ph.D. has centred on the pyramid wavefront sensor, which is the most recently introduced and least well understood of the geometric wavefront sensors. This research can be divided into three distinct groups.

Firstly, the wavefront sensing characteristics of the pyramid sensor with differing number of sides of the glass prism were investigated. This research was presented at the SPIE conference in San Diego in 2003.

Secondly, the use of a lenslet array at the focal plane, which is physically equivalent to the pyramid at the focal plane, was considered. This work was presented at the IVCNZ conference in Palmerston North in 2003 and at the SPIE conference in Glasgow in 2004, and has been accepted for publication in the Journal of the Optical Society of America A.

Thirdly, the concept of using phase retrieval in conjunction with the pyramid sensor (in the form of a lenslet array) was investigated. This idea was published in Applied Optics in

July 2004.

0.1 Thesis organisation

This thesis has nine chapters; the first four are introductory material required to understand the following four of original research. The final chapter is a conclusion of the novel contributions to the field of astronomical imaging.

The astronomical imaging problem is introduced in Chapter 1. This chapter is intended to be a stand-alone discussion of the distortion of images caused by the atmosphere, and the use of adaptive optics, computer post-processing and space telescopes to overcome these distortions.

The mathematical background and notation required to understand the rest of the thesis is presented in Chapter 2. The properties of the Fourier transform, which underpins all of the work in this thesis, are emphasised.

The physical nature of the atmosphere and its effects on images captured through it are discussed in Chapter 3. In particular, the treatment of the propagation and detection of wavefronts, which is critical to the original material in this thesis, is set out.

In Chapter 4, the current methods for estimating and compensating wavefront aberrations induced by the atmosphere are reviewed. Specifically, this includes a discussion of the building blocks of an adaptive optics system: wavefront sensing and wavefront estimation, deformable mirrors and laser guide stars. Also, the computer post-processing algorithms of deconvolution from wavefront sensing, phase retrieval and phase diversity are introduced.

Chapter 5 discusses this thesis' original contributions to DWFS. A calibration scheme for the Shack-Hartmann sensor that operates entirely in software is shown to give equivalent performance to the current method, which requires a calibration laser. Also, it is shown that when using DWFS on real data, certain modes are more susceptible to noise. This problem can be alleviated by optimising the weighting between the noise and measurement covariance matrices.

In Chapter 6, the pyramid sensor is generalised by placing a lenslet array at the focal plane. This generalisation allows the dual relationship of the pyramid sensor with the Shack-Hartmann sensor, which consists of a lenslet array at the aperture plane, to be shown. The two sensors subdivide each of a Fourier transform pair: the complex field at the aperture plane and the complex field at the focal plane. Simulation results of the lenslet array at

the aperture and focal planes in open loop, but without modulation, show that the two sensors have equivalent performance. However, the lenslet array at the focal plane can be modulated to improve its linear range and thus give a better wavefront estimate than the Shack-Hartmann sensor.

The pyramid sensor, which subdivides the complex field in the focal plane in quadrants, is generalised in Chapter 7 to an entire class of wavefront sensors that subdivide the focal plane into N equal segments. Simulation results show that at high photon counts the cone sensor (with an infinite number of sides) provides the best wavefront estimate. Also in this chapter, a new method for estimating the wavefront for pyramid type sensors is presented. In this method, the wavefront is estimated directly from the aperture images, rather than from the slope estimates, which are also formed from the aperture images. The removal of this intermediate step is shown to improve the wavefront estimate for all pyramid type sensors considered.

In Chapter 8, a novel phase retrieval algorithm that subdivides the focal plane with a lenslet array is proposed. By subdividing the focal plane the twin image stagnation problem, which limits other phase retrieval algorithms, can be overcome.

Chapter 9 is the conclusion, summarising the thesis' original contributions to wavefront sensing and phase retrieval for astronomical imaging.

0.2 Supporting publications

The journal and conference papers that have resulted from the research described in this thesis are listed below in chronological order of submission.

- W. Y. V. Leung, R. M. Clare and R. G. Lane, "Blind deconvolution of speckle images constrained by wavefront sensing data," in *Image reconstruction from incomplete data II*, P. J. Bones, M. A. Fiddy and R. P. Millane, eds., Proceedings of SPIE **4792**, 44-55 (2002).

- R. G. Lane, M. Tallon, E. Thiebaut, and R. M. Clare, "Diffraction limited image restoration by post-compensation from simultaneous speckle and wavefront sensing observations," in *Adaptive optical system technologies II*, P. L. Wizinowich and D. Bonaccini, eds., Proceedings of SPIE **4839**, 1142-1153 (2002).

- R. G. Lane, R. M. Clare and M. A. van Dam, "Statistical wavefront sensing," in *Optics in Astrophysics*, R. Foy ed. (to be published).

- R. M. Clare and R. G. Lane, "Wavefront sensing from spatial filtering at the focal plane," in *Astronomical adaptive optics systems and applications*, R. K. Tyson and M. Lloyd-Hart, eds., Proceedings of SPIE **5169**, 43-54 (2003).

- R. M. Clare and R. G. Lane, "Comparison of wavefront sensing using subdivision at the aperture and focal planes," in Proceedings of Image and Vision Computing New Zealand 2003 (IVCNZ'03), D. G. Bailey ed., 187-192 (2003).
- R. M. Clare and R. G. Lane, "Phase retrieval from subdivision of the focal plane with a lenslet array," Applied Optics **43**, 4080-4087 (2004).
- R. M. Clare and R. G. Lane, "Wavefront sensing from subdivision of the focal plane with a lenslet array," Journal of the Optical Society of America A **22**, 117-125 (2005).
- R. M. Clare and R. G. Lane, "Comparison of wavefront sensing with the Shack-Hartmann and pyramid sensors," in *Advancements in adaptive optics*, D. Bonaccini, B. L. Ellerbroek and R. Ragazzoni, eds., Proceedings of SPIE **5490**, 1211-1222 (2004).
- T. Y. Chew, R. M. Clare and R. G. Lane, "A Cramer-Rao bound analysis of the Shack-Hartmann and pyramid wavefront sensors," in Proceedings of Image and Vision Computing New Zealand 2004 (IVCNZ'04), D. Pairman, H. North and S. McNeill, eds., 227-232 (2004).

Glossary

0.3 Acronyms

CCD	charge-coupled device
CDF	cumulative density function
DFT	discrete Fourier transform
DM	deformable mirror
DSP	digital signal processor
DWFS	deconvolution from wavefront sensing
ER	error reduction
FFT	fast Fourier transform
FT	Fourier transform
FWHM	full width at half maximum
GS	Gerchberg-Saxton
IFT	inverse Fourier transform
ITE	irradiance transport equation
LTI	linear time invariant
LGS	laser guide star
MCAO	multi-conjugate adaptive optics
MEM	micro-electro-mechanical
MTF	magnitude transfer function
MSE	mean-squared error
NGS	natural guide star
OTF	optical transfer function
PDF	probability density function
PSF	point spread function
SNR	signal-to-noise ratio
SPID	speckle imaging by deconvolution
WTE	wavefront transport equation

0.4 Notation

j	$\sqrt{-1}$
$\odot$	convolution operator
$\otimes$	corrrelation operator
$\langle\cdot\rangle$	ensemble average
∞	infinity
$\approx$	approximately equal to
$\sum$	summation
$\mathcal{F}$	Fourier transform
$\lvert\cdot\rvert$	magnitude
$\propto$	proportional to
A^{-1}	inverse of matrix A
A^T	transpose of matrix A
$Pr(x)$	probability that $X = x$
$\lvert$	conditional probability
E[·]	expected value of
Var[·]	variance of
x^*	complex conjugate of x
∇^2	Laplacian
$\hat{x}$	estimate of x

0.5 Commonly used terms

σ^2	variance
D	telescope diameter
r_0	Fried's parameter
λ	wavelength
c	speed of light in a vacuum ($3\times10^8 \mathrm{ms}^{-1}$)
k	wavenumber
Θ	interaction matrix
$U(x)$	Heaviside unit step
$\delta(x)$	Dirac delta function
$\mathrm{sgn}(x)$	sign function
$\mathrm{rect}(x)$	rectangular function
$\mathrm{tri}(x)$	triangular function
$\mathrm{sinc}(x)$	sinc function
(x, y)	coordinates in aperture plane

$(u.v)$	coordinates in focal plane
(ξ, η)	coordinates in conjugate aperture plane
z	propagation distance
f	focal length
r	polar coordinate in aperture plane
ρ	polar coordinate in focal plane
$W(x, y)$	wavefront aberration
$\phi(x, y)$	wavefront phase
$A(x, y)$	generalised aperture function
$P(x, y)$	aperture function (magnitude)
Z_i	Zernike mode i
$I(\xi, \eta)$	aperture image
a	basis coefficients
m	matrix of measurements
$d(u, v)$	measured noisy data
$o(u, v)$	object
$n(u, v)$	additive noise on the measurements
$s(u, v)$	PSF
$g(u, v)$	noise-free data
$D(x, y)$	measured data spectrum
$O(x, y)$	Object spectrum
$\mathcal{H}(x, y)$	OTF

Chapter 1

Introduction

1.1 The astronomical imaging problem

Astronomical objects, such as stars, planets and galaxies, that are imaged by ground-based telescopes are distorted by the earth's atmosphere. Light from an astronomical object propagates through space in spherical wavefronts as shown in Fig. 1.1. The wavefronts travel for light years undisturbed until they reach the earth's atmosphere, where time-varying layers of air of different density cause the wavefronts to become aberrated. These atmosphere induced wavefront aberrations cause the images captured by the ground-based telescope to be randomly blurred versions of the object. This atmospheric turbulence also causes stars to twinkle when viewed with the human eye.

Without atmospheric turbulence, the resolution of an image captured with a telescope is inversely proportional to the diameter of the telescope. The larger the telescope, the better the resolution. However, in the presence of atmospheric turbulence the resolution of the image is limited by the atmosphere to that of a much smaller telescope. Binary stars are often used as a practical test of the achievable resolution. Fig. 1.2(a) shows an aberrated image of a binary star where it is no longer possible to distinguish the two components.

The resolution of astronomical images that have been degraded by the earth's atmosphere can be improved by either real-time adaptive optics or by computer post-processing algorithms. The two individual components of the binary star become clearly identifiable when adaptive optics is employed to correct the turbulence as seen in Fig. 1.2(b). Adaptive optics and computer post-processing of astronomical images are the subject of this thesis.

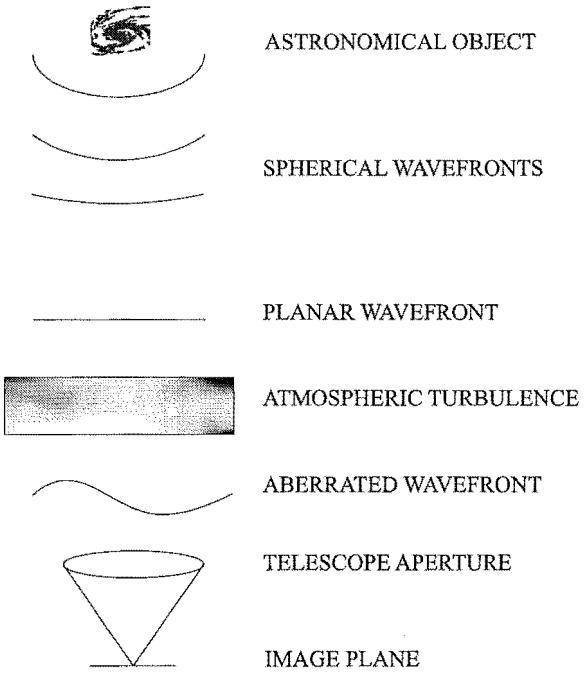

Figure 1.1 The propagation of a wavefront from an astronomical object to a ground-based telescope.

1.2 Solving the astronomical imaging problem

A number of different approaches have been proposed to overcome the astronomical imaging problem. These can be broadly grouped into space telescopes, adaptive optics and computer post-processing algorithms, each of which is discussed in turn in the following subsections. The choice of solution is a trade-off between the budget and required performance of the system.

1.2.1 Space telescopes

The simplest solution conceptually to the problem of the earth's atmosphere distorting astronomical images is to place the telescope in space, above the turbulence. This was first achieved in 1990 with the deployment of the 2.4 m diameter Hubble space telescope by NASA. Although Hubble has provided astronomers with images deeper into the universe (10 billion light years) than ground-based telescopes, it has come at a large financial cost. The construction and deployment of Hubble cost $1.5 billion (US). Hubble also requires regular servicing by astronauts to replace parts and readjust its orbit. The lifetime of a space telescope is also limited, with the Hubble not expected to see out this decade [1].

Hubble's replacement, the James Webb space telescope, which has a 6.5 metre diameter primary mirror, is due to be launched by NASA in 2011. This telescope has a predicted lifetime of ten years and a construction budget of $825 million (US). It is clear, however,

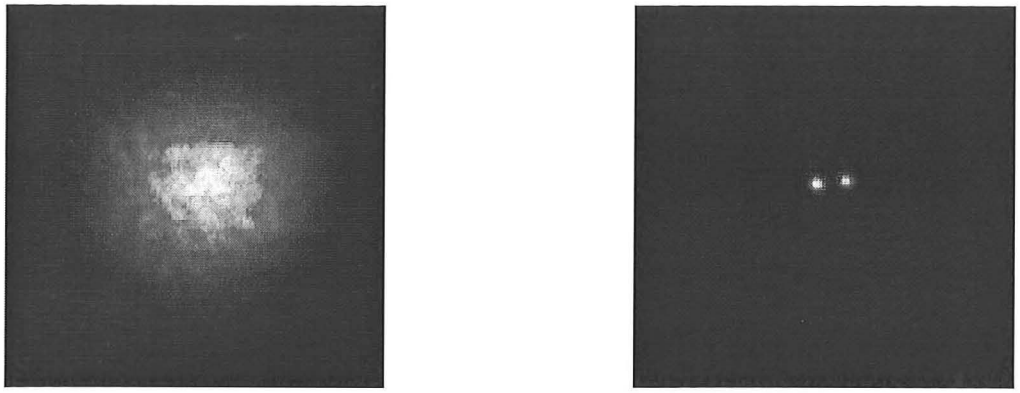

(a) (b)

Figure 1.2 Images of a binary star captured at the Starfire Optical Range, New Mexico, (a) without adaptive optics, and (b) with adaptive optics [2].

that one telescope will never be sufficient to collect data for the needs of all of the world's astronomers.

The large cost of construction, deployment and servicing of space telescopes means that overcoming the turbulence at ground-based telescopes with either adaptive optics or computer post-processing is required both now and in the foreseeable future.

1.2.2 Adaptive optics

In 1953, Horace Babcock [3] proposed a system to compensate for the effects of the atmosphere in real time by placing an element in the optical path to perform the inverse operation on the aberrated wavefront. This system has become known as adaptive optics and is currently employed at several observatories around the world, including Keck observatory [4], Lick observatory [5], Starfire optical range [6] and Subaru observatory [7]. A schematic of an adaptive optics system for an astronomical telescope is shown in Fig. 1.3.

Adaptive optics uses a closed loop feedback system to correct the random aberrations induced by the atmosphere. Since the path length of the aberration is constant for all wavelengths of light, it does not matter what wavelength of light the wavefront sensor, which is used to estimate the wavefront aberrations, receives. Thus the wavelengths of most scientific interest are passed to the detector, at the focal plane of the telescope, where the image of the astronomical object is formed. The remainder of the light is sent by a beam splitter to the wavefront sensor. The wavefront aberrations cannot be measured directly, and instead an aberration is introduced in the optical path to create two or more intensity distributions from which the wavefront slope or curvature can be estimated. The estimation of the aberrated wavefront is the primary topic of this thesis.

The wavefront estimate is then passed to the controller, which converts the wavefront es-

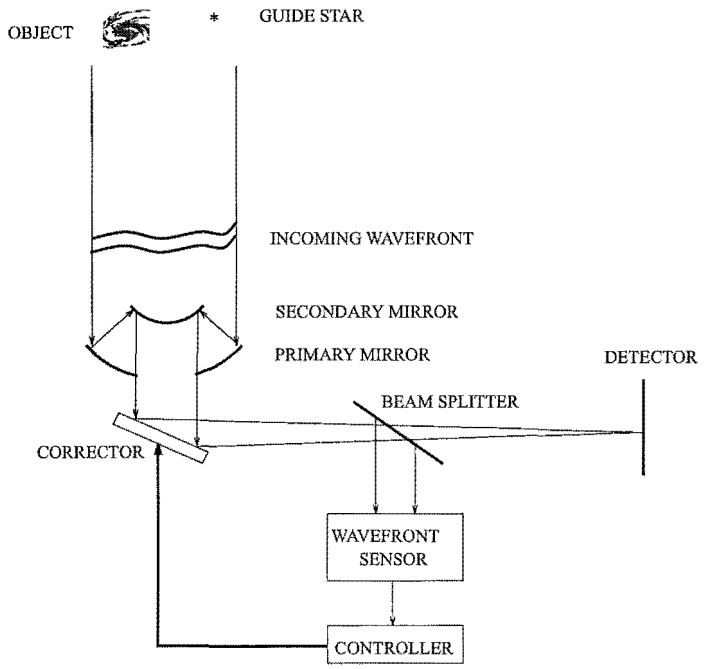

Figure 1.3 The block diagram of adaptive optics for astronomical imaging [8].

timate to a set of voltage signals. These voltage signals are fed back to control the wavefront corrector. The wavefront corrector, which is generally a deformable mirror, is then deformed in such a way as to best compensate the current estimate of the wavefront aberration.

The atmosphere is constantly changing with respect to time, with a coherence time, where the atmosphere is essentially frozen, of a few milliseconds. The adaptive optics feedback loop therefore needs to be run at several hundred Hertz to keep up with the time-varying nature of the turbulence.

Often the astronomical object of interest is not bright enough to provide the wavefront sensor with enough light to estimate the wavefront accurately. Thus a brighter guide star is often employed to drive the wavefront sensor whilst the science object of interest is imaged. This guide star needs to be located in the same area of the sky (the isoplanatic patch) as the astronomical object in order to estimate the same volume of turbulence. The guide star can be a nearby bright star, if one exists in the isoplanatic patch, or a star artificially generated using a laser focused to a point in the isoplanatic patch.

Images of a binary star, galaxy and a planet captured with, and without, adaptive optics are shown in Fig.s 1.2, 1.4 and 1.5 respectively. These images were captured at the Canada-France-Hawaii telescope in Hawaii and at the Starfire optical range in New Mexico.

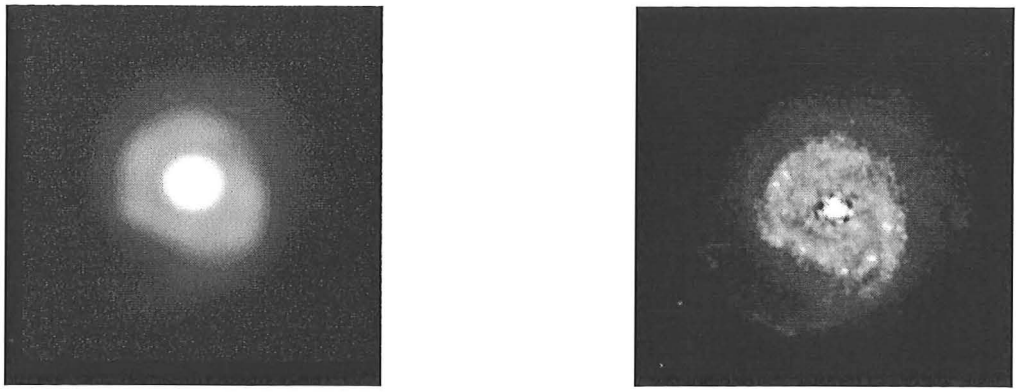

(a) (b)

Figure 1.4 Images of a galaxy captured with the Canada-France-Hawaii telescope at Mauna Kea, Hawaii, (a) without adaptive optics, and (b) with adaptive optics [9].

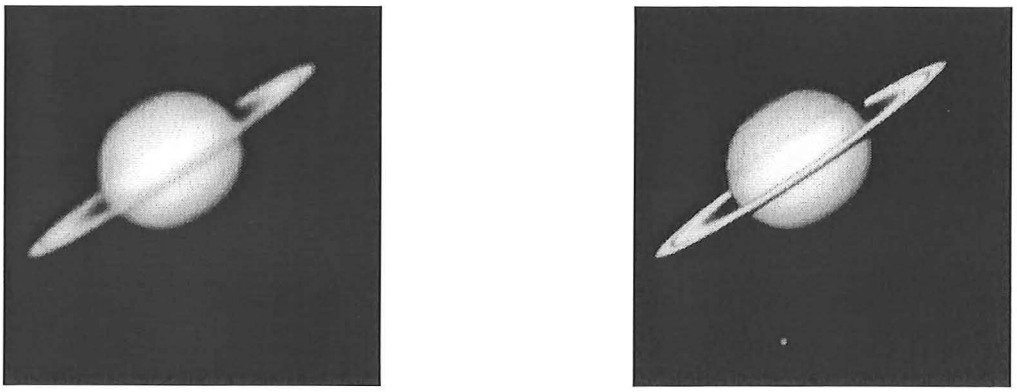

(a) (b)

Figure 1.5 Images of Saturn captured at the Starfire optical range, New Mexico, (a) without adaptive optics, and (b) with adaptive optics [10].

The components in an adaptive optics system are outlined in greater detail in Chapter 4. Original contributions to the field of adaptive optics, in particular the generalisation of the pyramid wavefront sensor [11], are discussed in Chapters 6 and 7 of this thesis.

1.2.3 Computer post-processing

Computer post-processing describes the set of methods that are used to overcome the effects of the atmosphere after the images of astronomical objects have been captured. The block diagram for a generic computer post-processing system is shown in Fig. 1.6. Unlike adaptive optics, which is a feedback system, computer post-processing is a feed-forward system. Computer post-processing has no correcting element. Instead, the images of the object and the information from the auxiliary channel are stored on computer and are the starting point for various deblurring algorithms. A multitude of such algorithms exist, with deconvolution from wavefront sensing, phase retrieval and phase diversity investigated in this thesis. These algorithms are discussed in more detail in Chapter 4.

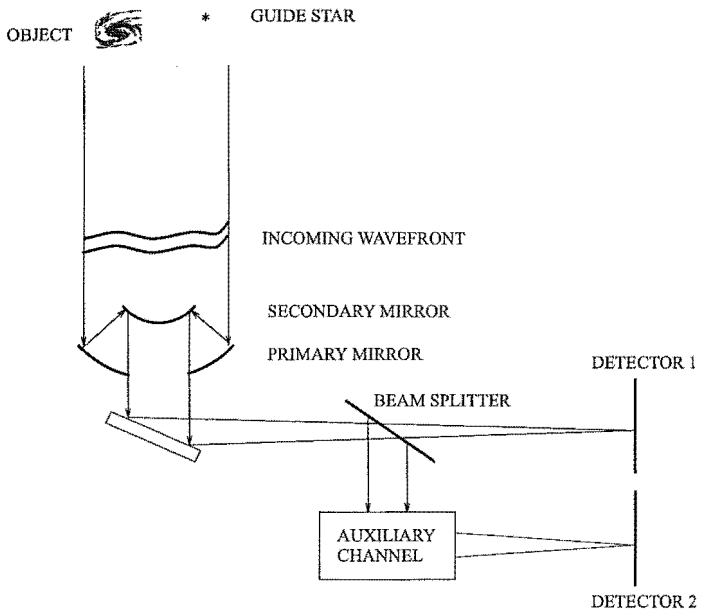

Figure 1.6 The block diagram for computer post-processing schemes for astronomical imaging.

The optional auxiliary channel depicted in Fig. 1.6 can be a wavefront sensor as in deconvolution from wavefront sensing and some phase retrieval algorithms, or an image of the object with a known aberration added, as in phase diversity. In many post-processing algorithms, such as most phase retrieval and blind deconvolution algorithms, there is no auxiliary channel and the image is deblurred solely from the information present in the imaging channel. However, the addition of an auxiliary channel often significantly improves the reliability of reconstructions.

Computer post-processing can also be used to improve the images that have been captured using adaptive optics on ground-based telescopes. For example, computer post-processing can be used to reduce the effects of the modes of atmospheric turbulence that the deformable mirror could not compensate.

Two chapters in this thesis are devoted to improvements made to existing computer post-processing algorithms. In Chapter 5, an alternative method for calibrating deconvolution from wavefront sensing is demonstrated. A new phase retrieval algorithm, which, like the pyramid wavefront sensor, subdivides the focal plane of the telescope, is proposed and analysed in Chapter 8.

1.2.4 Comparison of adaptive optics and computer post-processing

For ground-based telescopes the compensation of atmospheric turbulence can be achieved by either real-time adaptive optics systems or computer post-processing. The significant difference between the two is that adaptive optics is a closed loop system with feedback from the wavefront sensor to a correcting mirror. Adaptive optics systems are generally more expensive to build than computer post-processing ones because of the additional control electronics and the deformable mirror.

Adaptive optics has the inherent advantage of being less sensitive to component variation since it is a closed loop system. In addition, since the compensation is in real time it can easily be employed with a spectrograph, which is used to determine the chemical composition of astronomical objects from the wavelengths of light detected. Some wavefront sensors, notably the curvature and pyramid sensors, have an adjustable sensitivity that can be better utilised in a closed loop system. Once the loop is closed in an adaptive optics system, that is the atmosphere is being mostly compensated for, the sensitivity of the wavefront sensor can be increased to improve the measurements. A further advantage of adaptive optics over computer post-processing is that since the image of the object is smaller when detected, there is less read noise on the measurements.

Computer post-processing systems are not limited by the inability of the mirror to compensate certain modes. Also, in an adaptive optics system the current estimate of a wavefront at time t can only be gathered in the time range $(t - \Delta, t)$ where Δ defines the interval over which the atmosphere is effectively stable. When using computer post-processing, the wavefront estimate at time t is made from data gathered in the range $(t - \Delta, t + \Delta)$. Thus there are potentially twice as many photons available for an instantaneous wavefront estimate in a computer post-processing scheme than in an adaptive optics system.

Chapter 2

Mathematical Preliminaries

In this chapter, the mathematical functions and notation required to understand the rest of the thesis are briefly outlined. Firstly, the notation of common mathematical concepts is defined in Section 2.1. The special functions used to model physical phenomena of interest, such as apertures and stars, are defined in Section 2.2. In astronomical imaging, the wavefront sensing measurements, the estimated wavefront and the blurred image of the astronomical object are all treated in matrix form. The notation for matrix use in this thesis is set out in Section 2.3. Linear time-invariant systems, which mathematically describe imaging systems, are defined in Section 2.4. In optics, the complex fields at the aperture and focal planes are related as a Fourier transform pair. The properties of the Fourier, and also the Hankel and Hilbert, transforms are described in Section 2.5. The probability distributions relevant to this thesis, in particular in the area of photon detection, are discussed in Section 2.6. Finally, random processes are defined in Section 2.7 and this leads to the introduction of the structure function.

2.1 General notation

The notation of complex numbers and coordinate systems is defined in this section.

2.1.1 Coordinate systems

In this thesis, Cartesian coordinates are denoted by (x, y), (u, v) and (ξ, η). Sometimes, for compactness, the Cartesian coordinates are expressed in vector form by $\mathbf{x}$, $\mathbf{u}$, and $\boldsymbol{\xi}$ respectively. These three coordinate sets are used in the aperture, focal and conjugate aperture planes respectively throughout the thesis.

A function, $f(x, y)$, is circularly symmetric if it can be expressed as a function of only the

radial distance $r = \sqrt{x^2 + y^2}$, that is $f(r) = f(x, y)$. Such functions arise in optics due to the circular nature of lenses and telescope apertures, and in these situations a change of coordinate systems from Cartesian to polar coordinates can often reduce the complexity of the problem. The radial coordinates used in this thesis are r at the aperture plane and ρ at the focal plane.

2.1.2 Complex numbers

The imaginary number, which is defined by $\sqrt{-1}$, is denoted by j in this thesis. Complex numbers are used in electrical engineering and related disciplines to express a wave quantity, which has both magnitude and phase values, as a single number. A complex number z is given by

$$z = a + jb \tag{2.1}$$

where a and b are real numbers. a is the real part of the complex number and b the imaginary part. The magnitude of z is given by

$$|z| = \sqrt{a^2 + b^2}. \tag{2.2}$$

The phase of z is

$$\phi = \tan^{-1}\left(\frac{b}{a}\right). \tag{2.3}$$

Complex numbers are often expressed in polar coordinates

$$z = |z| \exp[j\phi]. \tag{2.4}$$

The complex conjugate of z, which is denoted by z^*, is given by

$$z^* = a - jb = |z| \exp[-j\phi]. \tag{2.5}$$

2.2 Special functions

In science and engineering, a number of special functions have been devised to describe real world physical phenomena that cannot be described with classical mathematical functions. These functions are often piece-wise in nature. Six such functions, the signum, rectangular, triangular, sinc, Heaviside unit step and Dirac delta functions are relevant to this thesis.

2.2.1 Sign function

The sign function, $\text{sgn}(x)$, models a discontinuity, such as with the optical knife-edge test, and is defined by [12]

$$\text{sgn}(x) = \begin{cases} -1, & x < 0 \\ 0, & x = 0 \\ +1, & x > 0. \end{cases} \tag{2.6}$$

2.2.2 Rectangle function

The rectangular function, $\text{rect}(x)$, is used to model the light transmission of square optical elements such as a square aperture or lenslet. In one dimension the definition of the rectangular function is [13]

$$\text{rect}(x) = \begin{cases} 1, & |x| < \frac{1}{2} \\ 0, & \text{otherwise.} \end{cases} \tag{2.7}$$

In two dimensions a square aperture is defined by $\text{rect}(x)\text{rect}(y)$.

2.2.3 Triangular function

The triangular function, $\text{tri}(x)$, which is used in this thesis to model the OTF of a square aperture, is defined by [13]

$$\text{tri}(x) = \begin{cases} 1 - |x|, & x < 1 \\ 0, & \text{otherwise.} \end{cases} \tag{2.8}$$

2.2.4 Sinc function

The sinc function, $\text{sinc}(x)$, arises from the Fourier transform of the rectangular function. The definition of the sinc function used in this thesis is

$$\text{sinc}(x) = \frac{\sin(\pi x)}{(\pi x)}. \tag{2.9}$$

2.2.5 Heaviside unit step

The Heaviside unit step function, $U(x)$, is used in this thesis to model the discontinuity at the edge of the aperture. The Heaviside unit step function is defined by [13]

$$U(x) = \begin{cases} 1, & x > 0 \\ 0, & x < 0. \end{cases} \tag{2.10}$$

2.2.6 Dirac delta function

The Dirac delta function is used in astronomical imaging to model a distant single star. The one-dimensional Dirac delta function, $\delta(x)$, is the derivative of the Heaviside step function and is defined by [13]

$$\delta(x) = \begin{cases} \infty, & x = 0 \\ 0, & \text{otherwise}, \end{cases} \tag{2.11}$$

and

$$\int_{-\infty}^{\infty} \delta(x)\mathrm{d}x = 1. \tag{2.12}$$

Although in practice no object is truly a delta function, it is an excellent model for objects whose size is significantly below the effective instrument resolution.

The delta function is useful because of its 'collapsing' integrals [14], which is also known as the sifting property,

$$f(x_0) = \int_{-\infty}^{\infty} f(x)\delta(x - x_0). \tag{2.13}$$

2.3 Matrices

Wavefront sensing measurements and images of astronomical objects are stored as matrices in this thesis. In this section, the notation of matrix operators, which are used on the wavefront sensing measurements to estimate the wavefront, are defined.

A matrix, A, of M rows and N columns is defined as

$$A = \begin{pmatrix} a_{11} & a_{12} & \dots & a_{1N} \\ a_{21} & a_{22} & & \\ \vdots & & \ddots & \vdots \\ a_{M1} & & \dots & a_{MN} \end{pmatrix}, \tag{2.14}$$

where a_{mn} is the element of A in the m^{th} row and n^{th} column. Matrix A is square if $M = N$.

The identity matrix, I, is defined by $AI = IA = A$ [15]. I consists of ones on the diagonal and zeros elsewhere. The identity matrix is analogous to the number 1 in numerical multiplication.

The transpose of a matrix A, which is denoted by A^T, is obtained by replacing a_{mn} with a_{nm}. The transpose of A, which is defined in Eq. (2.14), is given by

$$A^T = \begin{pmatrix} a_{11} & a_{21} & \dots & a_{M1} \\ a_{12} & a_{22} & & \\ \vdots & & \ddots & \vdots \\ a_{1N} & & \dots & a_{MN} \end{pmatrix}. \tag{2.15}$$

If A is an $M \times N$ matrix then A^T is $N \times M$.

The inverse of a square matrix A is denoted by A^{-1}, and defined by $AA^{-1} = I = A^{-1}A$. If A^{-1} exists, then A is said to be invertible.

A square matrix A is positive definite if $x^T Ax > 0$ for all non zero x vectors [15]. Similarly A is positive semi-definite if $x^T Ax \geq 0$ for all non zero x vectors. A key use of positive definite matrices is in estimation theory, where A is defined by the covariance of random variables. This is discussed further in Section 2.6.5.

2.4 Linear systems

A system, which is denoted by $\mathcal{L}$, describes mathematically the mapping of an input function $F(x)$ to an output function $G(x)$:

$$\mathcal{L}\{F(x)\} = G(x). \tag{2.16}$$

In this thesis, the primary system of interest is the atmosphere, where the input is the astronomical object of interest and the output is the distorted image.

A linear system is one which obeys the principle of superposition, such that

$$\mathcal{L}\{F_1(x) + F_2(x)\} = \mathcal{L}\{F_1(x)\} + \mathcal{L}\{F_2(x)\}. \tag{2.17}$$

A system can be characterised mathematically by its response to a delta function, and this is known as the impulse response, $H(x)$,

$$H(x, x_0) = \mathcal{L}\{\delta(x - x_0)\}. \tag{2.18}$$

The impulse response of an optical system is known as the point spread function (PSF). A linear system is also time invariant if a shift in the input results in the same shift of the output such that

$$\mathcal{L}\{F(x - x_0)\} = G(x - x_0). \tag{2.19}$$

For any linear time invariant (LTI) system, the complex exponential $\exp[j2\pi ft]$ is an eigenfunction with $h(f)$ the corresponding eigenvalue. The output of an LTI system is therefore

$$\mathcal{L}\{\exp[j2\pi ft]\} = h(f)\exp[j2\pi ft]. \tag{2.20}$$

The eigenvalue function, $h(f)$, which is defined as the transfer function, describes the magnitude attenuation and phase delay of the system on a complex exponential. The transfer function of an optical LTI system is called the optical transfer function (OTF).

2.5 Transform theory

In many science and engineering disciplines, the problem can be simplified with the use of an appropriate mathematical transform. The three transforms employed in this thesis are the Fourier, Hankel and Hilbert. Of these, the most important for wavefront sensing and phase retrieval is the Fourier transform since it can be used to model the propagation of light waves. The notation and important properties of the Fourier transform are outlined in this section. This is followed by a brief discussion of each of the Hankel and Hilbert transforms.

2.5.1 The Fourier transform

Joseph Fourier devised his transform to describe heat flow in solid bodies [13]. The Fourier transform (FT) has subsequently been applied to problems in, amongst others, communications theory, vibration analysis, image processing and wave propagation. The FT is used to convert the signal from one domain to another. For example, in communications theory the FT relates the temporal (t) and frequency (f) domains of a signal. The FT of a

continuous one-dimensional signal $G(t)$ is defined as [13]

$$g(f) = \mathcal{F}\{G(t)\} = \int_{-\infty}^{\infty} G(t) \exp[-j2\pi ft]\mathrm{d}t, \tag{2.21}$$

where $\mathcal{F}$ denotes the FT operation. The corresponding inverse Fourier transform (IFT) is given by

$$G(t) = \mathcal{F}^{-1}\{g(f)\} = \int_{-\infty}^{\infty} g(f) \exp[j2\pi ft]\mathrm{d}f. \tag{2.22}$$

The same letter is used to denote the signal in the two domains, with upper case used in the time domain and lower case in the frequency domain. It is important to note that the kernel of the FT, $\exp[-j2\pi ft]$, are the eigenfunctions for a LTI system, as described in Section 2.4.

2.5.2 The Fourier transform in two dimensions

In astronomical imaging the parameters of interest, such as the wavefront at the aperture and the intensity at the focal plane, are two dimensional quantities. The one dimensional FT and IFT of Eq.s (2.21) and (2.22) can be extended to two dimensions. The time dimension t is replaced with the spatial domain dimensions (x, y) and frequency f by the Fourier domain dimensions (u, v). The FT is defined in two dimensions by

$$g(u, v) = \int_{-\infty}^{\infty}\int_{-\infty}^{\infty} G(x, y) \exp[-j2\pi(ux + vy)]\mathrm{d}x\mathrm{d}y, \tag{2.23}$$

and the IFT by

$$G(x, y) = \int_{-\infty}^{\infty}\int_{-\infty}^{\infty} g(u, v) \exp[j2\pi(ux + vy)]\mathrm{d}u\mathrm{d}v. \tag{2.24}$$

In this thesis upper case quantities are used to denote functions of the aperture dimensions (x, y), with the lower case counterpart used for functions of the focal plane dimensions (u, v).

The two dimensional FT is a separable transform; that is the integral can be computed in each dimension. For example, Eq. (2.23) can be rewritten as

$$g(u, v) = \int_{-\infty}^{\infty}\left[\int_{-\infty}^{\infty} G(x, y) \exp[-j2\pi ux]\mathrm{d}x\right] \exp[-j2\pi vy]\mathrm{d}y, \tag{2.25}$$

and a similar result holds for the IFT. The properties of the two dimensional FT pertinent to this thesis are outlined in the next subsection.

2.5.3 Properties of the Fourier transform

The FTs of analytic functions can be simplified using the theorems of the FT which are discussed below. For the following theorems it is assumed $G(x, y)$ and $g(u, v)$ are a FT pair, as are $H(x, y)$ and $h(u, v)$.

Convolution theorem

The most important theorem of the FT in relation to this thesis is the convolution theorem. Firstly, it is necessary to define the convolution operator $\odot$ and the convolution integral of two functions, $G(x, y)$ and $H(x, y)$,

$$G(x, y) \odot H(x, y) = \int_{-\infty}^{\infty} \int_{-\infty}^{\infty} G(\xi, \eta) H(x - \xi, y - \eta) \mathrm{d}\xi \mathrm{d}\eta, \tag{2.26}$$

where ξ and η are dummy variables of integration. The convolution of two signals arises naturally in many science disciplines. For example, in astronomical imaging the image detected at the telescope is the convolution of the true astronomical object with the point spread function of the atmosphere and optical imaging system.

The convolution theorem for the FT is defined by

$$\mathcal{F}\{G(x, y) \odot H(x, y)\} = g(u, v) h(u, v). \tag{2.27}$$

The convolution theorem thus states that the FT of the convolution of two signals is equal to the multiplication of their respective spectra in the other domain. The convolution theorem can be used to simplify systems analytically by replacing a convolution problem with a multiplication one in the other Fourier domain.

Correlation theorem

The correlation of two functions measures the similarity between the two when they are displaced by (x, y) from each other. A high correlation value at a point (x, y) indicates that the signals are similar for that displacement. Conversely, a low correlation value indicates the two functions are dissimilar for that displacement. The correlation integral of two signals, G(x,y) and H(x,y), is defined by

$$G(x, y) \otimes H(x, y) = \int_{-\infty}^{\infty} \int_{-\infty}^{\infty} G(\xi, \eta) H^*(x + \xi, y + \eta) \mathrm{d}\xi \mathrm{d}\eta \tag{2.28}$$

where $\otimes$ is used in this thesis to denote correlation. If a signal $G(x, y)$ is correlated with a different signal, then the process is referred to as cross-correlation. Whereas the correlation of $G(x, y)$ with itself is referred to as auto-correlation.

The auto-correlation theorem of the FT is given by [14]

$$\mathcal{F}\{G(x,y) \otimes G(x,y)\} = \mathcal{F}\{G(x,y) \odot G^*(x,y)\} = g(u,v)g^*(u,v) = |g(u,v)|^2. \tag{2.29}$$

That is, the FT transform of an auto-correlation of a signal $G(x,y)$ is equal to the magnitude squared of the signal in the Fourier domain. The autocorrelation theorem's relevance to astronomical imaging is that the intensity measured at the focal plane of an optical instrument is the magnitude squared of the complex field in the focal plane.

Linearity theorem

The linearity theorem for the FT is defined as

$$\mathcal{F}\{aG(x,y) + bH(x,y)\} = ag(u,v) + bh(u,v), \tag{2.30}$$

where a and b are constants. Thus the spectrum of a sum of signals is the sum of the spectra of the individual signals.

Shifting theorem

The shifting theorem for the FT is given by

$$\mathcal{F}\{G(x,y)\exp[j2\pi(xa+yb)]\} = g(u-a, v-b), \tag{2.31}$$

where a and b are real constants. Thus the shifting theorem states that the FT of a function with a linear phase shift in the spatial domain results in a shift of the image in the Fourier domain. In astronomical imaging, the shifting theorem arises when considering wavefront tilts which are of the form $\exp[j2\pi(xa+yb)]$. If the wavefront at the aperture has a tilt term, then the intensity at the focal plane is shifted by (a,b).

The converse of Eq. (2.31) is that the FT of a function in the spatial domain that is shifted results in a linear phase shift of the image in the Fourier domain,

$$\mathcal{F}\{G(x-a, y-b)\} = g(u,v)\exp[-j2\pi(ua+vb)]. \tag{2.32}$$

Similarity theorem

The similarity theorem of the FT is

$$\mathcal{F}\{G(ax,by)\} = \frac{1}{ab}g\left(\frac{u}{a}, \frac{v}{b}\right), \tag{2.33}$$

where a and b are constants. The significance of the similarity theorem is that compression of the signal in one domain results in the expansion of its Fourier pair in the other domain. A consequence of the similarity theorem is the Heisenberg uncertainty principle, which states that the more accurately the position of a particle is known, the less accurately the momentum (its Fourier pair) is known.

2.5.4 The discrete Fourier transform

Eq.s (2.23) and (2.24), which describe the two dimensional FT, are defined for continuous functions. However, in astronomical imaging and many other engineering applications, the signals are discrete since the signal is sampled. For example, in astronomical imaging the intensity at the focal plane is sampled with a CCD. Also, the integrals of Eq.s (2.23) and (2.24) are over infinite extents, whereas physically the signals can only be sampled over a finite region (in space or time). In practice, the continuous FT can be approximated with the discrete Fourier transform (DFT). The DFT of a discrete signal $G(x, y)$, of dimension $N \times N$ samples, is given by

$$g(u, v) = \frac{1}{N^2} \sum_{x=0}^{N-1} \sum_{y=0}^{N-1} G(x, y) \exp[-j \frac{2\pi(ux + vy)}{N}], \tag{2.34}$$

and the inverse DFT by

$$G(x, y) = \sum_{u=0}^{N-1} \sum_{v=0}^{N-1} g(u, v) \exp[j \frac{2\pi(ux + vy)}{N}]. \tag{2.35}$$

The DFT implicitly assumes that the signal being transformed is periodic outside the sampled range. If the sampled data contains an integral number of periods of the signal, then no error is introduced by using the DFT and its inherent assumption of periodicity. However, if the sampled data does not contain an integral number of periods of the signal, then spectral leakage from the true spectral components to other surrounding frequencies occurs.

2.5.5 The fast Fourier transform

Computationally, the DFT is computed using the fast Fourier transform (FFT) algorithm, which was devised by Cooley and Tukey in 1965 [16]. The computational advantage of the FFT over the DFT implemented using Eq. (2.34) is that there are $N/\log_2 N$ fewer multiplications [13]. The FFT is most efficiently implemented on arrays of size $2^N \times 2^N$, where N is a whole number. In this thesis, atmospheric phase screens are chosen to be of dimension $2^N \times 2^N$ for the most efficient computation.

2.5.6 Hankel transform

The complex fields produced by circular optical components, such as lenses and apertures, or those radiating from a point source are often circularly symmetric in nature. As discussed in Section 2.1.1, a circularly symmetric function $G(x, y)$ can be expressed in terms of the radius only, $G(r)$. The Fourier transform of a circularly symmetric function can instead be performed with the Hankel transform, which calculates the integral over one radial coordinate rather than the two independent Cartesian coordinates of the Fourier transform. The Hankel transform of $G(r)$ is defined by

$$g(\rho) = 2\pi \int_0^\infty G(r) J_0(2\pi\rho r) r \, \mathrm{d}r, \tag{2.36}$$

where J_0 is the zero-order Bessel function of the first kind and is given by [13]

$$J_0(r) = \frac{1}{2\pi} \int_0^{2\pi} \exp[-jr\cos\theta] \mathrm{d}\theta. \tag{2.37}$$

Eq. (2.36) shows that the Hankel transform of a circularly symmetric function is another circularly symmetric function. The inverse Hankel transform is given by

$$G(r) = 2\pi \int_0^\infty g(\rho) J_0(2\pi\rho r) \, \rho \mathrm{d}\rho. \tag{2.38}$$

It is interesting to note from Eq.s (2.36) and (2.38) that the kernel is the same for both the Hankel and inverse Hankel transforms.

2.5.7 Hilbert transform

The Hilbert transform of a signal, $G(x)$, is defined as $H\{(G(x)\}$ by [13]

$$H\Big\{G(x)\Big\} = \frac{-1}{\pi x} \odot G(x) = \frac{1}{\pi} \int_{-\infty}^{\infty} \frac{G(x')dx'}{x' - x} \tag{2.39}$$

and corresponds to a filtering whereby the magnitudes of the spectral components of $g(u)$ are left unchanged but the phases are altered by $\frac{\pi}{2}$, positively or negatively according to the sign of u. The Hilbert transform is used in this thesis to describe the signals produced by the Foucault knife edge test.

2.6 Probability theory

So far in this chapter the functions have been deterministic; that is the output is uniquely determined by the input. However, in astronomical imaging the functions of interest, namely those relating to the turbulence in the atmosphere and the detection of light, are

stochastic in nature; that is there is a random component to the signal. In this section, random variables are introduced, and the Gaussian and Poisson probability distributions, which are used in later chapters, are discussed.

2.6.1 Random variables

A random variable X assigns a probability to each possible outcome x. A distinction is made between discrete and continuous random variables depending on whether the set of outcomes is discrete or continuous. For example, photon detection with a CCD is a discrete random variable since the outcome has to be a discrete value. Whereas the wavefront phase at a point in the aperture is a continuous random variable since the outcome can be any value.

2.6.2 Discrete random variables

The probability that a discrete random variable X has the outcome x is denoted by

$$Pr\{x\} = Pr\{X = x\}, \tag{2.40}$$

where $Pr\{\}$ is the probability operator.

The two conditions that a discrete random variable must meet are [17]:

1. $0 \leq Pr\{x\} \leq 1$.
2. $\sum_x Pr\{x\} = 1$.

The mean, μ_X, or expected value $\mathrm{E}[X]$, of a discrete random variable is given by

$$\mu = \mathrm{E}[X] = \sum_x x Pr\{x\}. \tag{2.41}$$

The variance of X is denoted by σ^2, or $\mathrm{Var}[X]$, and is defined by

$$\sigma^2 = \mathrm{Var}[X] = \sum_x (x - \mu)^2 \Pr\{x\}. \tag{2.42}$$

The variance of X describes the spread of the distribution. The square root of the variance, σ, is the standard deviation.

The Poisson random variable provides a model for data that represent the number of occurrences of a specified event in a given unit of space or time [17]. In this thesis, the Poisson probability distribution is used to model the probability of photons arriving at each pixel in

the detector within a specific time-frame. The Poisson distribution has a single parameter, λ, which is both the mean and variance of the distribution. The probability of the outcome x for a Poisson random variable X is

$$Pr\{x\} = \frac{\lambda^x \exp[-\lambda]}{x!}, \tag{2.43}$$

where ! is the factorial operator.

2.6.3 Continuous random variables

The cumulative density function (CDF), $F_X(x)$, of a continuous random variable X is defined by

$$F_X(x) = Pr\{X \leq x\}. \tag{2.44}$$

The CDF is a monotonically increasing function. The probability density function (PDF), $f_X(x)$, of X is defined by

$$f_X(x) = \frac{\mathrm{d}F_X(x)}{\mathrm{d}x}. \tag{2.45}$$

The PDF of X must satisfy these two requirements:

1. $f_X(x) \geq 0$.
2. $\int_{\infty}^{-\infty} f_X \mathrm{d}x = 1$.

The mean, μ_X, or expected value, $\mathrm{E}[X]$, of a continuous random variable X is defined by

$$\mu = \mathrm{E}[X] = \int_{-\infty}^{\infty} x f_X(x) \mathrm{d}x. \tag{2.46}$$

The variance, σ^2, or $\mathrm{Var}[X]$, of X is

$$\sigma^2 = \mathrm{Var}[X] = \int_{-\infty}^{\infty} (x-\mu)^2 f_X(x) \mathrm{d}x. \tag{2.47}$$

The Gaussian, or normal, probability distribution is used throughout humanities, science and engineering disciplines to model sets of continuous measurements. The Gaussian PDF, with mean μ and variance σ^2, is defined by [18]

$$f_X(x) = \frac{1}{\sigma\sqrt{2\pi}} \exp\left[\frac{-(x-\mu)^2}{2\sigma^2}\right]. \tag{2.48}$$

2.6.4 Central limit theorem

The central limit theorem states that for N independent random variables $\{X_1, X_2, \ldots X_N\}$, with arbitrary means $\{\mu_1, \mu_2 \ldots \mu_N\}$ and variances $\{\sigma_1^2, \sigma_2^2 \ldots \sigma_N^2\}$ and not necessarily known distribution, the random variable, Z, defined by

$$Z = \frac{1}{N} \sum_{i=1}^{N} X_i, \tag{2.49}$$

approaches a Gaussian distribution with mean $\mu_Z = \mu_X$ and $\sigma_Z = \sigma_X/\sqrt{N}$ as $N \to \infty$, where $\mu_X = \frac{1}{N} \sum_{i=1}^{N} \mu_i$ and $\sigma_X^2 = \sum_{i=1}^{N} \sigma_i^2$. The central limit theorem thus explains why so many probability distributions exist in nature that are approximately Gaussian.

An implication of the central limit theorem is that the means of samples of size N taken from a distribution of mean μ and variance σ^2 are Gaussian distributed with a mean of μ and variance σ^2/N. The standard deviation of the sample means is known as the standard error in the mean. In this thesis, the standard error in the mean is used as an estimate of the uncertainty in the mean of a simulated parameter.

2.6.5 Joint random variables

Joint random variables model physical situations which have more than one outcome. For example, photon detection on a CCD has both x and y coordinate outcomes. The joint CDF, $F_{XY}(x, y)$, of two random variables, X and Y, is defined by

$$F_{XY}(x, y) = Pr\{X \leq x \quad \text{AND} \quad Y \leq y\} \tag{2.50}$$

The joint PDF is given by

$$f_{XY}(x, y) = \frac{\partial^2 F_{XY}(x, y)}{\partial x \partial y}. \tag{2.51}$$

The covariance of two random variables, X and Y, is defined by

$$\begin{aligned} \text{Cov}(X, Y) &= \text{E}[(X - \mu_x)(Y - \mu_Y)] \\ &= \int_{-\infty}^{\infty} \int_{-\infty}^{\infty} f_{XY}(x, y)(x - \mu_x)(y - \mu_Y) \text{d}x\text{d}y. \end{aligned} \tag{2.52}$$

The covariance of a random variable with itself, C_{XX}, is simply the variance of that random

variable, σ_X^2. The covariance matrix for two random variables is

$$C_{X,Y} = \begin{bmatrix} \mathrm{Cov}(X,X) & \mathrm{Cov}(X,Y) \\ \mathrm{Cov}(Y,X) & \mathrm{Cov}(Y,Y) \end{bmatrix}. \tag{2.53}$$

The covariance matrix can be extended to any number of joint random variables. In this thesis the covariance matrix for the modes of atmospheric turbulence is used as prior knowledge when estimating the wavefront phase. Covariance matrices are positive definite, which implies $x^T C^{-1} x$ is positive for all x.

2.6.6 Conditional probability and Bayes' rule

Often two events are related in such a way that the probability of one occurring is dependent on whether the other event has occurred or not. This is known as conditional probability [17]. The conditional probability of event A occurring given that B has occurred is defined by

$$Pr\{A|B\} = \frac{Pr\{AB\}}{Pr\{B\}}, \tag{2.54}$$

where | denotes conditional probability. Similarly, the probability of event B occurring given that A has occurred is

$$Pr\{B|A\} = \frac{Pr\{AB\}}{Pr\{A\}}. \tag{2.55}$$

Combining Eq.s (2.54) and (2.55) yields Bayes' rule

$$Pr\{A|B\} = \frac{Pr\{B|A\}\,\mathrm{Pr}\{A\}}{Pr\{B\}}, \tag{2.56}$$

which relates the two conditional probabilities. Bayes' rule is used in Section 4.2 to find the most likely wavefront given the measured data.

2.7 Random processes

A random process $X(t)$ is a sequence of random variables in time or space of both [19]. The value of the random process at each point in space or time is itself a random variable. A random process is defined to be wide-sense stationary if the ensemble average for any t_1 and t_2 is the same [12],

$$\mathrm{E}[X(t_1)] = \mathrm{E}[X(t_2)], \tag{2.57}$$

and the auto-correlation is only a function of the separation of the two points, t_1 and t_2,

$$C_X(t_1, t_2) = C_X(t_1 - t_2). \tag{2.58}$$

2.7.1 The structure function

The covariance of a random process provides a measure of the relationship between the process at two points in space or time. However, processes with infinite covariance arise in the study of atmospheric turbulence. The structure function was introduced to overcome this anomaly. The structure function, $D_X(t)$, is defined by [19]

$$\begin{aligned} D_X(t) &= \mathrm{E}[(X(\tau) - X(t+\tau))^2] && (2.59) \\ &= 2(C_X(0) - C_X(t)). && (2.60) \end{aligned}$$

From Eq. (2.60) it is clear that the structure function has a value of zero for zero separation. The structure function is used in Chapter 3 to analyse velocity, temperature, refractive index and phase fluctuations in the atmosphere.

From the auto-correlation theorem, Eq. (2.29), the autocorrelation, $C_X(t)$, of a random process is related to the power spectrum, $\Phi(\kappa)$, by

$$\Phi(\kappa) = \int_{-\infty}^{\infty} C_X(t) \exp[-2\pi j \kappa t] \mathrm{d}t. \tag{2.61}$$

The power spectrum describes the structure of the process in Fourier space.

Chapter 3

Imaging Through Turbulence

> "If the Theory of making Telescopes could at length be fully brought into Practice, yet there would be certain Bounds beyond which Telescopes could not perform. For the Air through which we look upon the Stars, is in a perpetual Tremor; as may be seen by the tremulous Motion of Shadows cast from high Towers, and by the twinkling of the fixd Stars ... Long Telescopes may cause Objects to appear brighter and larger than short ones can do, but they cannot be so formed as to take away that confusion of the Rays which arises from the Tremors of the Atmosphere."
>
> Sir Isaac Newton, *Opticks*, 1704

Sir Isaac Newton in his 1704 treatise Opticks [20] was the first person to correctly describe how the atmosphere limits the resolution and quality of images viewed through ground-based telescopes. This chapter reviews the work done by scientists and engineers since Newton in the area of imaging through the atmosphere, culminating in a statistical model of the atmosphere and the images captured through the atmosphere.

The nature of light has caused great debate over the previous three centuries. Early theories considered light to be a stream of particles, known as photons, and Newton was a proponent of this theory [21]. Huygens and Hooke, on the other hand, believed that light propagated as a wave. In practice, the dual nature of light is generally accepted as a convenient model.

Geometric optics is the study of optics assuming light propagates in straight lines. Geometric optics is consistent with the photon model of light but cannot explain the effects of diffraction or interference. In contrast, the Fourier optics model of light treats light as a wave and can explain the physical phenomena of interference and diffraction. In this the-

sis, the Fourier optics model is used for light propagation and the geometric optics model for light detection.

This chapter is divided into four sections; firstly, the optical theory required to understand the rest of this thesis is presented. The nature and statistics of the optical properties of the atmosphere are analysed in the second section. The implications of imaging through this atmospheric model are then examined in the third section. Finally, the modelling of the detection of photons is discussed.

3.1 Optics theory

A discussion of the propagation of light is necessary to fully understand the later chapters of this thesis. The review of optics theory in this section is made firstly from a geometric (first-order) perspective, which considers light to propagate in photon form. This is followed by the more exact Fourier point-of-view, where the propagation is considered in wave form.

3.1.1 Geometric optics

Principles of geometric optics

To describe geometric optics it is first necessary to define light rays and the wavefront. Light rays diverge in straight lines from a point source as shown in Fig. 3.1. A wavefront is considered to be the surface of constant optical path length from the point source or alternatively the surface perpendicular to the light rays.

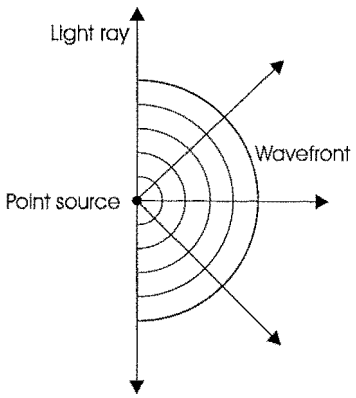

Figure 3.1 Light rays diverge radially from a point source. A wavefront is the surface perpendicular to the light rays.

The speed of light in a vacuum, c, is $3\times10^{8}\text{ms}^{-1}$. The speed of light is slower in all other media. The ratio of the speed of light in a vacuum to the speed in a particular medium, v,

defines the refractive index, n, of that medium [21]

$$n = \frac{c}{v} \tag{3.1}$$

The refractive index of a vacuum is therefore 1 and greater than 1 for all other media. The refractive index of a particular medium is dependent on its magnetic permeability and dielectric constant. Of particular relevance to this thesis is the variation of the refractive index of air with temperature which occurs in the atmosphere. It is these refractive index fluctuations that induce wavefront aberrations which subsequently distort the images of astronomical objects captured at ground-based telescopes.

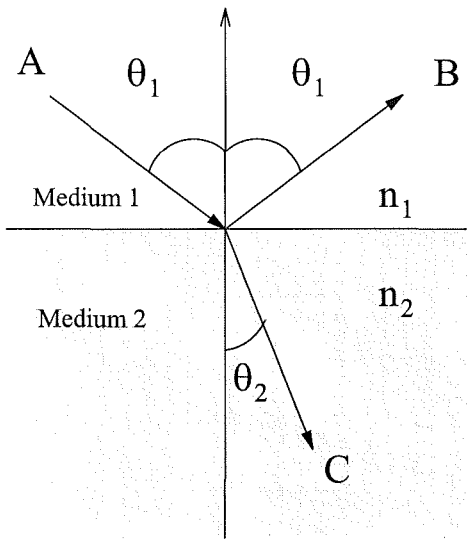

Figure 3.2 Reflection and refraction of light at an interface between two media with different refractive indices.

When a light ray hits the intersection between two media, two important optical phenomena occur as shown in Fig. 3.2, reflection and refraction. Some of the light from point A travelling through medium 1 is reflected back through medium 1 to point B. The angle of incidence of the ray from A, measured to the line normal to the interface, θ_1, is equal to the angle of reflection, also measured to the normal. The rest of the light from A passes through the interface between the two media and through to point C. The angle of refraction, θ_2, of the transmitted ray is governed by Snell's law

$$\frac{n_2}{n_1} = \frac{\sin(\theta_1)}{\sin(\theta_2)} = \frac{v_1}{v_2}, \tag{3.2}$$

where v_1 and v_2 are the speed of light in the two media.

Lenses, mirrors and telescopes

The main optical components of an optical system: mirrors, lenses and telescopes are now discussed from a geometric optics perspective. Lenses are used in optical systems to magnify objects. This is achieved by converging or diverging wavefronts using refraction. The wavefronts can be shaped by the lens as light travels slower through the lens than through air. There are a variety of different lens types (shapes); a double concave lens is shown in Fig. 3.3. The focal length of a lens, f, is dependent on the radii of curvature of the two sides of the lens, r_1 and r_2, and the refractive index of the lens material, n,

$$\frac{1}{f} = (n-1)\left(\frac{1}{r_1} - \frac{1}{r_2}\right). \tag{3.3}$$

Lenses are often classified by their 'F' number, F, which is defined as the ratio of the focal length of the lens to its diameter, D,

$$F = \frac{f}{D}. \tag{3.4}$$

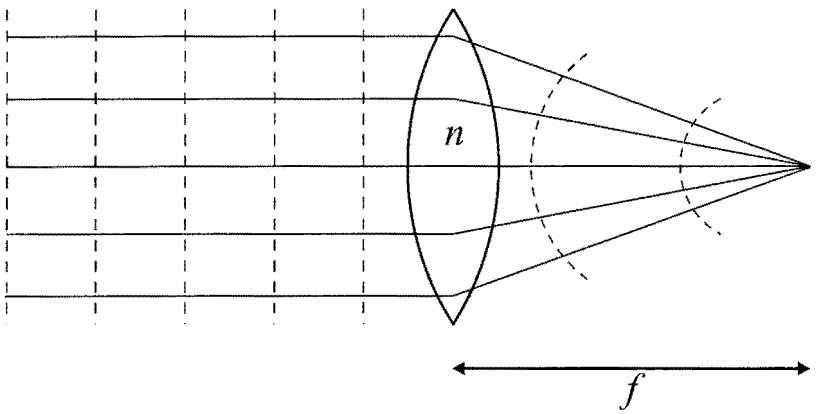

Figure 3.3 A double-convex lens of refractive index n converges planar wavefronts to a point at a distance f from the lens. The dotted lines are the wavefronts and the solid lines the direction of light propagation. [22]

Mirrors are used in optical systems to reflect and reshape wavefronts. A concave mirror is shown in Fig. 3.4, which converges planar wavefronts to a point. The focal length of the mirror is half the radius of the mirror, $f = r/2$. Mirrors are generally preferred to lenses in the design of telescopes since they can operate over a wider range of wavelengths and do not suffer from chromatic aberrations due to the dispersion of light.

The aperture of an imaging system is defined as the optical component over which light collection takes place. The intensity and resolution of an image are dependent on the size of the aperture.

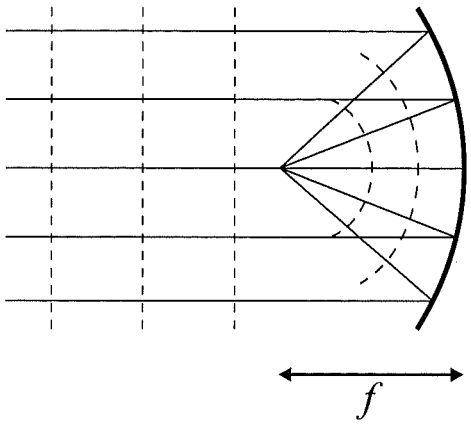

Figure 3.4 A concave mirror converges wavefronts to a point f in front of the mirror. [22]

The class of telescopes that are used in this thesis, such as that at the Obsevatoire de Lyon and at Mt. John, is the Cassegrain telescope. A Cassegrain telescope consists of a parabolic primary mirror and a hyperbolic secondary mirror as shown in Fig. 3.5(a). The aperture (primary mirror) is obscured by the secondary mirror and its supports, so the magnitude of the aperture is not a perfect circle as can be seen in Fig. 3.5(b) for the telescope at Lyon. This obscuration results in a loss of light for the image and wavefront sensor.

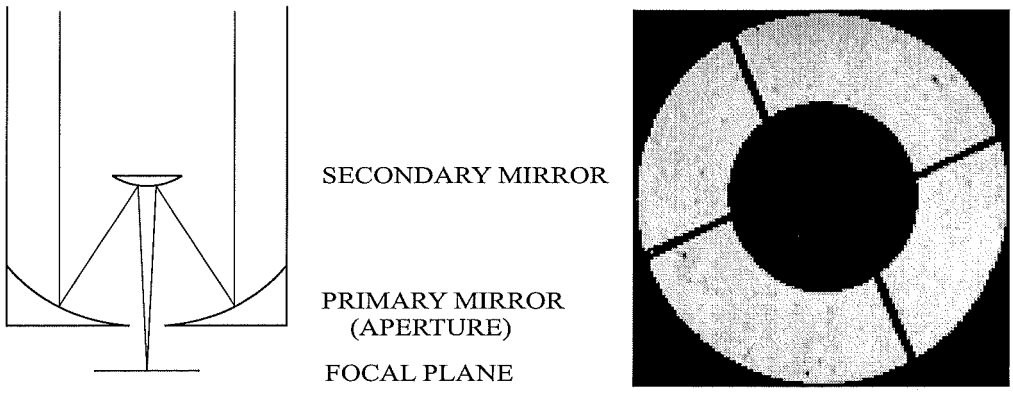

Figure 3.5 (a) Optical layout of a Cassegrain telescope. [22] (b) Magnitude of the aperture of the Cassegrain telescope at the Observatoire de Lyon.

Geometric optics wavefront propagation

The propagation of an arbitrary one-dimensional wavefront, $W(x, z)$, is now considered using the principles of geometric optics. The wavefront propagates perpendicularly to the wavefront at each point in the wavefront. This is shown for three photons in an arbitrary wavefront in Fig. 3.6. The change in intensity, $\partial I(x, z)/\partial x$, of the wavefront as it propagates

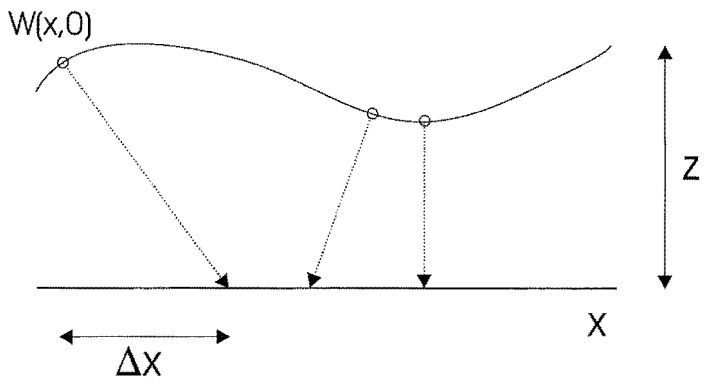

Figure 3.6 A wavefront is propagated a distance z. A photon from a point in the wavefront $W(x,0)$ is displaced by a distance Δx.

a distance z is given by the irradiance transport equation (ITE), which in one dimension (x) is given by [23]

$$\frac{\partial I(x,z)}{\partial z} = -\frac{\partial^2 W(x,z)}{\partial x^2} I(x,z) - \frac{\partial I(x,z)}{\partial x}\frac{\partial W(x,z)}{\partial x}. \tag{3.5}$$

The corresponding change in the wavefront is governed by the wavefront transport equation (WTE),

$$\frac{\partial W(x,z)}{\partial z} = 1 - \frac{1}{2}\left(\frac{\partial W(x,z)}{\partial x}\right)^2 + \frac{\lambda^2}{16\pi^2 I(x,z)}\frac{\partial^2 I(x,z)}{\partial x^2} - \frac{\lambda^2}{32\pi^2 I^2(x,z)}\left(\frac{\partial I(x,z)}{\partial x}\right)^2, \tag{3.6}$$

where λ is the wavelength. The geometric optics approximation to the WTE only includes the first two terms of Eq. (3.6), that is those that are wavelength independent [24]. Inclusion of the wavelength dependent terms of Eq. (3.6) can be used to predict the limitations of geometric optics in comparison to the more exact diffraction model.

By considering the CDF of photon arrival at the aperture, $C(x,0)$, and taking a Taylor series expansion around $(x,0)$ and then substituting the ITE and WTE, the slope at a point in the wavefront can be shown to be linearly related to the displacement, Δx, of a photon from that point in the wavefront [25]

$$\frac{\partial W(x,0)}{\partial x} = \frac{\Delta x}{z}. \tag{3.7}$$

This linear relationship between wavefront slope and displacement is an important one and underlies the majority of wavefront sensing schemes.

3.1.2 Fourier optics

The geometric optics model of light is sufficient for a first approximation of optical problems. However, the geometric optics model cannot explain the diffraction and interference of light. By considering light to propagate as a wave rather than as photons, the Fourier optics model can explain these phenomena.

Diffraction

Any monochromatic electromagnetic wave $u(x, y, z, t)$ at position (x, y, z) and time t can be expressed by [26]

$$u(x, y, z, t) = \mathrm{Re}[U(x, y, z) \exp[-j\phi(x, y, z)] \exp[-j2\pi\omega t]] \tag{3.8}$$

where ω is the frequency of the wave, $\phi(x, y, z)$ is the phase of the wave and $U(x, y, z)$ is the magnitude of the wave. In the following sections $\mathbf{U}(x, y, z)$ is used for compactness to represent $U(x, y, z) \exp[-j\phi(x, y, z)]$. $u(x, y, z, t)$ must satisfy the scalar wave equation

$$\nabla^2 u - \frac{1}{c^2} \frac{\partial^2 u}{\partial t^2} = 0 \tag{3.9}$$

where ∇^2 is the Laplacian operator defined by

$$\nabla^2 = \frac{\partial^2}{\partial x^2} + \frac{\partial^2}{\partial y^2} + \frac{\partial^2}{\partial z^2}. \tag{3.10}$$

By substituting $\mathbf{U}(x, y, z)$ into Eq. (3.9) the time-independent wave equation, known as Helmholtz's equation, can be derived

$$(\nabla^2 + k^2)\mathbf{U} = 0, \tag{3.11}$$

where k is the wavenumber defined as $2\pi/\lambda$, and λ is the wavelength of light.

The diffraction problem is illustrated in Fig. 3.7. An optical field incident on the aperture, with coordinate system (x_0, y_0), is propagated to the observation plane, with coordinates (u, v), a distance z away from the aperture plane. The distance between a given point in the aperture plane, (u, v), and a point in the observation plane, (x_0, y_0), is denoted as r. Application of the Helmholtz equation and Green's theorem to the problem leads to the Rayleigh-Somerfield diffraction formula which describes the wavefront in the observation plane [26]

$$\mathbf{U}(u, v, z) = \frac{1}{j\lambda} \int_{-\infty}^{\infty} \int_{-\infty}^{\infty} \mathbf{U}(x_0, y_0, 0) \frac{\exp[jkr]}{r} \cos(\theta) \mathrm{d}x_0 \mathrm{d}y_0, \tag{3.12}$$

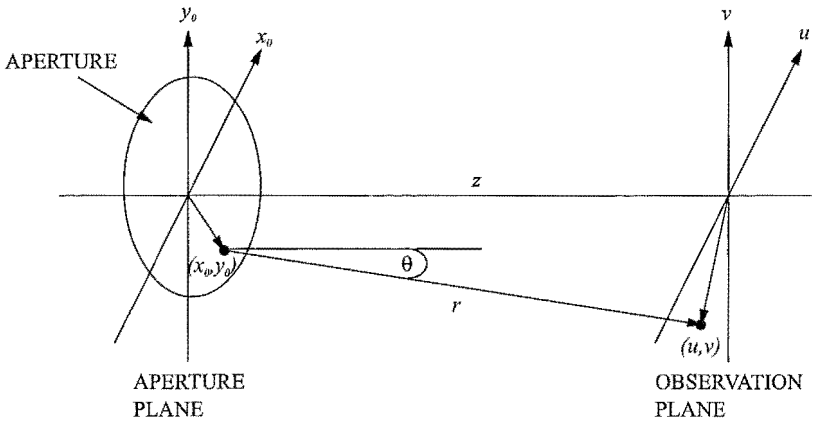

Figure 3.7 The diffraction problem - determining the optical field at (u, v, z) from the incident field on the aperture at $(x_0, y_0, 0)$.

where θ is the angle between z and r. Eq. (3.12) can also be expressed as

$$\mathbf{U}(u,v,z) = \int_{-\infty}^{\infty}\int_{-\infty}^{\infty} \mathbf{U}(x_0,y_0,0)h(u,v;x_0,y_0)\mathrm{d}x_0\mathrm{d}y_0, \tag{3.13}$$

where

$$h(u,v;x_0,y_0) = \frac{1}{j\lambda}\frac{\exp[jkr]}{r}\cos(\theta) \tag{3.14}$$

is the free space propagation impulse response. Eq. (3.13) is the mathematical definition of the Huygens-Fresnel principle, which states that the optical field in the observation plane can be expressed as a summation of spherical waves, $\exp[jkr]/r$, produced by an array of point sources located in the aperture. The distance r is given exactly from geometric considerations by

$$\begin{aligned} r &= \sqrt{z^2+(x_0-u)^2+(y_0-v)^2} \\ &= z\sqrt{1+\left(\frac{x_0-u}{z}\right)^2+\left(\frac{y_0-v}{z}\right)^2} \end{aligned} \tag{3.15}$$

The Rayleigh-Sommerfield diffraction formula can be difficult to use mathematically, and a number of approximations have been made for r to simplify the computation. The most useful of these are the Fresnel (near-field) and Fraunhofer (far-field) approximations.

Fresnel diffraction

The Fresnel diffraction formula is derived by approximating the spherical wavefronts of the Huygens-Fresnel principle with parabolic wavefronts. Mathematically, the first assumption is that the distance z between the two planes of interest is much greater than the extents of either plane. This means that the angle θ is negligibly small and consequently

$\cos(\theta) \approx 1$. The distance r between the points of interest in the two planes can be approximated by z, that is $r \approx z$. However, the r term cannot be replaced by z in the exponential. This is because a small approximation error in r can result in a large error in the phase when multiplied by k, which is large. The r term in the exponential can be simplified by the use of the binomial expansion

$$\begin{aligned}\sqrt{1+x} &= 1+\frac{1}{2}x-\frac{1}{8}x^2+\ldots \\ &\approx 1+\frac{1}{2}x.\end{aligned} \tag{3.16}$$

Using the first two terms of the binomial expansion on Eq. (3.15) yields

$$r \approx z\left(1+\frac{1}{2}\left(\frac{x_0-u}{z}\right)^2+\frac{1}{2}\left(\frac{y_0-v}{z}\right)^2\right) \tag{3.17}$$

These assumptions allow h for Fresnel diffraction to be expressed as

$$h(u,v;x_0,y_0) = \frac{\exp[jkz]}{j\lambda z}\exp\left[\frac{jk}{2z}\left((x_0-u)^2+(y_0-v)^2\right)\right]. \tag{3.18}$$

The optical field in the observation plane for Fresnel diffraction is then

$$\mathbf{U}(u,v,z) = \frac{\exp[jkz]}{j\lambda z}\int_{-\infty}^{\infty}\int_{-\infty}^{\infty}\mathbf{U}(x_0,y_0,0)\exp\left[\frac{jk}{2z}\left((x_0-u)^2+(y_0-v)^2\right)\right]\mathrm{d}x_0\mathrm{d}y_0. \tag{3.19}$$

Eq. (3.19) is said to be accurate when the separation between the planes satisfies

$$z^3 \gg \frac{\pi}{4\lambda}[(x_0-u)^2+(y_0-v)^2]^2_{\max}. \tag{3.20}$$

Expanding the quadratic terms in Eq. (3.19) yields

$$\begin{aligned}\mathbf{U}(u,v,z) &= \frac{\exp[jkz]}{j\lambda z}\exp\left[\frac{jk}{2z}(u^2+v^2)\right] \\ &\times \int_{-\infty}^{\infty}\int_{-\infty}^{\infty}\mathbf{U}(x_0,y_0,0)\exp\left[\frac{jk}{2z}\left(x_0^2+y_0^2\right)\right]\exp\left[-\frac{jk}{z}\left(x_0u+y_0v\right)\right]\mathrm{d}x_0\mathrm{d}y_0,\end{aligned} \tag{3.21}$$

which means that the optical field in the observation plane, $\mathbf{U}(u,v,z)$, is given by the Fourier transform of $\mathbf{U}(x_0,y_0,0)\exp[(jk/2z)(x_0^2+y_0^2)]$ evaluated at $(u/\lambda z, v/\lambda z)$ multiplied by complex exponential scalars.

The Fresnel diffraction model is employed when the wavefront is not propagated all the way to the focal plane, such as with the curvature wavefront sensor. Also, the Fresnel model is used when simulating scintillation as discussed in Section 3.2.5.

Fraunhofer diffraction

The Fraunhofer, or far field, diffraction model arises when the spherical wavefronts of the Huygens-Fresnel principle, or the parabolic wavefronts of the Fresnel model, are replaced with planar wavefronts. This model holds when the separation between the planes is

$$z \gg \frac{k(x_0^2 + y_0^2)_{\max}}{2}. \tag{3.22}$$

For a 1 metre aperture imaging in the visible ($\lambda = 589$ nm), this corresponds to an observation distance of more than 2700 km. The quadratic phase term, $(x_0^2 + y_0^2)$, of the integrand of Eq. (3.21) can be replaced by unity to model the planar wavefronts and becomes

$$\begin{aligned} \mathbf{U}(u,v,z) &= \frac{\exp[jkz]}{j\lambda z} \exp\left[\frac{jk}{2z}(u^2+v^2)\right] \\ &\times \int_{-\infty}^{\infty}\int_{-\infty}^{\infty} \mathbf{U}(x_0,y_0,0) \exp\left[-\frac{j2\pi}{\lambda z}(x_0 u + y_0 v)\right] \mathrm{d}x_0 \mathrm{d}y_0. \end{aligned} \tag{3.23}$$

With the change of coordinates $(x, y) = (x_0/\lambda z, y_0/\lambda z)$, Eq. (3.23) can be rewritten as

$$\begin{aligned} \mathbf{U}(u,v,z) &= \frac{\exp[jkz]}{j\lambda z} \exp\left[\frac{jk}{2z}(u^2+v^2)\right] \int_{-\infty}^{\infty}\int_{-\infty}^{\infty} \mathbf{U}(\lambda z x, \lambda z y, 0) \exp[-j2\pi(xu+yv)]\mathrm{d}x\mathrm{d}y \\ &= \frac{\exp[jkz]}{j\lambda z} \exp\left[\frac{jk}{2z}(u^2+v^2)\right] \mathcal{F}\Big[\mathbf{U}(\lambda z x, \lambda z y, 0)\Big]. \end{aligned} \tag{3.24}$$

which shows the optical field at the observation plane is the Fourier transform of the optical field at the aperture multiplied by complex exponential scalars.

The observed intensity at the measurement plane is given by

$$\begin{aligned} I(u,v) &= \Big|\mathbf{U}(u,v,z)\Big|^2 \\ &\propto \Big|\mathcal{F}\Big[\mathbf{U}(\lambda z x, \lambda z y, 0)\Big]\Big|^2. \end{aligned} \tag{3.25}$$

Eq. (3.25) shows the direct Fourier transform relationship between the observed intensity at the measurement plane and the complex field at the aperture plane. The Fraunhofer diffraction model, and the consequent Fourier transform relationship between the aperture and observation planes, are appropriate for astronomical imaging since by the time the wavefronts from stellar objects reach the earth's atmosphere they can be considered planar.

Lenses can be used to artificially propagate the wavefront large distances. When the observation plane is placed at the focal plane of the lens or lenslet array, the Fraunhofer diffraction model is employed to relate the complex field at the lenslet and measurement

plane.

Diffraction from an aperture

The diffraction patterns observed in the focal plane from apertures of various geometries can now be calculated using the Fraunhofer diffraction model. More specifically, rectangular and circular apertures are considered here. The former models most lenslet arrays and the latter telescope apertures. In order to calculate the diffraction patterns for these two aperture geometries the generalised aperture function, $A(x, y)$, needs to be introduced,

$$A(x,y) = \begin{cases} P(x,y)\exp[j\phi(x,y)] & \text{inside aperture} \\ 0 & \text{outside aperture,} \end{cases} \tag{3.26}$$

where $P(x, y)$ is the aperture function and $\phi(x, y)$ is the aperture phase which is a function of the wavefront aberrations. Firstly, a rectangular aperture is considered. The aberration-free aperture function is described by

$$P(x,y) = \text{rect}(x)\text{rect}(y). \tag{3.27}$$

Using the Fourier transform relationship derived in Section 3.1.2 for the fields in the aperture and focal planes, the diffraction pattern in the focal plane is

$$h(u,v) = \text{sinc}(u)\text{sinc}(v). \tag{3.28}$$

The observed intensity in the focal plane is the magnitude squared of the field in the focal plane,

$$|h(u,v)|^2 = \text{sinc}^2(u)\text{sinc}^2(v), \tag{3.29}$$

and is shown in Fig. 3.8(a). An example of this diffraction pattern arising from a rectangular aperture is the Shack-Hartmann wavefront sensor, which consists of an array of square lenslets placed in the aperture and is discussed in further detail in Section 4.1.1.

The aperture function for an aberration-free circular aperture of radius a is given by

$$P(x,y) = \begin{cases} 1 & x^2 + y^2 \leq a^2 \\ 0 & \text{otherwise.} \end{cases} \tag{3.30}$$

Due to the circular symmetry of the aperture function, it can be transformed into polar

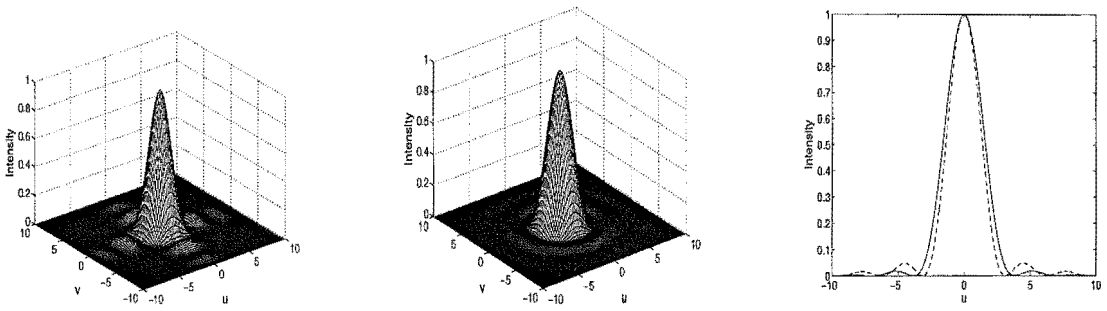

(a) (b) (c)

Figure 3.8 Fraunhofer diffraction patterns for (a) a square aperture and (b) a circular aperture. The cross-sections of the square (dotted) and circular apertures (solid) are plotted in (c).

coordinates

$$P(r) = \begin{cases} 1 & r \leq a \\ 0 & \text{otherwise.} \end{cases} \tag{3.31}$$

Since the aperture function is described by polar rather than Cartesian coordinates, the Hankel transform is used in place of the Fourier transform to find the Fraunhofer diffraction pattern,

$$h(\omega) = \frac{2J_1(\omega)}{\omega}, \tag{3.32}$$

where

$$\omega = \frac{2\pi}{\lambda}\frac{a}{z}\sqrt{u^2 + v^2}, \tag{3.33}$$

and $J_1(\omega)$ is a first order Bessel function of the first kind. The intensity seen at the observation plane is given by

$$|h(\omega)|^2 = \left(\frac{2J_1(\omega)}{\omega}\right)^2, \tag{3.34}$$

and is known as the Airy disk. The Airy disk is plotted in Fig. 3.8(b). Comparing the cross-sections of the two diffraction patterns in Fig. 3.8(c), it can be seen that main lobe widths for the two aperture geometries are very similar but the side lobes are higher for the sinc distribution of the square aperture. Also, the zero points of the Airy disk are not evenly spaced whereas they are for the sinc function. The distance between the zero-crossings decreases further away from the origin for the Airy disk as can be seen in Table 3.1.

ω	$\left(\frac{2J_1(\omega)}{\omega}\right)^2$	Max or Min
0	1	max
3.833	0	min
5.137	0.0175	max
7.015	0	min
8.416	0.0042	max
10.172	0	min
11.621	0.0016	max

Table 3.1 Locations of the first seven maxima and minima of the Airy disk. [26]

3.1.3 Rayleigh resolution limit

In astronomical imaging it is important to be able to resolve two different points in an object or two separate point sources, such as with a binary star. The resolution of an image, in the absence of turbulence, is limited by the diffraction effects introduced at the aperture. The Rayleigh resolution criterion states that two incoherent sources are "barely resolved" with a circular aperture when the centre of the Airy disk of the first point source falls exactly on the the first zero of the Airy disk corresponding to the second point source [26]. This scenario is shown in Fig. 3.9. The positions of the maxima and minima of the Airy disk diffraction pattern for a circular aperture are tabulated in Table 3.1. Substituting the first minima of Table 3.1 into Eq. (3.33) yields

$$3.833 = \frac{2\pi}{\lambda}\frac{a}{z}\omega_{\min}, \tag{3.35}$$

where $\omega_{\min}$ is the minimum separation required to satisfy the Rayleigh criterion. Rearranging Eq. (3.35) and solving for $\omega_{\min}$ gives

$$\omega_{\min} = 1.22\lambda F, \tag{3.36}$$

where $F = z/2a$ is the focal number of the system. For astronomical purposes it is preferable to specify the minimum angle of separation for resolution of two objects,

$$\alpha_{\min} = 1.22\frac{\lambda}{D}, \tag{3.37}$$

where D is the telescope diameter.

It should be noted that Rayleigh's resolution criterion relates to diffraction-limited point

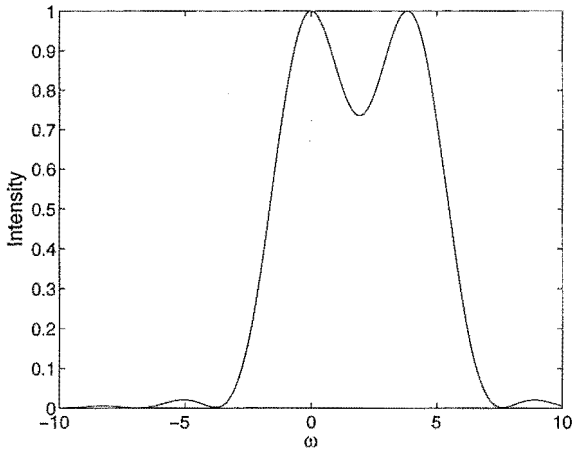

Figure 3.9 The summation of two diffraction patterns separated by the Rayleigh resolution distance arising from two point sources imaged through a circular aperture.

sources. For objects partially compensated with adaptive optics, the intensity pattern has a characteristic core and halo structure (see Section 3.3.3) and so a different resolution criterion is required to distinguish one object's core from another's halo. Also, if strong prior information exists, for example that the object is a binary rather than single star, then resolution far below the Rayleigh limit is possible.

Although it is generally accepted that the resolution attainable by an imaging system is limited by the diffraction limit, it is theoretically possible for certain spatially bounded objects to attain resolution beyond this limit. Resolution beyond the classical diffraction limit is known as super-resolution or bandwidth extrapolation [26].

3.1.4 Coherent and incoherent sources

In order to understand imaging more fully, it is necessary to make the distinction between coherent and incoherent illumination. Coherent illumination implies the optical field is perfectly correlated or deterministic [20]. Thus all the object points have a fixed phase relationship. Coherent sources are linear in complex amplitude and so the response of each object point can be added on a complex amplitude basis. An example of a coherent source is a laser.

The most common form of photon creation occurs when an atom reverts from a higher state to a lower energy state with the excess energy used to emit the photon. The direction and phase of the emitted photon is random. A spatially incoherent source is one that is illuminated with this random photon emission. Examples of incoherent sources are self-luminous objects such as stars and the objects illuminated by them. Therefore the topic of this thesis, astronomical imaging, involves the study of incoherent imaging. Incoherent

imaging is linear in intensity, in contrast to coherent imaging which is linear in complex amplitude.

Firstly, coherent imaging is examined. The output, $\mathbf{u}_{\text{out}}(u,v)$, of a coherent field passing through a system with an impulse response $h(u,v)$ is

$$\mathbf{u}_{\text{out}}(u,v) = \mathbf{u}_{\text{in}}(u,v) \odot h(u,v). \tag{3.38}$$

Taking the Fourier transform of Eq. (3.38) gives

$$\mathbf{U}_{\text{out}}(x,y) = \mathbf{U}_{\text{in}}(x,y)H(x,y), \tag{3.39}$$

where $H(x,y)$ is the coherent transfer function, which can be further described by

$$\begin{aligned} H(x,y) &= \mathcal{F}\{h(u,v)\} \\ &= \mathcal{F}\{\mathcal{F}\{A(\lambda z x, \lambda z y)\}\} \\ &= A(-\lambda z x, -\lambda z y). \end{aligned} \tag{3.40}$$

Thus the coherent transfer function is simply the generalised aperture function rotated by 180 degrees. The observed intensity is the magnitude squared of $\mathbf{u}_{\text{out}}(u,v)$.

With incoherent illumination, the measured intensity at each point is assumed to be independent of all other points. Incoherent illumination is linear in intensity, so the intensity at each point can be added. The total intensity is therefore described by

$$i(u,v) = \mathbf{u}_{\text{in}}(u,v) \odot |h(u,v)|^2. \tag{3.41}$$

Taking the Fourier transform of Eq. (3.41) and invoking the convolution theorem yields

$$I(x,y) = \mathbf{U}_{\text{in}}(x,y)\mathcal{H}(x,y), \tag{3.42}$$

where the upper case quantities are the Fourier transforms of the respective lower case ones. $\mathcal{H}(x,y)$ represents the incoherent transfer function and is known as the optical transfer function (OTF) [20]. Using Eq.s (3.41) and (3.42), and the autocorrelation theorem allows the OTF to be defined

$$\begin{aligned} \mathcal{H}(x,y) &= \mathcal{F}\{|h(u,v)|^2\} \\ &= A(\lambda z x, \lambda z y) \otimes A(\lambda z x, \lambda z y). \end{aligned} \tag{3.43}$$

Eq. (3.43) shows that the OTF is given by the autocorrelation of the generalised aperture function. The absolute value of the OTF is defined as the magnitude transfer function (MTF) and is bounded between 0 and 1. The MTF is a measure of how well the imaging

system transfers the different spatial frequencies between the object and image, with 1 representing a perfect transfer [27]. The Fourier transform of the OTF is defined as the point spread function (PSF), $s(u,v) = |h(u,v)|^2$. Mathematically, the OTF is a Fourier transform of a real positive valued function, $s(u,v)$.

3.1.5 OTFs and PSFs

The OTFs and PSFs with incoherent imaging are now analysed for the cases of rectangular and circular apertures, of focal length f. Firstly, for a rectangular aperture of dimension $D_x \times D_y$, the OTF can be shown to be [20]

$$\mathcal{H}(x,y) = \mathrm{tri}\left(\frac{\lambda f x}{D_x}\right)\mathrm{tri}\left(\frac{\lambda f y}{D_y}\right), \tag{3.44}$$

where the triangular function is as defined in Section 2.2. The corresponding PSF is given by [20]

$$s(u,v) = \frac{D_x D_y}{(\lambda f)^2}\mathrm{sinc}^2\left(\frac{uD_x}{\lambda f}\right)\mathrm{sinc}^2\left(\frac{vD_y}{\lambda f}\right), \tag{3.45}$$

where the sinc function is also defined in Section 2.2. These expressions for the OTF and PSF for a rectangular aperture are plotted in Fig. 3.10 (a) and (b) respectively. For a circular aperture of diameter D, the OFT is given in polar coordinates by [20]

$$\mathcal{H}(r) = \begin{cases} \frac{2}{\pi}\left[\cos^{-1}\left(\frac{\lambda f r}{D}\right) - \frac{\lambda f r}{D}\sqrt{1-\left(\frac{\lambda f r}{D}\right)^2}\right] & r \leq \frac{D}{\lambda f} \\ 0 & \text{otherwise.} \end{cases} \tag{3.46}$$

and the corresponding PSF, also in polar coordinates, by [20]

$$s(\rho) = \frac{4J_1^2\left(\frac{\rho D}{2\lambda f}\right)}{\rho^2}, \tag{3.47}$$

where $J_1(\rho)$ is a first order Bessel function of the first kind. The OTF and PSF for the circular aperture are shown in Fig. 3.10 (c) and (d) respectively.

3.2 Kolmogorov turbulence

Wavefronts become distorted as they pass through the atmosphere due to the randomly time-varying layers of air of differing temperature, and hence refractive index [20]. The atmosphere thus acts as a collection of random time-varying lenses. The spatial statistics of the turbulent air motion were first derived by Kolmogorov [19]. Tatarskii extended

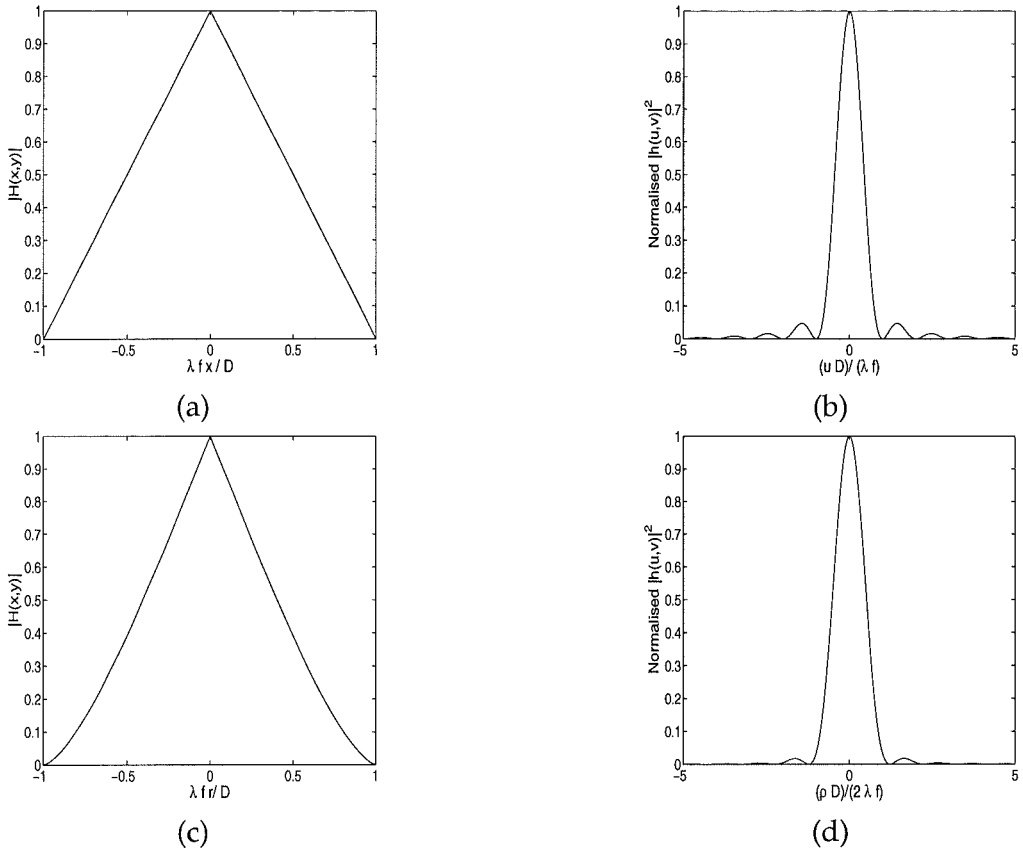

Figure 3.10 For a square aperture of dimension D, the (a) OTF and (b) PSF. For a circular aperture of diameter D, the (c) OTF and (d) PSF.

Kolmogorov's results to include an analysis of the statistics of refractive index fluctuations [28], which are outlined in this section.

The variance of the velocity of Kolmogorov turbulence is infinite. To overcome the problem of an infinite covariance, the structure function, introduced in Section 2.7.1, is used. Kolmogorov argued that the velocity structure function should be expressible as a constant times a function, $f()$, of the separation between two points, R_1 and R_2. The velocity structure function with Kolmogorov's assumptions is given by

$$D_v(R_1 - R_2) = \alpha f(|R_1 - R_2|/\beta), \tag{3.48}$$

where α and β are constants. Kolmogorov's dimensionality argument states that since β is a normalisation constant, it must have units of distance (m) and therefore α must have units of velocity squared (m^2s^{-2}). Turbulent flow is governed by only two parameters, the energy density ϵ (m^2s^{-3}), and kinematic viscosity ν (m^2s^{-1}). Kolmogorov realised that the only way to combine these two parameters and satisfy the dimensionality criterion was by

setting

$$\alpha = \nu^{1/2}\epsilon^{1/2} \qquad \text{and} \qquad \beta = \nu^{3/4}\epsilon^{-1/4}. \tag{3.49}$$

The velocity structure function, in terms of the turbulent flow parameters, is therefore

$$D_v(R_1 - R_2) = \nu^{1/2}\epsilon^{1/2} f(|R_1 - R_2|\nu^{-3/4}\epsilon^{1/4}). \tag{3.50}$$

Kolmogorov developed his model further by noting that energy is input to the atmosphere by solar heating at the outer scale, L_0, which is typically of the order of tens of metres [20]. This energy then cascades through finer and finer spatial scales so that eventually, at the inner scale l_0 (typically millimetres), the velocity gradient is so large that energy is converted to heat by viscous dissipation. Kolmogorov postulated that the kinematic viscosity, ν, plays no role in determining the velocity structure function for this regime of spatial distances between the inner and outer scales. The only way for the ν-dependance to drop out is for $f(|R_1 - R_2|/\beta)$ to obey a two-thirds power law, so that the velocity structure function is

$$D_v(R_1 - R_2) \propto \epsilon^{2/3}|R_1 - R_2|^{2/3} \qquad l_0 < |R_1 - R_2| < L_0. \tag{3.51}$$

This dimensional argument leading to the two-thirds power law is the basis for the equations governing Kolmogorov turbulence. Experimental evidence does strongly support this power law for the velocity structure function in turbulent flow over the appropriate range of spatial distances [28].

Velocity and velocity variations do not in themselves affect the propagation of light through the atmosphere. Instead it is the differences in the refractive index, $n(R_1 - R_2)$, in the path of the wavefront that cause the aberrations. Tatarski proposed that a similar two-thirds power law to the velocity structure function defined the temperature structure function,

$$D_T(R_1 - R_2) = C_T^2|R_1 - R_2|^{2/3} \qquad l_0 < |R_1 - R_2| < L_0, \tag{3.52}$$

where C_T^2 is the temperature structure constant, which is determined experimentally. This relationship has subsequently been validated experimentally [28]. Since there are no pressure induced atmospheric density variations, the atmospheric density is essentially inversely proportional to the absolute temperature. The refractive index deviations from unity are proportional to the density, which means the refractive index structure function also follows the two-thirds power law

$$D_n(R_1 - R_2) = C_n^2(z)|R_1 - R_2|^{2/3}, \tag{3.53}$$

where $C_n^2(z)$ is the refractive index structure constant and its value is highly dependent on

the altitude, z. The power spectrum of these refractive index fluctuations, Φ_n, was shown by Tatarski to be

$$\Phi_n(\boldsymbol{\kappa}) = 0.033 C_n^2 \boldsymbol{\kappa}^{-11/3} \qquad 2\pi/L_0 < 2\pi/|R_1 - R_2| < 2\pi/l_0 \tag{3.54}$$

where $\boldsymbol{\kappa}$ is the spatial wavenumber vector $(\kappa_x, \kappa_y, \kappa_z)$. Eq. (3.54) only holds in the bounds stated. The modified von Karman power spectrum includes the effects of the finite inner and outer scales

$$\Phi_n(\boldsymbol{\kappa}) = \frac{0.033 C_n^2}{(\boldsymbol{\kappa}^2 + \kappa_0^2)^{11/6}} \exp\left(-\frac{\boldsymbol{\kappa}^2}{\kappa_m^2}\right), \tag{3.55}$$

where κ_0 is $2\pi/L_0$ and κ_m is $5.92/l_0$.

It is the fluctuations of the phase of the wavefront which are of interest in astronomical imaging. Roddier [33] showed that the covariance function, $C(\mathbf{x}')$, of the complex amplitude of a wave, $U(\mathbf{x})$, with coordinates $\mathbf{x} = (x, y)$, that has passed through Kolmogorov turbulence is

$$\begin{aligned} C(\mathbf{x}') &= \langle U(\mathbf{x}) U^*(\mathbf{x} + \mathbf{x}') \rangle \\ &= \exp\left[-\frac{1}{2} D_\phi(\mathbf{x}')\right], \end{aligned} \tag{3.56}$$

where $D_\phi(\mathbf{x}')$ is the phase structure function. This is in turn given by

$$\begin{aligned} D_\phi(\mathbf{x}') &= 2.91 k^2 \sec(\gamma) |\mathbf{x}'|^{5/3} \int_0^\infty C_n^2(z) \mathrm{d}z \\ &= 6.88 \left(\frac{|\mathbf{x}'|}{r_0}\right)^{5/3} \end{aligned} \tag{3.57}$$

where γ is the zenith angle (angle of observation measured from the zenith), and r_0 is the Fried parameter [29], also known as the seeing size. Physically, Fried described his parameter as the aperture which has the "same resolution" as a diffraction-limited aperture in the absence of turbulence. Typical values for r_0 range from 10-20 cm in the visible region of the spectrum. The Fried parameter can therefore be defined by

$$r_0 = \left(\frac{2.91}{6.88} k^2 \sec(\gamma) \int_0^\infty C_n^2(z) \mathrm{d}z\right)^{-3/5}. \tag{3.58}$$

Fried's parameter is proportional to the six-fifths power of the wavelength

$$r_0 \propto \lambda^{6/5}. \tag{3.59}$$

As the wavelength increases, so does r_0, and therefore the seeing improves. The wavefront

aberration is achromatic (independent of wavelength) so the number of microns of optical path retardance is the same for all wavelengths of light. However, there are fewer waves of retardance at the longer wavelengths. This means the effect of atmospheric turbulence is more severe for ultra violet and less severe for infra-red light than it is for visible light.

The power spectrum of the phase fluctuations given by the phase structure function of Eq. (3.57) is [19]

$$\Phi_\phi(\boldsymbol{\kappa}) = 0.023 r_0^{-5/3} |\boldsymbol{\kappa}|^{-11/3}. \tag{3.60}$$

Eq. (3.60) is strongly supported by experimental observations [28]. The phase fluctuations induced by the atmosphere are fractal in nature [30]. This independence to scale cannot be represented by classical geometry, and is apparent when written as

$$\Phi_\phi(\alpha\boldsymbol{\kappa}) = \alpha' \Phi_\phi(\boldsymbol{\kappa}). \tag{3.61}$$

3.2.1 Temporal behaviour of Kolmogorov turbulence

The turbulence in the atmosphere is continually changing, so a knowledge of the temporal statistics of Kolmogorov turbulence is essential to compensate for it. The basic model for studying the time-varying statistics of the atmosphere is the Taylor hypothesis [19]. Taylor's hypothesis states that the atmosphere can be modelled as distinct layers of turbulence. Furthermore, each layer (at altitude z) is travelling perpendicularly to the earth's surface at a velocity $v(z)$. If the layer simply moves through the atmosphere without changing its refractive index properties, then the phase contribution of that layer also simply moves across the telescope aperture. The temporal power spectrum of the phase in the telescope aperture, $\Phi_\phi(f)$, for only one layer of turbulence in the Taylor hypothesis is [19]

$$\Phi_\phi(f) \propto \int_0^\infty \frac{1}{v} \left(\frac{f}{v}\right)^{-8/3} C_n^2(z) \mathrm{d}z. \tag{3.62}$$

Thus there is a -8/3 power law dependence of the phase on the frequency f at any point in the aperture. The approximate frequency of a control loop required to overcome the time variations in the atmosphere is known as the Greenwood frequency, f_G. For the Taylor hypothesis, the Greenwood frequency is given by [27]

$$f_G = 2.31 \lambda^{-6/5} \left[\sec(\gamma) \int_0^\infty (v(z))^{5/3} C_n^2(z) \mathrm{d}z \right]^{3/5}. \tag{3.63}$$

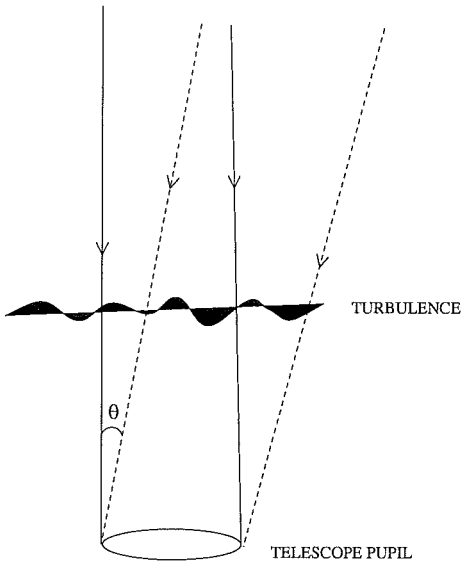

Figure 3.11 Angular anisoplanatism. [36]

For a single layer of turbulence, Eq. (3.63) reduces to

$$f_G = 0.43\frac{v}{r_0}. \tag{3.64}$$

In the visible spectrum the Greenwood frequency is approximately 40Hz [28]. Since the Greenwood frequency is inversely proportional to r_0, it is inversely proportional to wavelength to the six-fifths (ie $f_G \propto \lambda^{-6/5}$).

3.2.2 Angular anisoplanatism

When imaging a faint object, a nearby bright star is often observed so that the wavefront sensor can receive enough light to make an accurate estimate of the atmospheric turbulence. This off-axis viewing of the true object is known as angular anisoplanatism and is shown in Fig. 3.11. The isoplanatic angle, θ_0, is the angle between an object and guide star that would result in a mean square phase error of 1 rad^2. The isoplanatic angle is given by [19]

$$\theta_0 = \left[2.91k^2 \sec^{8/3}(\gamma) \int_0^\infty C_n^2(z) z^{5/3} \mathrm{d}z\right]^{-3/5} \tag{3.65}$$

The isoplanatic angle, like Fried's parameter r_0, is dependent on wavelength to the six-fifths ($\theta_0 \propto \lambda^{6/5}$). The mean squared wavefront error, σ_θ^2, resulting from observing a science

object an angle θ away from the guide star is

$$\sigma_\theta^2 = \left(\frac{\theta}{\theta_0}\right)^{5/3}. \tag{3.66}$$

In the visible and for a typical Fried parameter of 10cm and a single layer of turbulence at 5km, the isoplanatic angle is only 1.3 arcseconds. The consequence of this small isoplanatic angle is the low probability that a natural guide star will exist for a given astronomical object.

3.2.3 Summary of important turbulence parameters

The dependence on wavelength and zenith angle of the three important parameters discussed in the previous subsections: Fried's parameter, the Greenwood frequency and the isoplanatic angle are summarised in Table 3.2.

Parameter	Wavelength (λ)	Zenith angle (γ)
Fried's parameter (r_0)	$\lambda^{6/5}$	$(\cos\gamma)^{3/5}$
Greenwood frequency (f_G)	$\lambda^{-6/5}$	$(\cos\gamma)^{-3/5}$
Isoplanatic angle (θ_0)	$\lambda^{6/5}$	$(\cos\gamma)^{8/5}$

Table 3.2 The wavelength and zenith angle dependence of turbulence related parameters.

3.2.4 Zernike polynomials

In order to compensate for the atmospheric turbulence, it is necessary to estimate the phase of the wavefront at the telescope aperture. The wavefront phase can be estimated at each point in the aperture, but this is computationally intensive. An alternative method is to represent the phase over the aperture as a sum of basis functions $\Psi(x, y)$. Given a statistical model of the turbulence, the choice of basis functions is not important so long as the set is complete; that is the wavefront phase distortion, $\phi(u, v)$, can be represented by

$$\phi(x, y) = \sum_{i=1}^{\infty} a_i \Psi_i(x, y), \tag{3.67}$$

where a_i is the coefficient of the i^{th} basis function. The discussion of the optimal estimation of the coefficients of the basis functions from the wavefront sensing measurements is made in Section 4.2. In this section, a specific set of basis polynomials used to model the wavefront, the Zernikes, is discussed.

The optimal set of basis functions to describe a wavefront aberrated by Kolmogorov turbulence is the Karhunen-Loève expansion, for which the coefficients, a_i, in Eq. (3.67) are statistically independent [31]. The Karhunen-Loève functions cannot be calculated analytically and instead are usually found by diagonalising the covariance matrix of a set of analytic polynomials. Although the low order Zernike polynomials are weakly correlated, they provide a good approximation to the Karhunen-Loève expansion. As a result, they are often used to describe wavefronts aberrated by Kolmogorov turbulence due to their simple analytic expressions.

The Zernike set of polynomials are defined on the unit circle and hence are often suitable for optical purposes since most apertures are also circular. The Zernike polynomials are orthogonal over the unit circle. The use of Zernike basis polynomials to model atmospheric turbulence was first proposed by Fried [32]. The advantage of Zernike polynomials when used to model wavefronts is that the first few modes represent the classical optical aberrations of tip, tilt, defocus, astigmatism etc. The Zernikes are usually described by polar coordinates, (r, θ), as the product of radial and angular terms. Using the ordering system devised by Noll [34], the Zernike polynomials are defined by

$$\begin{aligned} Z_{\text{even } i}(r,\theta) &= \sqrt{n+1}R_n^m(r)\sqrt{2}\cos(m\theta), \quad m \neq 0 \\ Z_{\text{odd } i}(r,\theta) &= \sqrt{n+1}R_n^m(r)\sqrt{2}\sin(m\theta), \quad m \neq 0 \\ Z_i(r) &= R_n^0(r), \quad m = 0, \end{aligned} \tag{3.68}$$

where

$$R_n^m(r) = \sum_{s=0}^{(n-m)/2} \frac{(-1)^s(n-s)!}{s![(n+m)/2-s]![(n-m)/2-s]!} r^{n-2s}. \tag{3.69}$$

The values of n, the radial order, and m, the azimuthal order, are always integral and must satisfy $m \leq n$, and $n - |m|$ is always even. The index i is used for ordering the polynomials and is a function of n and m.

The wavefront phase, $\phi(Rr, \theta)$, can then be written as a weighted sum of the Zernike polynomials over an aperture of radius R by

$$\phi(Rr,\theta) = \sum_{i=1}^{\infty} a_i Z_i(r,\theta) \tag{3.70}$$

where a_i is the coefficient of the i^{th} polynomial, Z_i, and is defined by

$$a_i = \frac{1}{\pi}\int_0^{2\pi}\int_0^R W(\rho)\phi(R\rho,\theta)Z_i(\rho,\theta)\rho \mathrm{d}\rho \mathrm{d}\theta \tag{3.71}$$

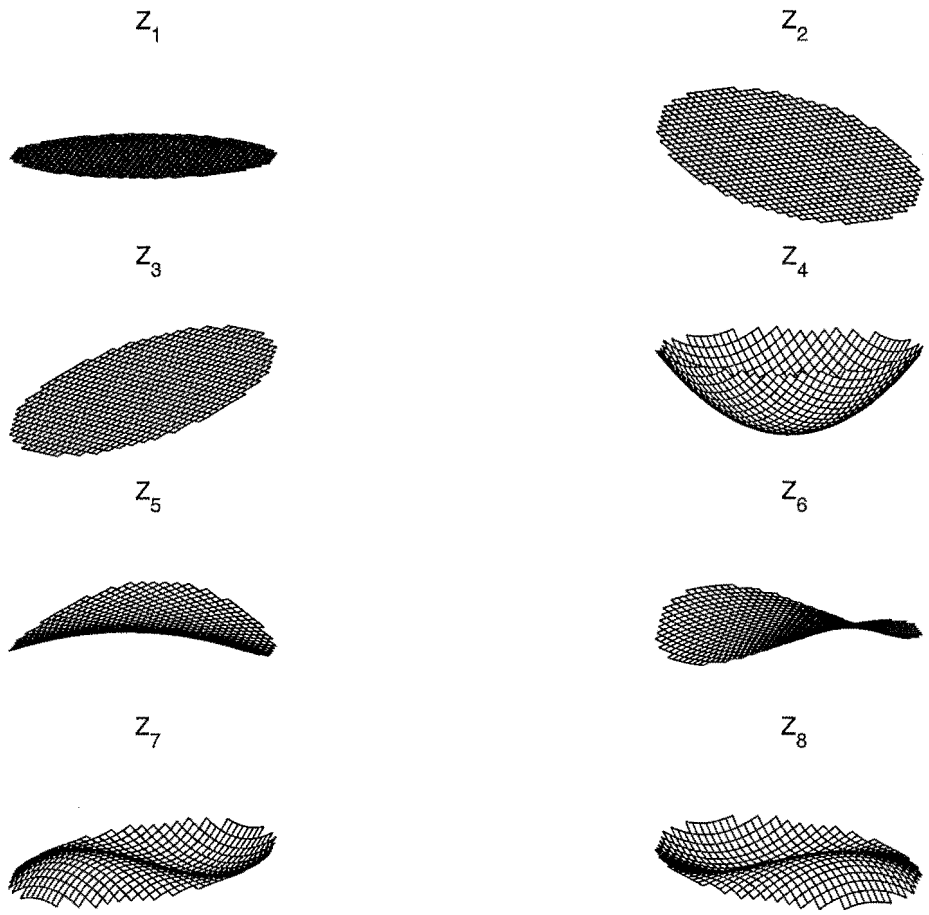

Figure 3.12 First eight Zernike polynomials. Z_1 = piston, Z_2 = tip, Z_3 = tilt, Z_4 = defocus, Z_5, Z_6 = astigmatism, Z_7, Z_8 = coma. [8]

where $\rho = r/R$ is the normalised radial coordinate, and $W(\rho)$ is a unit volume weighting function

$$W(\rho) = \begin{cases} \frac{1}{\pi} & \rho \leq 1 \\ 0 & \rho > 1. \end{cases} \tag{3.72}$$

The first eight Zernike polynomials and their classical optical aberration names are displayed in Fig. 3.12. The first mode is piston, which does not affect the images captured by a telescope, and is therefore not included in the analysis of atmospheric turbulence. The second and third modes, tip and tilt, comprise 87 percent [32] of the energy of the wavefront aberration caused by atmospheric turbulence. These modes produce random motion of the images formed in the image plane, but do not affect the spatial resolution of the image.

Z_j	Polynomial	Residual phase error (rad^2)
Z_1	1	$1.0299(D/r_0)^{5/3}$
Z_2	$2r\cos(\theta)$	$0.582(D/r_0)^{5/3}$
Z_3	$2r\sin(\theta)$	$0.134(D/r_0)^{5/3}$
Z_4	$\sqrt{3}(2r^2-1)$	$0.111(D/r_0)^{5/3}$
Z_5	$\sqrt{6}r^2\sin(2\theta)$	$0.0880(D/r_0)^{5/3}$
Z_6	$\sqrt{6}r^2\cos(2\theta)$	$0.0648(D/r_0)^{5/3}$
Z_7	$\sqrt{8}(3r^3-2r)\sin(\theta)$	$0.0587(D/r_0)^{5/3}$
Z_8	$\sqrt{8}(3r^3-2r)\cos(\theta)$	$0.0525(D/r_0)^{5/3}$
Z_9	$\sqrt{8}r^3\sin(3\theta)$	$0.0463(D/r_0)^{5/3}$
Z_{10}	$\sqrt{8}r^3\cos(3\theta)$	$0.0401(D/r_0)^{5/3}$

Table 3.3 The first ten Zernike polynomials and their residual phase errors. [34]

In practice, only a finite number of Zernike polynomials, I, are corrected

$$\phi_c = \sum_{i=1}^{I} a_i Z_i(r,\theta) \tag{3.73}$$

where ϕ_c is the wavefront correction. The mean squared residual phase error from the first I terms, Δ_I, is given by [19]

$$\begin{aligned}\Delta_I &= \int_{-\infty}^{\infty}\int_{-\infty}^{\infty} W(\rho)\langle[\phi(R\rho)-\phi_c(R\rho)]^2\rangle\rho\mathrm{d}\rho\mathrm{d}\theta \\ &= \langle\phi^2\rangle - \sum_{i=1}^{I}\langle|a_i^2|\rangle\end{aligned} \tag{3.74}$$

where $\langle\phi^2\rangle$ is the phase variance, which is infinite for the Kolmogorov spectrum. The residual phase errors for the first ten modes are tabulated in Table 3.3. For the higher order modes, $I > 10$, the residual error can be approximated by

$$\Delta_I \approx 0.2944 I^{-\sqrt{3}/2}\left(\frac{D}{r_0}\right)^{5/3}. \tag{3.75}$$

The covariance matrix for the first ten Zernike polynomials, excluding piston which has infinite variance, is shown in Table 3.2.4. The off-diagonal terms show the weak correlation between some of the modes such as tip and coma. In contrast, the covariance matrix of the optimal Karhunen-Loève expansion is diagonal.

	Z_2	Z_3	Z_4	Z_5	Z_6	Z_7	Z_8	Z_9	Z_{10}
Z_2	0.448	0	0	0	0	0	-0.0141	0	0
Z_3	0	0.448	0	0	0	-0.0141	0	0	0
Z_4	0	0	0.0232	0	0	0	0	0	0
Z_5	0	0	0	0.0232	0	0	0	0	0
Z_6	0	0	0	0	0.0232	0	0	0	0
Z_7	0	-0.0141	0	0	0	0.0618	0	0	0
Z_8	-0.0141	0	0	0	0	0	0.00618	0	0
Z_9	0	0	0	0	0	0	0	0.00618	0
Z_{10}	0	0	0	0	0	0	0	0	0.00618

Table 3.4 Covariance matrix for the first ten Zernike polynomials, excluding piston. Each entry must be multiplied by $(D/r_0)^{5/3}$. [20]

3.2.5 Simulation of Kolmogorov turbulence

Simulating the atmosphere is essential for an accurate simulation of the operation of an adaptive optic or computer post-processing astronomical imaging system. In practice, most methods for simulating the turbulence consist of generating a single phase screen located at the aperture of the optical system [35]. However, this approach cannot account for anisoplanatic effects. There are a number of different methods to generate phase screens that satisfy the spatial and temporal correlation properties of Kolmogorov turbulence, Eq.s (3.54) and (3.62). These include spectral methods that use the covariances of the von Karman or Kolmogorov spectra, modal expansions using basis functions such as the Zernikes, fractal methods, and direct simulation in terms of the Karhunen-Loève basis functions of the turbulence [36]. The method used to simulate Kolmogorov turbulence in this thesis is the mid-point displacement method of Harding *et al.* [35]. The Harding method is an extension of the direct simulation of the phase screen. The Harding method is chosen because of its accuracy in satisfying the Kolmogorov statistics and its reasonable computational complexity. A 32 × 32 pixel phase screen with D/r_0 of 16, generated using the method of Harding, is shown in Fig. 3.13(a) and the corresponding speckle image formed at the detector plane in Fig. 3.13(b).

The previous paragraph outlined how the phase aberration at the telescope can be generated with the mid-point displacement method. In some circumstances the magnitude of the wavefront aberration, the scintillation, also needs to be estimated. The scintillation at the telescope aperture can be simulated by propagating a phase screen, which can again be generated with the Harding method, from the chosen turbulence layer height to the telescope using Fresnel propagation.

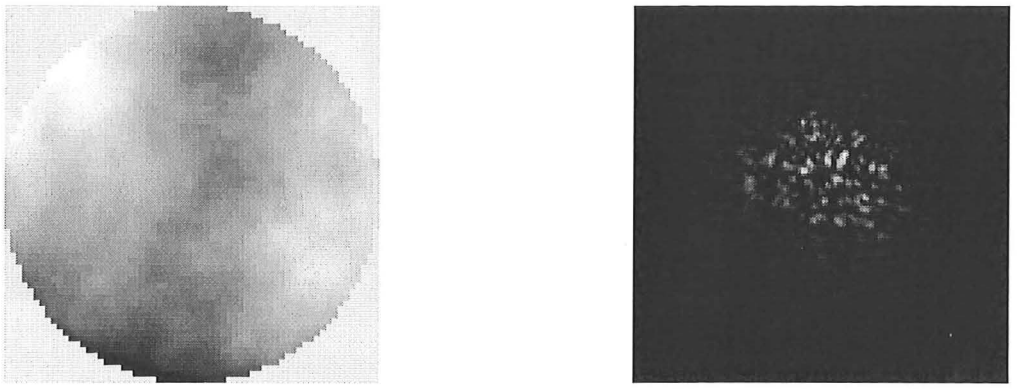

(a) (b)

Figure 3.13 (a) Phase screen of severity D/r_0=16 generated using the mid-point method. (b) The corresponding speckle image.

3.3 Imaging

In this section, a discussion of the fundamentals of imaging through Kolmogorov turbulence is made. Firstly, the difference between long and short exposure imaging through Kolmogorov turbulence is examined. A performance criterion for imaging through the atmosphere, the Strehl ratio, is then introduced. Finally, the section is completed with a discussion on objects partially compensated with the use of adaptive optics.

3.3.1 Long and short exposure imaging

Since the atmospheric turbulence is constantly changing in time, the exposure time of the image of an astronomical object affects the characteristic functions, the PSF and OTF, of the optical system. A short exposure image, such as shown in Fig. 3.14(b), is captured over a period of time less than the temporal correlation time of the atmosphere. The atmosphere is essentially frozen for a short exposure image. The short exposure images are displaced by the tip and tilt terms, Z_2 and Z_3, of the atmosphere.

A long exposure image is captured over a period of time much larger than the atmospheric temporal correlation time. The long exposure image is therefore the ensemble average of a large number of short exposure images. Similarly, the long exposure PSF is the ensemble average of the PSFs of the short exposure images. In contrast, the short exposure PSF can be considered to be the average of the short exposure PSFs if each image were centroided before averaging [19].

Fig. 3.14(c) shows a long exposure image which is the sum of 1000 short exposure images. The diffraction-limited image, which is simply the Fraunhofer diffraction pattern of a circular aperture, is also shown for comparison in Fig. 3.14(a). Short exposure imaging has the advantage that some of the high spatial frequency content is retained, which can then

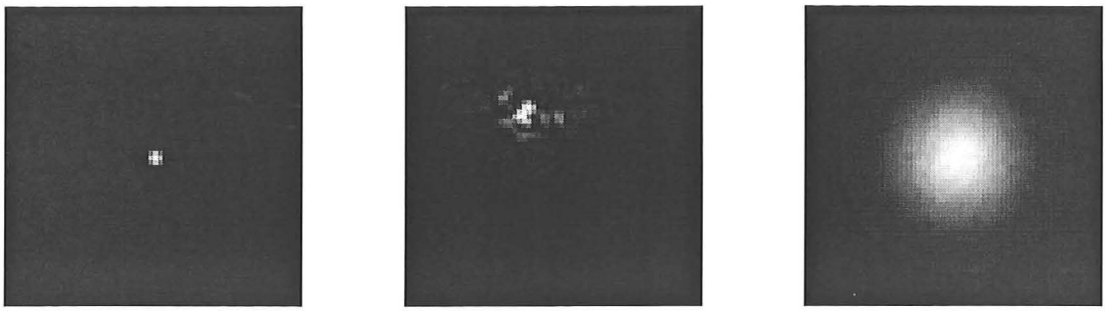

(a) (b) (c)

Figure 3.14 Simulated images of a single bright star observed through a circular aperture. (a) The diffraction-limited image, (b) a short exposure image, and (c) a long exposure image.

be used to reconstruct the object [37].

The long exposure transfer function can be shown to be the product of the covariance function of the atmospheric function defined in Eq. (3.56), $C(\lambda f x, \lambda f y)$, and the telescope OTF, $\mathcal{H}(\lambda f x, \lambda f y)$ [19]

$$\mathcal{H}_{LE}(x, y) = C(\lambda f x, \lambda f y)\mathcal{H}(\lambda f x, \lambda f y) \tag{3.76}$$

where the subscript denotes long exposure. The covariance of the atmosphere can be found by substituting Eq. (3.57) into Eq. (3.56) yielding,

$$C(\mathbf{x}) = \exp\left[-3.44\left(\frac{\lambda f|\mathbf{x}|}{r_0}\right)^{5/3}\right]. \tag{3.77}$$

The long exposure OTF for a circular aperture can then be found by substituting the OTF for a circular aperture, Eq. (3.46) and the atmospheric covariance function, Eq. (3.77), into Eq. (3.76)

$$\mathcal{H}_{LE}(r) = \frac{2}{\pi}\left[\cos^{-1}\left(\frac{\lambda f r}{D}\right) - \frac{\lambda f r}{D}\sqrt{1-\left(\frac{\lambda f r}{D}\right)^2}\right]\exp\left[-3.44\left(\frac{\lambda f|r|}{r_0}\right)^{5/3}\right]. \tag{3.78}$$

The long exposure OTFs for various D/r_0 ratios are plotted in Fig. 3.15(a). The long exposure PSF is the Fourier transform of Eq. (3.78) and is found computationally. The PSFs for short exposure imaging are plotted in Fig. 3.16(a) for the same D/r_0 ratios

The covariance of the atmosphere for the case of short exposure imaging was derived by Fried [29]

$$C(\mathbf{x}) = \exp\left[-3.44\left(\frac{\lambda f|\mathbf{x}|}{r_0}\right)^{5/3}\left(1-\left(\frac{\lambda f|\mathbf{x}|}{D}\right)^{1/3}\right)\right]. \tag{3.79}$$

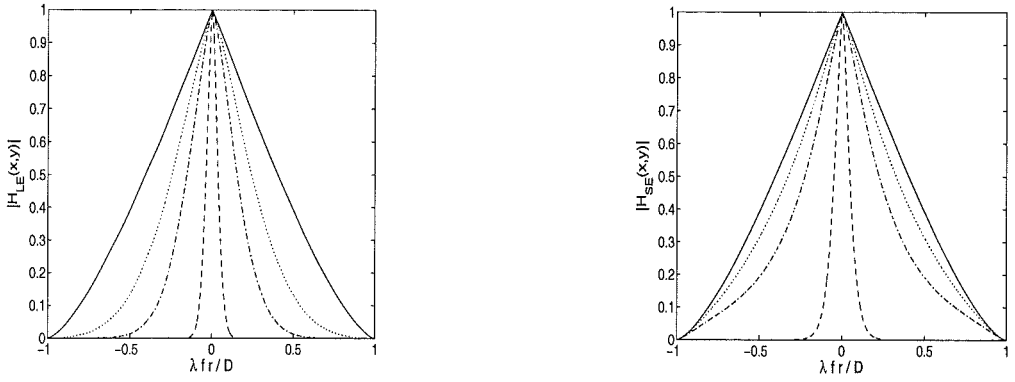

(a) (b)

Figure 3.15 For a circular aperture, the (a) long exposure OTFs and (b) short exposure OTFs for D/r_0 ratios of 0 (solid), 1 (dotted), 2 (dashed-dotted) and 10 (dashed).

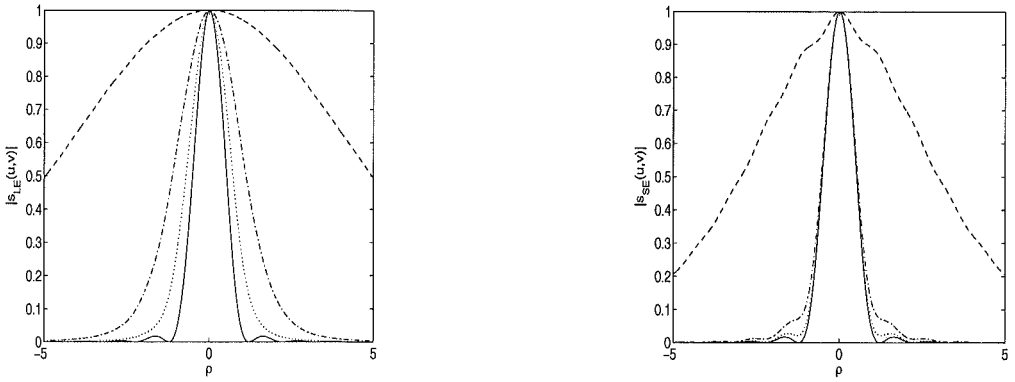

(a) (b)

Figure 3.16 For a circular aperture, the normalised (a) long exposure PSFs and (b) short exposure PSFs for D/r_0 ratios of 0 (solid), 1 (dotted), 2 (dashed-dotted) and 10 (dashed).

The difference between long and short exposure imaging is given by the $1-(\lambda f|\mathbf{x}|/D)^{1/3}$ term in the exponential of the short exposure atmospheric covariance. For a circular aperture, the short exposure OTF is given by substituting Eq. (3.79) and Eq. (3.46) into Eq. (3.76)

$$\begin{aligned}\mathcal{H}_{SE}(r) &= \frac{2}{\pi}\left[\cos^{-1}\left(\frac{\lambda f r}{D}\right)-\frac{\lambda f r}{D}\sqrt{1-\left(\frac{\lambda f r}{D}\right)^2}\right] \\ &\times \exp\left[-3.44\left(\frac{\lambda f|r|}{r_0}\right)^{5/3}\left(1-\left(\frac{\lambda f|r|}{D}\right)^{1/3}\right)\right]. \end{aligned} \tag{3.80}$$

The short exposure OTF for the circular aperture is plotted in Fig. 3.15(b) for several D/r_0 ratios. Again the short exposure PSF is computed numerically for a circular aperture and is shown in Fig. 3.16(b) for the same levels of turbulence.

The advantage in using short exposure images rather than long exposure images can be

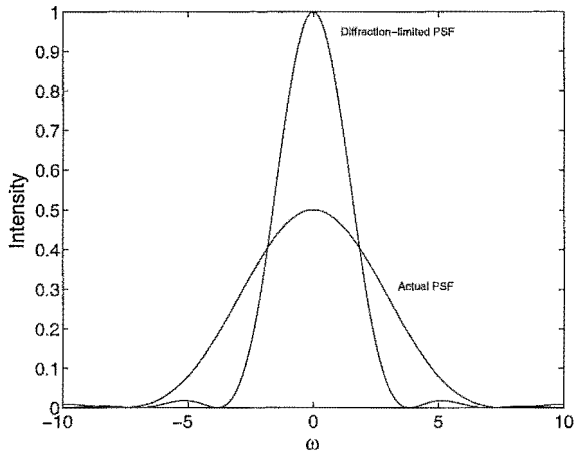

Figure 3.17 The Strehl ratio is defined as the ratio of the peak of the diffraction-limited PSF to the peak of the unaberrated PSF.

seen in comparing either the respective OTFs of Fig. 3.15 or the PSFs in 3.16. The magnitude of the OTFs for long exposure imaging drop off more quickly than their short exposure counterparts. This indicates more high frequency content is lost with long exposure imaging than short. The PSFs for short exposure imaging are narrower than those of long exposure imaging and therefore closer to the ideal diffraction-limited case.

3.3.2 Strehl ratio

A useful measure of the performance of an optical system is the Strehl ratio, S, which is the ratio of the peak values of the aberrated and unaberrated PSFs. An example of aberrated and unaberrated PSFs for a circular aperture are shown in Fig. 3.17. Mathematically, the Strehl ratio is defined by

$$S = \frac{(|h(u,v)|^2_{\max})_{\text{aberrated}}}{(|h(u,v)|^2_{\max})_{\text{diffraction-limited}}}. \tag{3.81}$$

The Strehl ratio is bounded between 0 and 1, with 1 representing an aberration free system. It should be noted that if the aberration is a tip or tilt, then this results in a shift of the centre of the image and does not affect the Strehl ratio. A system with a Strehl ratio of 0.8 or more is effectively diffraction-limited, and this limit is known as Marechal's criterion. For small aberrations, the Strehl ratio is related to the variance of the phase aberration, σ^2_ϕ, by

$$S \approx 1 - \sigma^2_\phi \qquad \sigma^2_\phi << 1. \tag{3.82}$$

If the aberration is not small, then the Strehl ratio depends on the exact nature of the aberration. If the aberration is assumed to be Gaussian and the telescope diameter D is much

greater than r_0, then the Strehl ratio can be approximated by

$$S \approx \exp[-\sigma_\phi^2]. \tag{3.83}$$

The Strehl ratio as a measure of image quality does have its drawbacks; for instance, the Strehl ratio cannot differentiate between a broad and a narrow PSF if they have the same peak value. Instead, other performance measures can be used by astronomers for optical systems, such as the full width at half maximum (FWHM) of the PSF of a point source.

The Strehl ratio is one of a number of possible sharpness metrics, S_Γ, that can be used in astronomical imaging. The sharpness S_Γ of an image is defined as a quantity which reaches its maximum value only for a true (undistorted) image [39]. The sharpness metric is computed as a weighted sum, $w(u,v)$, of a non-linear point transformation on the image intensity, $\Gamma I(u,v)]$, over all the image pixels, [40]

$$S_\Gamma = \sum_{u,v} w(u,v)\Gamma[I(u,v)]. \tag{3.84}$$

For example, for Muller and Buffington's fifth sharpness metric, the non-linear point transformation is the image raised to a power [39]

$$\Gamma[I(u,v)] = [I(u,v)]^\beta. \tag{3.85}$$

The image-sharpening approach is to iteratively choose the wavefront aberration, $\phi(x,y)$, to maximise the sharpness of the image. In Chapter 5, the sharpness metric of the Strehl is maximised to determine the fixed abberations of the telescope. The Strehl ratio is chosen as the sharpness metric in this thesis because it is easily computed.

3.3.3 Partially compensated objects

A further example of the drawbacks of the Strehl ratio is a point source when partially compensated with adaptive optics. When an object is partially compensated, the PSF is the sum of two terms, the Airy disk and a halo due to light diffracted by the remaining small scale wavefront phase errors [38]. The PSF of a partially compensated object is shown in Fig. 3.18. The core of the partially compensated object has the same approximate width, $\approx \lambda/D$, as the diffraction-limited PSF, shown in Figure 3.17. However, there exists a halo around the compensated object with a FWHM of λ/r_0 [27]. The halo masks the extent of the star image and consequently the resolution is reduced. Also, the halo can mask a lower magnitude companion star. The better the adaptive optics system is at compensating for the atmosphere, the more energy there is in the core and less in the halo. A better measure of the quality of the compensation than the Strehl is therefore the relative fractions of light

in the core and halo [38].

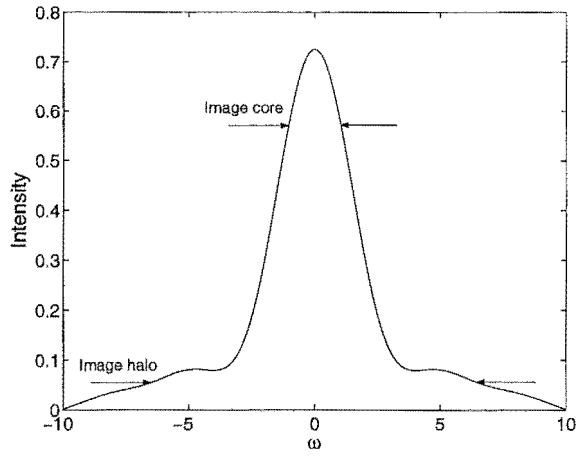

Figure 3.18 The PSF of an object partially compensated object using adaptive optics with a broad halo and narrow core.

3.4 Photon detection

While light has been treated as a wave when propagating in this thesis, it is now assumed to be in photon form for the detection process. The quantized, random nature of photon arrival introduces noise in the detection process. The semi-classical model for photoelectric light detection is adopted in this thesis and allows the modelling of the detection process as a Poisson random variable [20]. The probability of receiving $n(u,v)$ photons at a point (u,v) in the detector plane is given by

$$Pr\{n(u,v)\} = \frac{i(u,v)^{n(u,v)} \exp[-i(u,v)]}{n(u,v)!} \tag{3.86}$$

where $i(u,v)$ is the mean intensity at the detector and ! is the factorial operator. In this thesis the Gaussian approximation to the Poisson is used when the mean number of photons is greater than 100. In this case the photon noise is therefore modelled as a Gaussian distribution with the mean and variance at each point dependent on the intensity of the signal at that point. A normalised speckle image formed at a detector without any additive photon noise is shown in Fig. 3.19(a). The same speckle image with 100 and 1000 photons added are shown in Fig. 3.19(b) and (c) respectively. The occurrence of photons far away from the central core of the speckle image in Fig. 3.19(b) and (c) should be noted. These photons are important since they have a significant effect in centroid calculation [41].

As well as photon noise, there exist other forms of detector noise. Charge-coupled devices (CCDs) are commonly used as the detectors in astronomical imaging. CCDs are corrupted with additive noise commonly referred to as read noise [20]. This source of noise is again

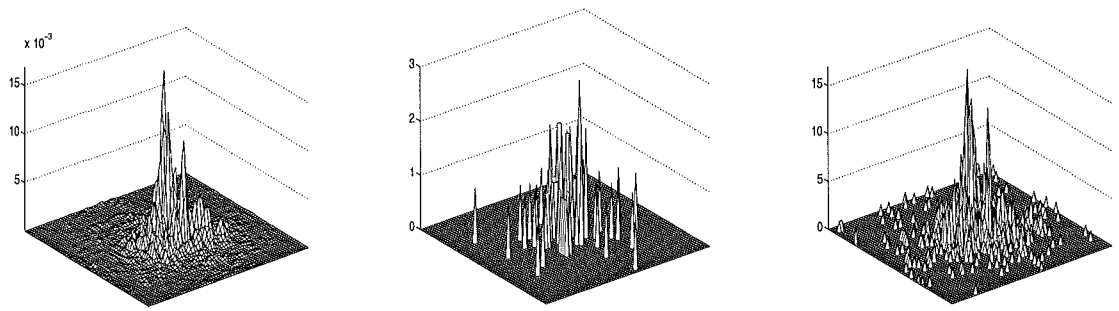

(a) (b) (c)

Figure 3.19 Speckle images for a D/r_0=8 phase screen (a) without photon noise, (b) with 100 photons, and (c) with 1000 photons.

modelled as a Poisson process at low noise levels and, unlike photon noise, is independent of the image intensity.

Chapter 4

Wavefront Estimation and Compensation

In Chapter 3, the cause of atmospheric turbulence and its effects on the images of astronomical objects are discussed. This chapter addresses the methods for overcoming the aberrations caused by the atmosphere. These aberrations can be compensated in real-time in a closed loop adaptive optic system or in an open loop post-processing algorithm. The fundamental building blocks of all adaptive optics systems and the most common computer post-processing schemes are reviewed in this chapter.

In order to compensate for the turbulence-induced phase distortion, it is first necessary to estimate the distortion. In an adaptive optics system, light is split between the imaging channel and a wavefront sensing channel, with the wavefront sensor used to measure the wavefront aberration. It is not possible to measure the phase aberration directly, and instead wavefront sensors manipulate the wavefront so as to produce intensity images from which the wavefront slope or curvature can be estimated. The three most commonly used wavefront sensors in astronomical adaptive optics today: the Shack-Hartmann, pyramid and curvature sensors, are reviewed in Section 4.1. The optimal method for estimating the wavefront from these wavefront sensing measurements is then examined in Section 4.2.

In an adaptive optics system, the aberrated wavefront is corrected by a deformable mirror. The wavefront estimate generated by the wavefront sensor is converted into a control matrix which is passed to the deformable mirror. The control matrix deforms the deformable mirror in such a way as to counteract the current estimate of the wavefront. The types and operation of the main classes of deformable mirrors used in adaptive optics systems are reviewed in Section 4.3.

Most astronomical objects of interest are too faint to provide enough light to run the wavefront sensor with a sufficiently high signal-to-noise ratio (SNR) to accurately estimate the wavefront. This has lead scientists to investigate methods for creating artificial stars in the upper atmosphere with the use of lasers. These laser guide stars are discussed in Section 4.4. The intrinsic problems that laser guide stars pose for the wavefront sensor are also discussed.

It is also possible to improve the aberrated astronomical image or a partially compensated image from an adaptive optics system using an algorithm on a computer after the image has been obtained. These algorithms are collectively referred to as computer post-processing. Three of these such algorithms: phase retrieval, phase diversity and deconvolution from wavefront sensing, are reviewed in Section 4.5.

4.1 Wavefront sensing

The role of the wavefront sensor in an adaptive optics system is to estimate the aberrated phase at the telescope aperture, $\phi(x, y)$. The main problem is that phase distortions at optical frequencies cannot be measured directly, and their effects on intensity are non-linearly related to the wavefront distortion. Wavefront sensors manipulate the wavefront by introducing a known wavefront perturbation which cause the intensity fluctuations to be linearly related to the wavefront. The resulting linear equations can then be solved to estimate the wavefront. In order to accurately estimate the wavefront, a number of properties are desirable in a wavefront sensor [22]. These are:

- Linearity: A linear relationship should exist between the wavefront and the wavefront sensing data. This ensures a unique easily obtainable solution.
- Broadband: The wavefront sensor should be able to operate across a wide range of wavelengths. For most astronomical objects light is limited, so it is important to use every available photon to maximise the SNR.
- Sensitivity: The wavefront sensing measurements need to be sensitive to changes in the wavefront.

Wavefront sensors can be roughly grouped into two classes. Interferometers can estimate the wavefront aberration from the interference pattern formed between the wavefront and a shifted version of the wavefront. Specific interferometers for wavefront estimation include the shearing, Mach-Zehnder and Twyman-Green interferometers [27]. The other major class of wavefront sensors are based on the principles of geometric optics, which are discussed in Section 3.1.1, that is the wavefront travels in straight lines perpendicular

to each point in the wavefront, and the displacement of the light is linearly related to the wavefront slope.

Geometric wavefront sensors are generally preferred to interferometers for astronomical adaptive optics [42]. Firstly, interferometers are, in general, not able to operate in incoherent light. Even light from laser guide stars is not coherent enough for typical interferometers. Secondly, the interference fringes are chromatic and the necessary filtering of the stellar light wastes valuable photons. Lastly, wavefront aberrations typically exceed 2π radians and interferometers have an inherent 2π phase ambiguity. Algorithms exist to un-wrap the phase but these are too slow to operate in a closed loop adaptive optics system.

This section discusses the three most commonly used geometric wavefront sensors in adaptive optics: the Shack-Hartmann, pyramid and curvature sensors. In addition, direct wavefront sensing, which is a variation on the processing of curvature sensing data, is investigated. In all these geometric wavefront sensors, there exists a trade-off between the spatial resolution of the wavefront estimate in the aperture plane and the accuracy with which the slope or curvature can be estimated in the measurement plane.

There is also the problem of how to estimate the wavefront, $\phi(x, y)$, from the measurements from the wavefront sensor, m. The wavefront can be represented as a sum of basis functions, $\Psi_i(x, y)$

$$\phi(x, y) = \sum_{i=1}^{\infty} a_i \Psi_i(x, y), \tag{4.1}$$

where a are the coefficients of the basis functions. In this thesis, the estimate of the wavefront is made in terms of the Zernike basis polynomials but the following argument holds for all basis functions.

The measurements from the wavefront sensor, m, are linearly related to the true coefficients of the wavefront by

$$m = \Theta a + n, \tag{4.2}$$

where n is additive noise on the measurements and Θ is the interaction matrix [43].

The objective is to minimise the expected error, E, between the true coefficients of the wavefront, a, and the estimated coefficients, $\hat{a}$,

$$E = \left\langle \sum (a - \hat{a})^2 \right\rangle, \tag{4.3}$$

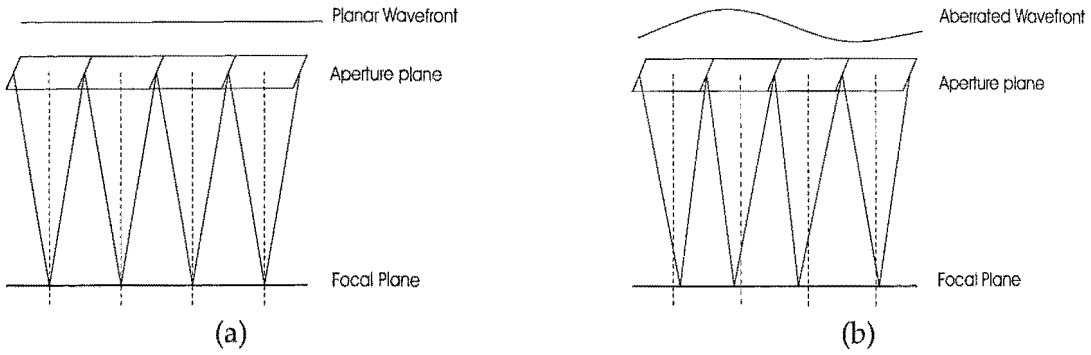

Figure 4.1 The Shack-Hartmann sensor with (a) a planar wavefront and (b) an aberrated wavefront. The dashed lines are the perpendicular bisectors of the lenslets. [22]

where $\langle \cdot \rangle$ denotes the ensemble average. The linear system of equations relating the measurements from the wavefront sensor to the coefficients of the wavefront is underdetermined since the wavefront has an infinite number of degrees of freedom and there are a finite number of measurements. The key point with wavefront estimation is that the underdetermined system of linear equations is rendered soluble by an assumption of the prior probabilities of the unknown coefficients.

4.1.1 Shack-Hartmann wavefront sensor

The most commonly used wavefront sensor in astronomical adaptive optics is the Shack-Hartmann wavefront sensor, which is shown in Fig. 4.1. The Shack-Hartmann wavefront sensor consists of an array of lenslets placed in the aperture plane of the telescope. The lenslet array subdivides the complex field in the aperture, with each lenslet forming a low resolution image of the object.

When there is no aberration present, the low resolution images are focused onto points directly below the centre of the respective lenslet as in Fig 4.1(a). However, if there is an overall mean wavefront slope over the lenslet, then that image is displaced from the centre by an amount proportional to the mean wavefront slope [37], Fig 4.1(b). The wavefront slope in the aperture plane in the x and y directions over each lenslet can be formed by calculating the displacement of the image in the x and y directions from the unaberrated rest positions. The entire wavefront can then be reconstructed from the mean slope measurements across the aperture.

The size of the lenslet determines the spatial resolution of the Shack-Hartmann sensor. When the resolution is low, only a small number of modes in the atmospheric turbulence can be determined by the sensor. The smaller the lenslet, the smaller a region of the wavefront the slope can be estimated for. The aberrations of a higher order than tilt within each lenslet cannot be detected. However, reducing the size of the lenslets in the array reduces

the number of photons per lenslet. This results in a reduction in the accuracy with which the slope estimates can be made. Also if the lenslet size is made smaller than the Fried parameter, r_0, then diffraction effects mean the spot size increases and consequently the accuracy of the slope estimate decreases. In practice, the optimum for the Shack-Hartmann sensor is when the lenslet size is close to r_0.

The displacement is conventionally estimated with the centroid estimator, which computes the centre of mass of the image. If the detector consists of an array of finite sized pixels of width Δ, with $(2P, 2Q)$ pixels per image, the centroid estimator in the x and y directions, (m_x, m_y), is

$$m_x = \left[\sum_{p=-P+1}^{P}\sum_{q=-Q+1}^{Q} I(p\Delta, q\Delta)(p\Delta - \delta_u)\right] \Big/ \left[\sum_{p=-P+1}^{P}\sum_{q=-Q+1}^{Q} I(p\Delta, q\Delta))\right] \tag{4.4}$$

$$m_y = \left[\sum_{p=-P+1}^{P}\sum_{q=-Q+1}^{Q} I(p\Delta, q\Delta)(q\Delta - \delta_v)\right] \Big/ \left[\sum_{p=-P+1}^{P}\sum_{q=-Q+1}^{Q} I(p\Delta, q\Delta)\right], \tag{4.5}$$

where (δ_u, δ_v) is the offset from the first pixel to the origin in the focal plane.

The variance of the centroid estimate strongly depends on the type of noise that predominates in the CCD. If it is read noise, then each pixel can be modelled as having a noise variance equal to η^2. The overall noise variance is equal to

$$\sigma^2 = E\left[(\hat{a} - a)^2\right] = \eta^2 \sum_i \sum_j (i\Delta - \delta_u)^2. \tag{4.6}$$

This variance grows without bound with the size of the CCD, and dictates that the smallest practical number of pixels should be used. A 2×2 array (or quad-cell) with $\delta = \frac{1}{2}$ is thus the configuration that dominates many existing slope sensors [44].

Improvements in technology may mean that read noise is no longer the dominant noise source, and Poisson photon noise is in fact the limiting factor. In this case the variance of the centroid noise is equal to

$$\sigma^2 = E\left[(\hat{a} - a)^2\right] = \frac{1}{R} \sum_p \sum_q (p\Delta - \delta)^2 I(p\Delta, q\Delta), \tag{4.7}$$

where R is the total number of photons. For a finite aperture the variance of the centroid operator tends to infinity. Physically, the reason for this is that the probability of detecting photons very far away from the centre of the image intensity (the Airy disk for a circular aperture) does not decay quickly enough [41].

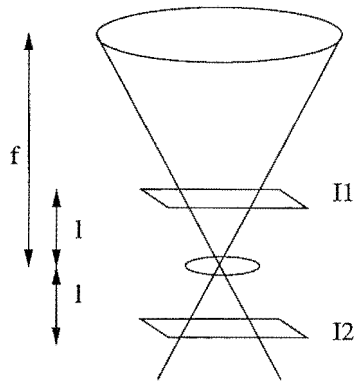

Figure 4.2 The curvature sensor layout [22].

Truncating the plane constrains the centroid estimate to a certain region, making the variance finite. Since the truncated plane is placed where the centre is expected to be, prior information is implicitly added [45]. By adding prior information, truncating the plane can improve the centroid estimate, even though some photons are lost.

4.1.2 Curvature wavefront sensor

Curvature wavefront sensors were first proposed by Roddier in 1988 [46]. The curvature sensor estimates the wavefront from measurements of the curvature within the aperture and the radial tilt at the edges of the aperture. The layout of the curvature sensor is shown in Fig. 4.2. The telescope aperture has a focal length f. Two defocused images of the aperture, $I_1(\mathbf{x})$ and $I_2(\mathbf{x})$, are captured at a distance l either side of the focal plane. A second lens of focal length $f/2$ is placed at the focal plane in order that the two images are of the same scale.

Assuming geometric optics, the wavefront curvature, $\nabla^2 W(x,y)$, is related to the two intensity measurements by [46,47]

$$\frac{I_1(x,y) - I_2(-(x,y))}{I_1(x,y) + I_2(-(x,y))} = \frac{f(f-l)}{2l}\left[\frac{\partial W(f(x,y)/l)}{\partial n}U(x,y) - P\nabla^2 W(f(x,y)/l)\right], \qquad (4.8)$$

where P is the transmission function of the aperture, $U(x,y)$ is the Heaviside unit step around the aperture edge, and is weighted by the radial tilt, $\partial W/\partial n$.

For practical wavefront sensors, only one detector is used instead of the two illustrated in Fig. 4.2. Instead, a variable curvature mirror is placed at the focal plane of the telescope [48]. The two defocused images of the aperture, $I_1(\mathbf{x})$ and $I_2(\mathbf{x})$, are then formed at the same detector from the concave and convex formations of the variable curvature mirror.

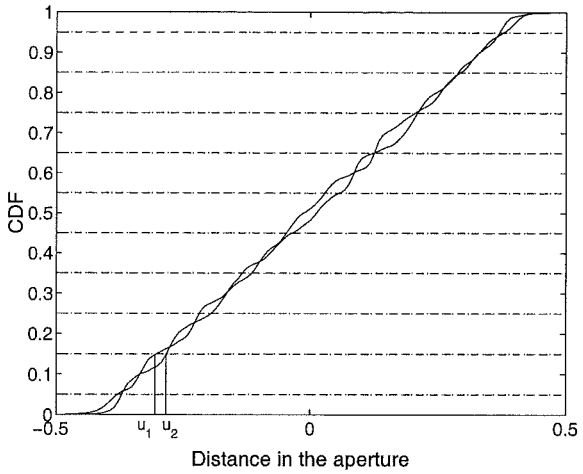

Figure 4.3 The normalized CDFs, $C_1(x)$ and $C_2(x)$ and the sampling intervals, $s = [0.05, 0.15, 0.25, \ldots, 0.95]$. The points where each of the curves intersects $s(2) = 0.15$ are marked u_1 and u_2 respectively [25].

An advantage of the curvature sensor is that Poisson's equation can be solved directly by applying the Laplacian measurements to a bimorph mirror, which is discussed in Section 4.3.3.

4.1.3 Direct wavefront sensing

Direct wavefront sensing was proposed by van Dam and Lane [25] in 2002 to determine the wavefront aberration from two defocused images. The two defocused images are generated in the same manner as for the curvature sensor. The key idea with direct wavefront sensing is that the intensity of the propagated wavefront represents a PDF for photon arrival. The change in the PDF between the two detector planes can be seen indirectly through the CDFs of the intensities at the two planes. Van Dam and Lane showed using the WTE and the ITE, which are discussed in Section 3.1.1, that there exists a linear relationship between the slope at a point in the wavefront and the difference in the abscissae of the CDFs of the two intensity patterns for a chosen CDF value.

In one dimension, direct wavefront sensing is essentially a problem of histogram equalisation. Two example CDFs and the constant CDF lines representing the sampling interval, s, are shown in Fig. 4.3. The wavefront slope estimate, W_x, over a set of approximately regular intervals in the x dimension is made using the relationship

$$W_x\left(\frac{u_1(i) + u_2(i)}{2}\right) = \frac{u_1(i) - u_2(i)}{2z}, \tag{4.9}$$

where u_1 and u_2 are the abscissae of the CDFs at the two detector planes, z is the propagation distance and i is the index of the set of sample points.

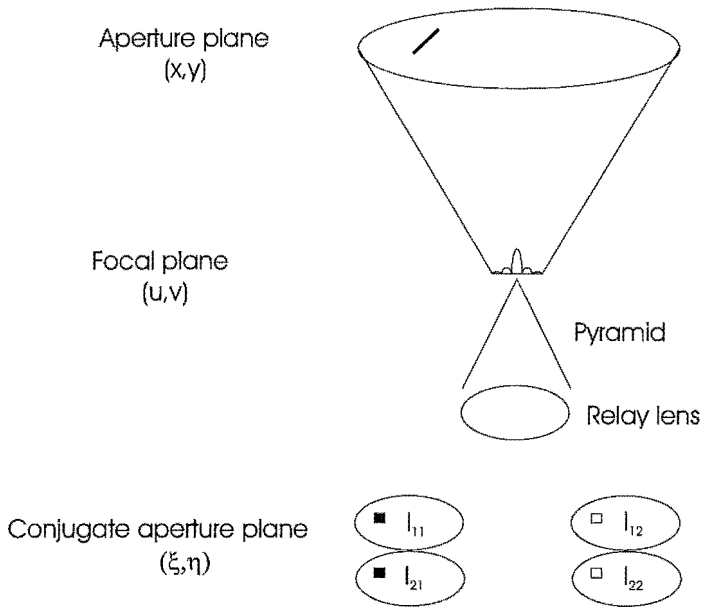

Figure 4.4 The pyramid sensor layout. A positive slope at a point in the aperture illuminates the corresponding points in the left hand images and not those on the right.

Of course, for practical wavefront sensing the wavefront slope needs to be estimated in two dimensions. The radon transform is thus employed to collapse the two dimensional problem to an equivalent system of one dimensional problems [25].

4.1.4 Pyramid wavefront sensor

The pyramid wavefront sensor was introduced by Ragazzoni in 1996 [11], although Babock, in his seminal paper on adaptive optics [3], also suggests using a beam-splitting pyramid to determine the wavefront aberration. The pyramid sensor [11,49–52] is a development of the Foucault, or knife-edge test [53], and is best understood in terms of geometric optics. The pyramid subdivides the complex field in the focal plane into quadrants at the origin using a four sided glass prism (pyramid) positioned at the origin of the focal plane of the telescope. The subdivided fields are then passed through a relay lens to form four images of the aperture, I_{11}, I_{12}, I_{21} and I_{22}. The subscripts denote the row and column of the image respectively.

If the pyramid sensor is considered from a geometric optics perspective, the rays from the points in the aperture where the slope is positive pass to the right of the pyramid vertex and illuminate the corresponding points in the left hand images as shown in Fig. 4.4. Conversely, for the regions in the aperture where the slope is negative, the corresponding points in the right hand images are illuminated. If the predictions of the geometrical optics approximation are followed to their logical conclusion, a step discontinuity in the intensity versus slope curve is obtained as shown in Fig. 4.5(a) for a typical pixel in the left hand

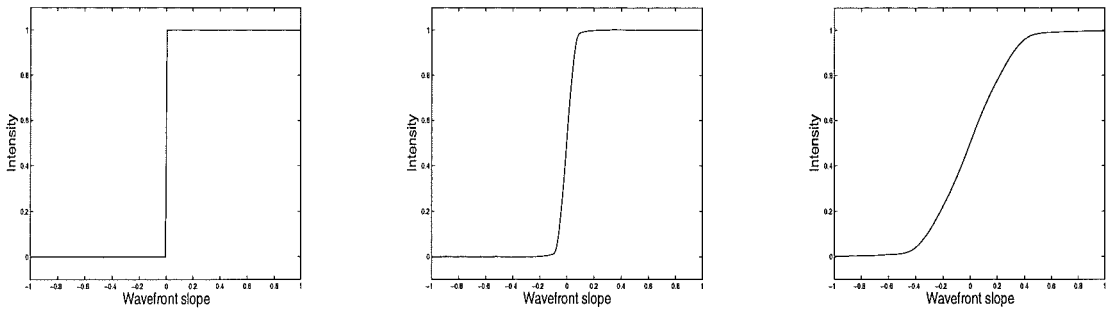

(a) (b) (c)

Figure 4.5 The intensity for a given pixel versus the slope across the corresponding point in the aperture assuming (a) zero spot size, (b) a finite spot size, and (c) a finite size spot with modulation of the pyramid.

images.

However, as shown in Section 3.1.2, Fourier optics predicts that at the focal plane the aperture will form a spot of finite size instead of the point predicted by geometric optics. The intensity versus slope curve is thus approximately linear over a range dependent on the size of the spot in the focal plane, Fig. 4.5(b).

A method to overcome the dependence of the transition region on the size of the spot is to introduce a mechanical modulation. This modulation moves the pyramid in the focal plane relative to the complex field incident on the pyramid. The modulation extends the range of slopes which are within the linear region at the price of reducing the slope within the linear region (Fig. 4.5(c)). Whilst this is beneficial from the point of view of ensuring that the output signal is a linear function of the wavefront slope, it is at the cost of sensitivity since it requires a larger change in the wavefront slope to produce an equivalent change in the pixel intensity.

Two different paths for the modulation of the pyramid were identified by Ragazzoni and these are shown in Fig. 4.6. The diamond path leads to a linear relationship between the wavefront slope and the images formed in the conjugate aperture plane. The circular path is mechanically easier to produce, but generates only an approximately linear signal.

Ragazzoni generated formulae for the orthogonal slope estimates from the four aperture images for the pyramid sensor using simple geometrical considerations, [11]

$$\frac{\partial\phi(\xi,\eta)}{\partial\xi} \propto \Big[I_{11}(\xi,\eta) - I_{12}(\xi,\eta) - I_{21}(\xi,\eta) + I_{22}(\xi,\eta)\Big] \Big/ \Big[\sum_{i=1}^{2}\sum_{j=1}^{2} I_{ij}(\xi,\eta)\Big] \tag{4.10}$$

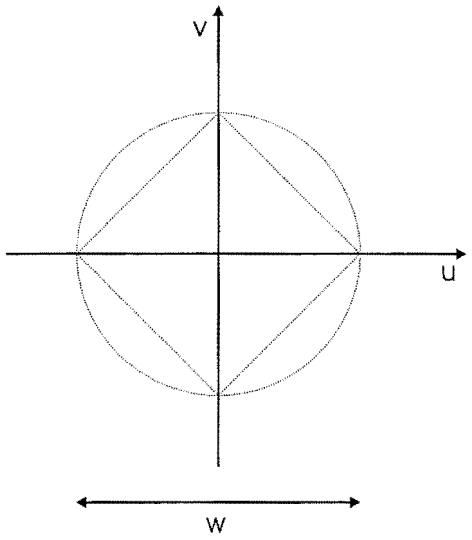

Figure 4.6 The circular and diamond modulation paths of width w for the pyramid sensor.

$$\frac{\partial\phi(\xi,\eta)}{\partial\eta} \propto \Big[I_{11}(\xi,\eta) + I_{12}(\xi,\eta) - I_{21}(\xi,\eta) - I_{22}(\xi,\eta)\Big] \Big/ \Big[\sum_{i=1}^{2}\sum_{j=1}^{2} I_{ij}(\xi,\eta)\Big]. \tag{4.11}$$

In the literature, the pyramid sensor has only be discussed within a geometric optics framework. By considering the pyramid sensor as equivalent to a lenslet array placed at the focal plane of the telescope, a Fourier optics analysis of the pyramid sensor can be made. This is done in Chapter 6. The Fourier analysis of the pyramid also enables a discussion of the spatial resolution limit of the pyramid sensor to be made.

The pyramid sensor operates by subdividing the focal plane into quadrants. However, the focal plane can be subdivided into any number of equal segments, and this is analysed in Chapter 7.

The pyramid sensor estimates the wavefront from the two sets of slope estimates generated from the four aperture images. However, it is possible to estimate the wavefront directly from the aperture images. This new method of estimating the wavefront from the aperture images, which is discussed in Chapter 7, avoids the discarding of information when generating the slope estimates. An iterative phase retrieval algorithm, which also estimates the wavefront directly from the aperture images, is investigated in Chapter 8.

4.2 Statistical wavefront estimation

Statistically speaking, wavefront estimation is choosing the most likely set of basis coefficients for the wavefront given the observed data from the wavefront sensor. Mathematically, this can be written as,

$$\overset{\max}{\hat{a}} \{Pr\{\hat{a}|m\}\}. \tag{4.12}$$

$Pr\{\hat{a}|m\}$ is difficult to express directly but is rendered more tractable by the use of Bayes' theorem,

$$Pr\{\hat{a}|m\} = \frac{Pr\{m|\hat{a}\}Pr\{\hat{a}\}}{Pr\{m\}}. \tag{4.13}$$

This approach is equivalent to the maximum *a posteriori* (MAP) approach originally proposed by Wallner [54]. The position of the maximum is unchanged by a monotonic transformation and hence further simplification can be achieved by taking the logarithm of Eq. (4.13)

$$\log[Pr\{\hat{a}|m\}] = \log[Pr\{m|\hat{a}\}] + \log[Pr\{\hat{a}\}] - \log[Pr\{m\}]. \tag{4.14}$$

It is worthwhile to consider each of these terms in turn. The term $\log[Pr\{m|\hat{a}\}]$ represents how likely it would be to observe the given measurements if the parameters were equal to $\hat{a}$. This can be computed using

$$\hat{m} = \Theta\hat{a} \tag{4.15}$$

to estimate the measurements that would have been expected from the current wavefront estimate. The difference, $\hat{m} - m$, is then an estimate of the noise, $\hat{n}$. Assuming the noise is a zero mean Gaussian random variable, $\log[Pr\{m|\hat{a}\}]$ can be estimated by

$$\begin{aligned} Pr\{m|\hat{a}\} &= \exp\left[-\frac{1}{2}\hat{n}^T N^{-1}\hat{n}\right] \\ &= \exp\left[-\frac{1}{2}(\hat{m}-m)^T N^{-1}(\hat{m}-m)\right] \end{aligned} \tag{4.16}$$

where $N = \langle nn^T \rangle$ is the expected noise covariance.

The $\log[Pr\{m\}]$ term of Eq. (4.14) can be discarded since it is not a function of $\hat{a}$, the variable that is being maximised. Put simply, however improbable the data, it remains what was measured.

The term $Pr\{\hat{a}\}$ is the key to solving an underdetermined system of equations. Given

two possible solutions which would produce exactly the same measurements, $Pr\{\hat{a}\}$ is used to select the most likely. In the case of a wavefront aberration caused by atmospheric turbulence the estimated coefficients, $\hat{a}$, are also zero mean Gaussian random variables, so their probability distribution is given by

$$Pr\{\hat{a}\} = \exp\left[-\frac{1}{2}\hat{a}^T C^{-1}\hat{a}\right]. \tag{4.17}$$

Here $C = \langle aa^T \rangle$ is the covariance of the basis functions used to model the turbulence. Covariance matrices are positive definite by definition which implies $\hat{a}^T C^{-1}\hat{a} > 0$, and thus a defined maximum of $Pr\{\hat{a}\}$ exists.

Using Eq.s (4.16) and (4.17) in Eq. (4.14) yields

$$\log[Pr\{\hat{a}|m\}] = -\frac{1}{2}\Big(\hat{a}^T C^{-1}\hat{a} + (\hat{m} - m)^T N^{-1}(\hat{m} - m)\Big). \tag{4.18}$$

Substituting Eq. (4.15) for $\hat{m}$ into Eq. (4.18) gives

$$\log[Pr\{\hat{a}|m\}] = -\frac{1}{2}\Big(\hat{a}^T C^{-1}\hat{a} + (\Theta\hat{a} - m)^T N^{-1}(\Theta\hat{a} - m)\Big). \tag{4.19}$$

Equating the partial derivative of Eq. (4.19) with respect to $\hat{a}^T$ to zero

$$\frac{\partial \log[Pr\{\hat{a}|m\}]}{\partial \hat{a}^T} = C^{-1}\hat{a} + \Theta^T N^{-1}\Theta\hat{a} - \Theta^T N^{-1} m = 0 \tag{4.20}$$

defines the reconstructor, Ω, which gives the most likely estimate,

$$\begin{aligned} \hat{a} &= (C^{-1} + \Theta^T N^{-1}\Theta)^{-1}\Theta^T N^{-1} m \\ &= \Omega m. \end{aligned} \tag{4.21}$$

The optimal estimator Ω is a function of both the covariance of the atmospheric turbulence and the measurement noise. A matrix identity can be used to derive an equivalent form of Eq. (4.21) [55]

$$\Omega = C\Theta^T(\Theta C\Theta^T + N)^{-1}. \tag{4.22}$$

The term inverted in Eq. (4.22) is the covariance of the measurements and is consequently directly measurable,

$$\langle mm^T \rangle = \Theta C\Theta^T + N. \tag{4.23}$$

If the relative merits of the two forms of the optimal reconstructor are considered, Eq.s (4.21) and (4.22), both require a matrix inversion. Computationally, the size of the matrix

inversion is important. Eq. (4.21) inverts a $P \times P$ (parameters) matrix and Eq. (4.22) an $M \times M$ (measurements) matrix. In a traditional least squares system there are fewer parameters estimated than there are measurements, ie $M > P$, indicating Eq. (4.22) should be used. In a Bayesian framework, more modes are being reconstructed than there are measurements, ie $P > M$, so Eq. (4.21) is more convenient.

In practice, an additional weighting term α, which determines the balance between the fit to the data (N) and the prior information (C), is often included in Eq. (4.21) such that

$$\Omega = (\alpha C^{-1} + \Theta^T N^{-1} \Theta)^{-1} \Theta^T N^{-1}. \tag{4.24}$$

If α is too high, then too much emphasis is put on the prior for the weights; on the other hand, too small a value for α also leads to a sub-optimal solution. However, it is important to note that the reconstruction should not be unduly sensitive to the relative weighting between the prior assumptions and the observed data.

If in the ideal case the noise on the measurements is zero, such that $N = 0$, then the measurements are explained exactly and the basis coefficients are assigned by their relative probability, which is determined by C.

If only a finite number of basis modes are estimated, then the coefficients of all the other modes are implicitly assumed to be zero and the covariance of the modes estimated is very large. Thus $\Theta^T N^{-1} \Theta$ becomes large relative to C^{-1} and in this case Eq. (4.21) simplifies to a weighted least-squares formula

$$\Omega = (\Theta^T N^{-1} \Theta)^{-1} \Theta^T N^{-1}. \tag{4.25}$$

Here the information on the relative probability of the basis coefficients contained in C is lost.

An advantage of this statistical approach to wavefront estimation is that the residual error can be predicted by substituting Eq. (4.21) into Eq. (4.3),

$$E = \left\langle (a - \Omega m)(a - \Omega m)^T \right\rangle. \tag{4.26}$$

By further substituting $\Theta a + n$ for m gives

$$E = \left\langle \Big((I - \Omega\Theta)a - \Omega n \Big) \Big((I - \Omega\Theta)a - \Omega n \Big)^T \right\rangle, \tag{4.27}$$

where I is the identity matrix. If Eq. (4.27) is expanded and the noise and the signal are

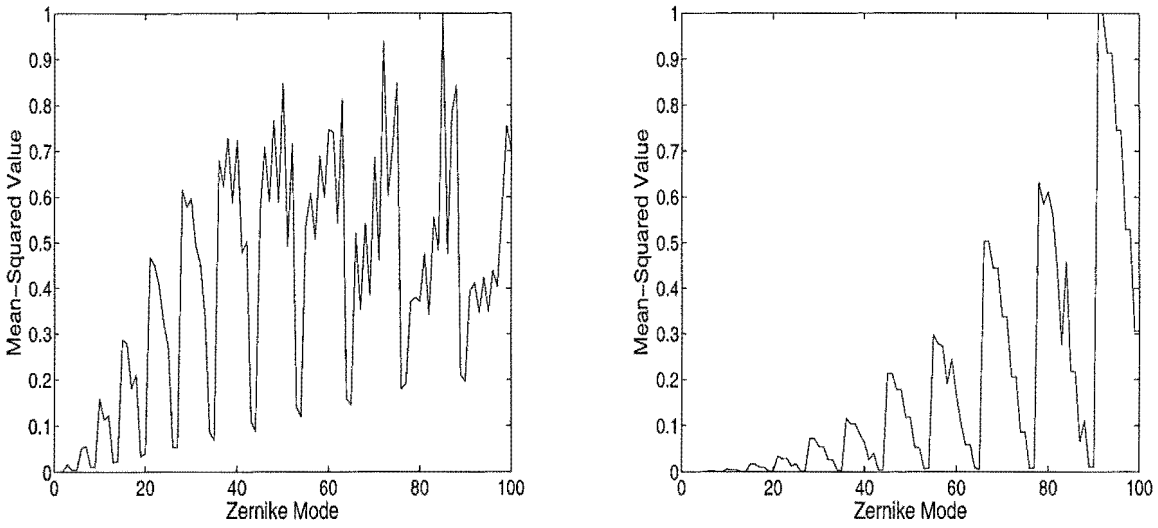

Figure 4.7 The normalised mean-squared values of the rows of $\Theta^T N^{-1}\Theta$ when N is the identity matrix for (a) the Shack-Hartmann sensor (real data), and (b) the pyramid sensor (simulated data).

assumed to be uncorrelated, then the residual error simplifies to,

$$E = \left\langle (I - \Omega\Theta)C(I - \Omega\Theta)^T + \Omega N \Omega^T \right\rangle. \tag{4.28}$$

A numerical value for the residual error can be obtained by taking the trace of each matrix in Eq. (4.28). Thus provided the statistics of the noise and turbulence are known, then the error in the reconstruction can be predicted.

Reconstructor structure

One of the problems with reconstructing an astronomical object using either pyramid or Shack-Hartmann wavefront sensing measurements and Zernike polynomials is that the reconstructor is unable to accurately estimate certain Zernike coefficients across the aperture. This problem can be demonstrated by examining the structure of the reconstructor in Eq. (4.24).

The $\Theta^T N^{-1}\Theta$ term in Eq. (4.24) reduces to $\Theta^T\Theta$ when the noise covariance is estimated by the identity matrix to model Gaussian noise. $\Theta^T\Theta$ is an $I \times I$ matrix, where I is the number of Zernike modes estimated. The mean-squared value of each of the I rows of this matrix, normalised to the maximum value, are plotted in Fig. 4.7 (a) and (b) for the first 100 Zernike modes for the Shack-Hartmann and pyramid sensors respectively. For both sensors, there are nulls in $\Theta^T\Theta$ at modes of low azimuthal order, m, occurring periodically with respect to the radial order, n, of the Zernike polynomials.

At the modes where these nulls occur the reconstructor needs to amplify the data to estimate the corresponding Zernike coefficient. This in turn leads to an amplification of the noise on the data and can lead to erroneous estimation of some modes across the aperture. At these nulls the $\Theta^T N^{-1}\Theta$ term is small relative to the αC^{-1} term. The error in the reconstruction from the amplification of the noise on the data for these specific Zernike modes can become greater than the error from not estimating these particular modes at all. The reconstructor therefore has to decide for each mode if it is better to simply not estimate that mode.

The effect of this phenomenon with the Shack-Hartmann sensor on the reconstruction of a single bright star using deconvolution from wavefront sensing is detailed in Section 5.5.

4.3 Deformable mirrors

Deformable mirrors can provide a real time compensation for the atmospheric turbulence by introducing an optical path difference, which induces an optical phase shift in the aberrated wavefront. The generic design of a deformable mirror consists of a number of voltage controlled actuators which can push and pull the mirror surface to deform it. The major design considerations for the choice of deformable mirror include the dynamic range (stroke) of the actuators, the temporal response of the mirror and the spatial density of the actuators. Although wavefront correctors are not the topic of this thesis, a summary of the major characteristics of the main classes is presented in the following subsections for completeness in the discussion of adaptive optics.

4.3.1 Segmented mirrors

Segmented mirrors consist of a number of elementary mirrors which are each individually controlled by one actuator for piston-only control or three actuators for piston and tip-tilt control. The main advantage of segmented mirrors is that they consist of an array of identical and easily repairable elementary elements. If an element breaks down, it does not affect the rest of the mirror and can easily be replaced [56]. A drawback of segmented mirrors is that an edge diffraction effect is induced by the gaps between the segments [57].

4.3.2 Continuous face-sheet mirrors

Continuous face-sheet mirrors consist of a continuous reflective glass face-sheet deformed by an array of discrete actuators. Continuous face-sheet mirrors have a significantly lower fitting error than segmented mirrors with the same number of actuators.

4.3.3 Bimorph mirrors

A bimorph mirror is constructed from two thin piezoelectric ceramic wafers which are oppositely polarised [57]. An array of electrodes is deposited between these two wafers. When a voltage, V, is applied to an electrode at a point (x, y), the piezoelectric wafer contracts locally and the other wafer expands. This induces a surface deformation of the mirror, $S(x, y)$, which follows Poisson's equation [27]

$$\nabla^2 S(x,y) = \frac{\partial^2 S(x,y)}{\partial x^2} + \frac{\partial^2 S(x,y)}{\partial y^2} \propto V(x,y). \tag{4.29}$$

Thus the bimorph mirror responds with a curvature proportional to the applied voltage. In theory, the bimorph mirror can be used in conjunction with the curvature sensor since the measurements can be applied straight to the mirror, avoiding the need to integrate the curvature sensor measurements [56].

4.3.4 MEMs mirrors

Micro-electro-mechanical (MEM) mirrors are fabricated using the manufacturing methods of the integrated circuit industry. The actuation in MEMs devices is created by electrostatic attraction and repulsion between control electrodes and a common electrode membrane, which also acts as the mirror surface. MEM mirrors have the potential for low production costs by making use of current integrated circuit technology [27].

4.4 Laser guide stars

In astronomy, many of the objects of most interest are also the faintest. These faint objects are not bright enough to adequately drive the wavefront sensor and hence perform adaptive optics on them. A method to overcome this problem is to use a nearby bright star, also known as a natural guide star (NGS), to provide enough light to allow the wavefront sensor to accurately estimate the wavefront. However, as mentioned in Section 3.2.2, the probability of an NGS existing within the isoplanatic angle of a given astronomical object is very low (1 % for observations in the infra-red and less in the visible [58]).

The United States military and Foy and Labeyrie [59] independently proposed to use a laser to create an artificial guide star at a chosen point in the atmosphere. The back-scattered light from the laser guide star (LGS) can then be used to estimate the atmospheric aberrations between the LGS and the telescope aperture.

Two different techniques for generating artificial guide stars have been demonstrated. Rayleigh beacons are generated from the scatter off air molecules in the stratosphere (at

approximately 20km). Sodium beacons are produced from resonance scattering of sodium atoms in the mesosphere (at 90km) with lasers of wavelength of 589.2 nm. Rayleigh beacons have the advantage that the exact wavelength of the laser does not matter, and so high power output can be easily achieved [58]. The main disadvantage of Rayleigh beacons is their low altitude, which means only a fraction of the atmospheric turbulence can be sampled. For this reason, sodium beacons with their higher altitude are preferred for adaptive optics.

Sodium beacons suffer from a number of inherent problems that affect the operation of the wavefront sensor and are discussed in the following subsections.

4.4.1 Tilt determination

The laser beam that creates the LGS in the mesosphere is equally deflected on its path to and from the mesosphere. The LGS position appears fixed with respect to the optical axis of the telescope irrespective of the true position of the LGS [60]. Thus the tilt introduced on the wavefront cannot be determined with an LGS.

The simplest solution to the tilt determination problem is to use a nearby NGS to measure the tip and tilt while using the LGS to measure the higher order terms. The tip and tilt from the NGS are generated using the whole aperture, and these two modes have a larger isoplanatic patch than the higher order modes [60]. However, since the NGS is uncompensated a high photon flux is required. Thus the probability of finding a sufficiently bright NGS in the tilt isoplanatic patch is again low.

If the higher order modes of the NGS are corrected using a second LGS and secondary adaptive optics system, then an NGS with a lower photon flux can be used to determine the wavefront tip and tilt. The disadvantages of this system are the increase in hardware required and that full sky coverage, especially in the visible, is not assured [60].

An alternative method proposed by Foy [60] is the polychromatic sodium star. This method is based on the principle of dispersion; the difference between the tilt at different wavelengths is proportional to the absolute tilt. The angle of the absolute tilt is given by

$$\theta = \frac{n-1}{n_1 - n_2}(\theta_1 - \theta_2), \tag{4.30}$$

where n_1 and n_2 are the refractive indices of air at the two wavelengths, θ_1 and θ_2 are the tilts of the two wavelengths, and θ and n correspond to the tilt and refractive index at the wavelength of interest. The advantage of this method is that no NGS is required. Physically, the two different wavelengths of photons are emitted from sodium atoms depending on which one of two paths valence electrons take from the $4P_{3/2}$ level to the $3S_{1/2}$ level.

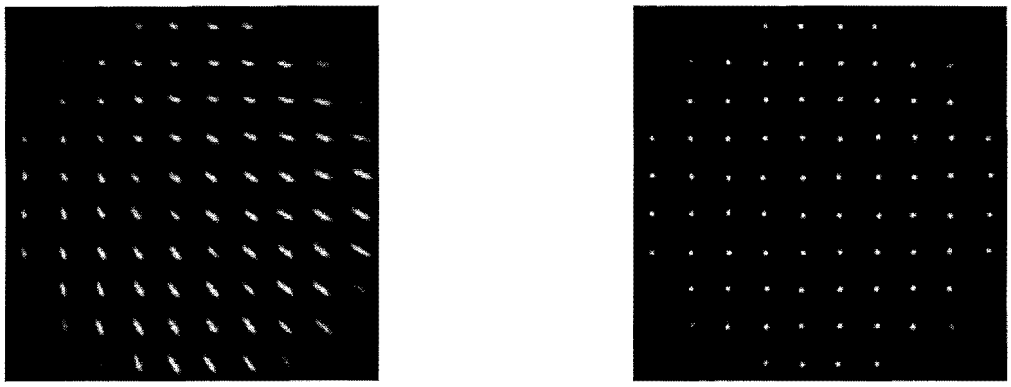

(a) (b)

Figure 4.8 Simulated spots formed with a 10×10 Shack-Hartmann array when observing a sodium laser beacon with an off axis projection of the laser. The laser is located at the top left hand corner of the aperture. (b) The spots formed when viewing a natural guide star through the same turbulence.

However, there are significantly fewer higher energy photons than lower energy ones and this affects the accuracy of the tilt measurement [60].

4.4.2 Off axis projection

Another inherent problem with laser guide stars is that since the sodium layer is approximately 10km thick, the LGS becomes extended for subapertures not on the optical axis of the telescope [63]. This causes the spot shape in the various subapertures of the Shack-Hartmann sensor to be different in different subapertures [61]. The apparent size of a laser spot is given by [62]

$$\theta_{\text{spot}} = \frac{\Delta H s}{H^2}, \tag{4.31}$$

where ΔH is the width of the sodium layer, H is the height of the sodium layer, and s is the separation between the projector and the considered subaperture. The elliptical nature of the Shack-Hartmann spots when viewing a sodium LGS can be seen in Fig. 4.8(a). This problem occurs regardless of whether the laser is projected from a separate aperture located on the side of the main telescope or from behind the secondary mirror of the telescope, although it is less severe in the latter case. Several methods to overcome this spot elongation have been proposed, including using a pulsed laser and time gating the received photons to remove those back-scattered from the upper end of the sodium layer. However, this comes at a cost in brightness of the LGS [63].

4.4.3 Focus anisoplanatism

Light from the astronomical object of interest passes through a cylinder, as shown in Fig. 4.9, whereas light from the LGS passes through a cone. The atmospheric turbulence present

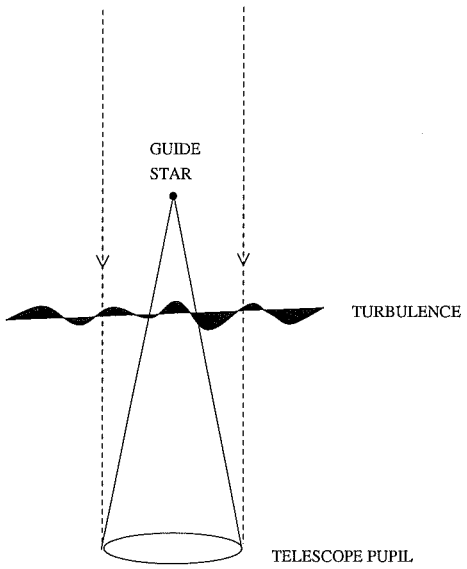

Figure 4.9 Focus anisoplanatism, also known as the cone effect. [8]

in the difference of these two volumes is not sampled by the LGS and hence introduces an error in the estimation of the wavefront by the wavefront sensor. This error is known as focus anisoplanatism or, alternatively, as the cone effect. The phase error, σ_ϕ^2, due to the cone effect of an LGS at height H and zenith angle γ, is given by [65]

$$\sigma_\phi^2 = \frac{2\pi^2}{\lambda^2} \frac{1}{H\cos(\gamma)} \int_0^H C_n^2(z) z^2 (z^{1/3} - 1) \mathrm{d}z. \tag{4.32}$$

The phase error can also be expressed by [64]

$$\sigma_\phi^2 = \left(\frac{D}{d_0}\right)^{5/3}, \tag{4.33}$$

where d_0 is a parameter that is dependent on the turbulence profile, wavelength, back-scatter altitude and zenith angle. From Eq. (4.33), it can be seen that the error from the cone effect is greater for larger telescopes. The proposed solution to alleviate the problem of the cone effect is to use many guide stars to reconstruct the three-dimensional turbulence profile, and this is discussed in the next subsection.

4.4.4 Multi-conjugate adaptive optics

The use of multiple guide stars was proposed to overcome the cone effect [66] or to reconstruct astronomical objects such as planets and galaxies, which are larger than the isoplanatic patch [67]. N layers of atmospheric turbulence, $\phi_n(x, y)$, can be compensated with the use of N deformable mirrors, DM_n, each conjugated to a different layer of turbulence.

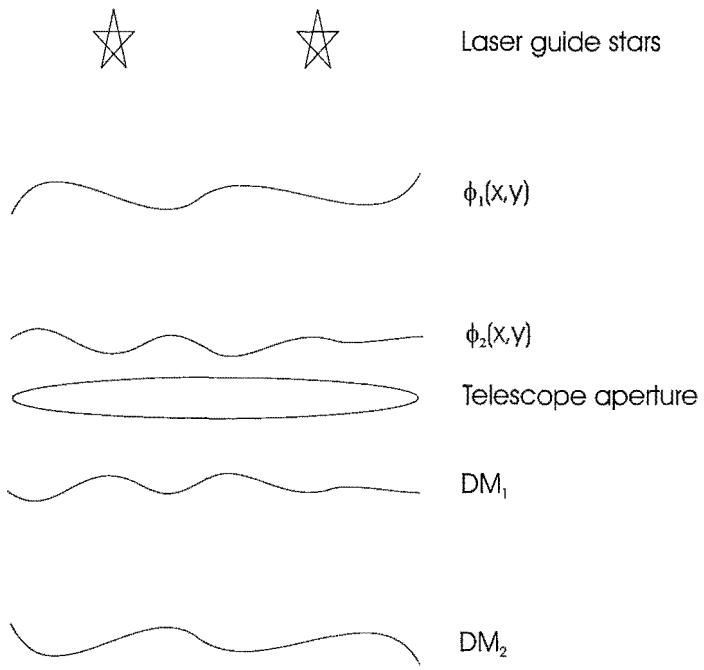

Figure 4.10 A multi-conjugate adaptive optic system with two guide stars and two deformable mirrors.

The use of multiple LGS and multiple deformable mirrors conjugated to the different layers of the atmospheric turbulence is known as multi-conjugate adaptive optics (MCAO). In addition, I wavefront sensors can be used to estimate the turbulence layers.

MCAO with two guide stars, two layers of turbulence and two deformable mirrors is shown in Fig. 4.10. The turbulence at the high altitude is compensated by DM_1 and that at the ground layer by DM_2.

The methods for combining the wavefront sensing measurements to form the three dimensional turbulence profile can be classified into two schools of thought: star-oriented and layer-oriented. In the star-oriented techniques, each wavefront sensor is coupled to a different guide star. Whereas in layer-oriented techniques, the wavefront sensors are coupled to different layers in the atmosphere and each of them collect light from the whole set of guide stars [68]. In both these techniques the estimation problem is to choose the most likely set of basis coefficients for the N turbulence layers, a_n, given the I sets of measurement data, m_i,

$$\max_{\hat{a}_n} \{Pr\{\hat{a}_n|m_i\}\}. \tag{4.34}$$

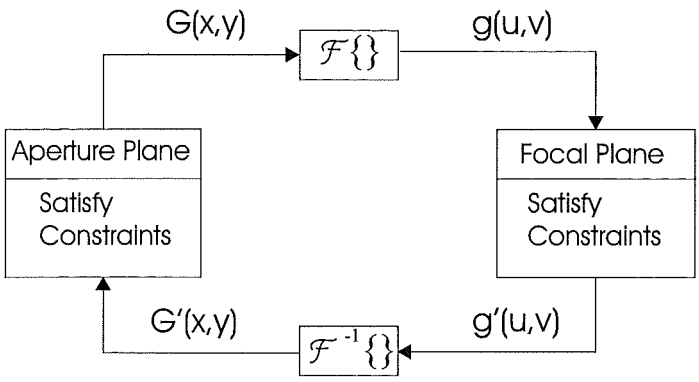

Figure 4.11 Block diagram of the Error-Reduction (Gerchberg-Saxton) phase retrieval algorithm.

4.5 Computer post-processing

The alternative to the real-time wavefront correction of adaptive optics is the set of methods that are used to deblur astronomical images after collection, commonly referred to as computer post-processing. This section reviews a number of these methods that are pertinent to this thesis including phase retrieval, phase diversity, and deconvolution from wavefront sensing.

4.5.1 Phase retrieval

As discussed in Section 4.1, wavefront sensing is a set of methods that introduce a known perturbation to generate a set of measurements which are linearly related to the wavefront phase. Conversely, phase retrieval is a non-linear iterative process used to determine the phase at the aperture plane of the telescope from the intensity measurements and prior information about the object and noise [69, 70]. The Fraunhofer diffraction formula, Eq. (3.24), is reproduced here

$$a(u,v) = \frac{\exp[jkz]}{j\lambda z} \exp\left[\frac{jk}{2z}(u^2+v^2)\right] \int_{-\infty}^{\infty}\int_{-\infty}^{\infty} A(\lambda z x, \lambda z y) \exp[-j2\pi(xu+yv)]\mathrm{d}x\mathrm{d}y, \tag{4.35}$$

where, as before, $A(x,y) = P(x,y)\exp[j\phi(x,y)]$ is the generalised aperture function. Eq. (4.35) shows the Fourier transform relationship between the complex field at the aperture, $A(\lambda z x, \lambda z y)$, and focal, $a(u,v)$, planes. The phase retrieval problem is the recovery of $\phi(x,y)$ from the observed intensity $|a(u,v)|^2$. A number of iterative phase retrieval algorithms have been proposed to recover the phase from the observed intensity [69, 71, 72].

One of the early phase retrieval iterative algorithms is the Gerchberg-Saxton (GS) [71] rou-

tine shown in Fig. 4.11. Each iteration of the GS algorithm consists of four steps:

(1) The current estimate of the object, $G_k(x,y)$, is Fourier transformed to form $g_k(u,v)$.

(2) The magnitude of $g_k(u,v)$ is made to conform with the measured modulus, $|a(u,v)|$, to form $g'_k(u,v)$.

(3) $g'_k(u,v)$ is inverse Fourier transformed to form $G'_k(x,y)$.

(4) $G'_k(x,y)$ is made to conform with the known object modulus, forming the new estimate of the object, $G_{k+1}(x,y)$.

In practice, instead of the magnitude in one of the Fourier domains, it is often only possible to estimate the size of an object. This constraint, along with the knowledge that the object is positive, was used by Fienup as the basis of the error-reduction (ER) algorithm [69], which is also described by Fig. 4.11. The first three steps of the ER algorithm are identical to those of the GS algorithm. However, the fourth step of the ER algorithm is: (4) the new estimate of the object, $G_{k+1}(x,y)$, is formed from making $G'_k(x,y)$ conform with the object constraints:

$$G_{k+1}(x,y) = \begin{cases} G'_k(x,y) & (x,y) \notin \gamma \\ 0 & (x,y) \in \gamma, \end{cases} \tag{4.36}$$

where γ is the set that includes all the points where $G'_k(x,y)$ violates the constraints. The principal constraints are that the object be non-negative, and the size of the retrieved object may not exceed the known size of the object [69]. The error-reduction algorithm is so named because the error, defined in the object domain by

$$E_o^2 = \sum_x \sum_y \left| G_{k+1}(x,y) - G'_k(x,y) \right|^2, \tag{4.37}$$

and equivalently in the Fourier domain by

$$E_F^2 = \sum_u \sum_v \left| g'_k(u,v) - g_k(u,v) \right|^2, \tag{4.38}$$

decreases at each iteration [70]. Here the subscripts O and F denote the object and Fourier domains respectively. A possible stopping criterion for the algorithm is when the difference in errors in either domain from consecutive iterations, $E_{k+1}^2 - E_k^2$, falls below a certain threshold. However, although the error may approach zero and consequently stop the algorithm, this does not mean that the image has converged to the true solution. Instead, the algorithm may have converged to a local minimum.

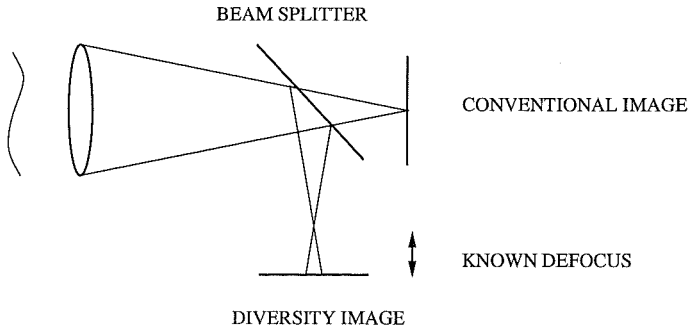

Figure 4.12 The layout of a phase diversity system [22].

One problem with phase retrieval algorithms such as the ER method is that since the object, $A(x, y)$, and its twin, $A^*(-x, -y)$, have the same modulus the two images are equally likely when starting from a random initial estimate [73]. There exist other more subtle local minima [72].

Another serious deficiency of the ER algorithm is its slow convergence. This lead Fienup [69] to propose the hybrid input-output algorithm to accelerate convergence. Although often faster, the convergence of the hybrid input-output is not assured, and attempts have been made to improve the convergence of the algorithm without losing the mathematical properties of ER [70,72].

In chapter 8, phase retrieval algorithms based on the GS and ER algorithms, but instead using the aperture images produced from a lenslet array placed in the focal plane as a constraint, are proposed.

4.5.2 Phase diversity

Phase diversity is an extension of phase retrieval and was introduced by Gonsalves in 1982 [74]. In addition to the image obtained at the focal plane of conventional phase retrieval, phase diversity generates one or more other images by introducing a known phase aberration, $\theta(x, y)$. This aberration is generally a defocus term. The phase diversity schematic is shown in Fig. 4.12. Phase diversity is able to recover the object being imaged, $o(u, v)$, as well as the unknown phase aberration, $\phi(x, y)$. For this reason, phase diversity is suited to estimating optical misalignment in telescopes [75].

The coherent transfer function, $H_1(x, y)$, which is defined in Section 3.1.4, for the conventional image is given by

$$H_1(x, y) = P(x, y) \exp[j\phi(x, y)], \tag{4.39}$$

where, as before, $P(x, y)$ is the aperture function. Similarly, the coherent transfer function for the phase diversity image is given by

$$H_1(x, y) = P(x, y) \exp[j(\phi(x, y) + \theta(x, y))]. \tag{4.40}$$

The conventional image, $d_1(u, v)$, is given by

$$d_1(u, v) = o(u, v) \odot s_1(u, v) + n_1(u, v), \tag{4.41}$$

where $n_1(u, v)$ is the noise in the conventional image channel and $s_1(u, v)$ is the PSF, which is related to the Fourier transform of the coherent transfer function by

$$s_1(u, v) = |h_1(u, v)|^2. \tag{4.42}$$

The phase diversity image is defined by

$$d_2(u, v) = o(u, v) \odot s_2(u, v) + n_2(u, v), \tag{4.43}$$

where the subscript, 2, refers to the corresponding quantities in the phase diversity channel.

The estimate of the spectrum of the object spectrum, $\hat{O}(x, y)$, is generated by

$$\hat{O}(x, y) = \frac{\mathcal{H}_1^*(x, y) D_1(x, y) + \mathcal{H}_2^*(x, y) D_2(x, y)}{|\mathcal{H}_1(x, y)|^2 + |\mathcal{H}_2(x, y)|^2} \tag{4.44}$$

where $\mathcal{H}(x, y)$ is again the OTF and $*$ is the complex conjugation operator. The phase aberration, $\phi(x, y)$, is then estimated in an iterative manner similar to phase retrieval from the two images and the estimated object spectrum.

4.5.3 Deconvolution from wavefront sensing

Deconvolution from wavefront sensing (DWFS) is a hybrid technique that combines elements of both adaptive optics and computer post processing to deblur the astronomical image. The technique was proposed by Primot *et al.* [37], and uses simultaneous short exposure images and wavefront sensing data as seen in Fig. 4.13. Mathematically, the problem of object reconstruction by DWFS can be written as a set of K linked deconvolution problems:

$$\begin{aligned} d_k(u, v) &= o(u, v) \odot s_k(u, v) + n_k(u, v) \\ &= g_k(u, v) + n_k(u, v), \end{aligned} \tag{4.45}$$

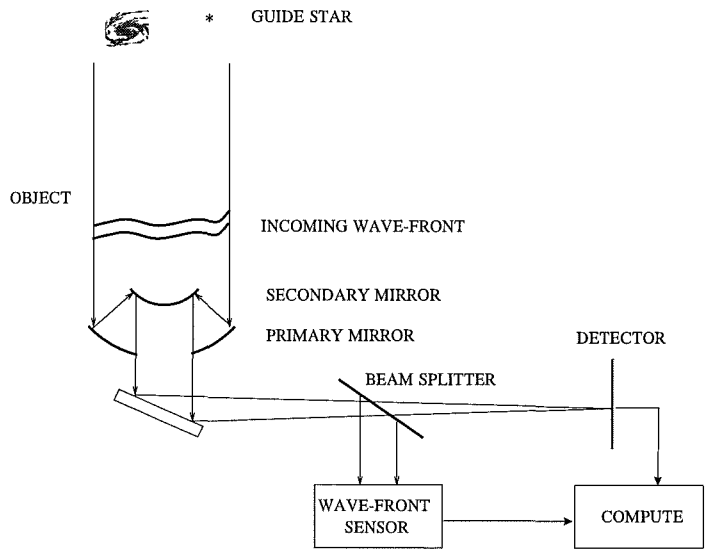

Figure 4.13 Block diagram of deconvolution from wavefront sensing.

where $o(u,v)$ is the astronomical object of interest, $s_k(u,v)$ is the PSF, $g_k(u,v)$ is the noise-free data and $n_k(u,v)$ is the additive noise on the data. The subscript k denotes the k^{th} realisation of the K frames of the respective quantities. DWFS is a non-recursive method for reconstructing the object where only the information measured in the wavefront sensor is used to form the PSF estimate, $\hat{s}_k(u,v)$. Mathematically, DWFS is a vector Wiener filter [76,77] that reconstructs the object spectrum $\hat{O}(x,y)$ [37]:

$$\hat{O}(x,y) = \frac{\langle D(x,y)\hat{\mathcal{H}}^*(x,y)\rangle}{\langle|\hat{\mathcal{H}}(x,y)|^2\rangle + c}, \tag{4.46}$$

where c is a constant. $D(u,v)$ is the spectrum of the data, and the notation $\langle\cdot\rangle$ denotes an ensemble. The estimate of the OTF, $\hat{\mathcal{H}}_k(u,v)$, is made using Eq. (3.43), reproduced here

$$\mathcal{H}(x,y) = P(x,y)\exp[j\hat{\phi}_k(x,y)] \otimes P(x,y)\exp[j\hat{\phi}_k(x,y)], \tag{4.47}$$

where the estimate of the phase, $\hat{\phi}_k(u,v)$, is measured by a wavefront sensor. The object distribution in the spatial domain, $\hat{o}(u,v)$, is obtained by taking an inverse Fourier transform of $\hat{O}(x,y)$.

The practical issues of calibration with DWFS and the results obtained using DWFS at the Observatoire de Lyon are discussed in Chapter 5.

4.5.4 Computer post-processing of adaptive optics images

Although computer post-processing and adaptive optics have been discussed as separate fields, it is possible to use the two in conjunction with each other. A number of authors [78–80] have proposed the use of computer post-processing techniques, such as DWFS or blind deconvolution, on the images partially compensated by adaptive optics. The computer post-processing system can take into account the physical limitations of the adaptive optics system that captured the images. For example, the post-processing algorithm can overcome the atmospheric modes that the wavefront sensor can see but the deformable mirror cannot correct for. Problems with the so-called 'waffle' modes [81], which the wavefront sensor cannot see but the deformable mirror can correct, can also be alleviated.

Chapter 5

Practical Implementation of DWFS

5.1 Introduction

The Shack-Hartmann wavefront sensor, which is introduced in Section 4.1.1, estimates the wavefront slope over each subaperture by determining the displacement of the low resolution images from the reference (no wavefront aberration) positions. In theoretical analyses of the Shack-Hartmann sensor [37,43], these reference positions are assumed known. However, these reference positions have to be measured in a calibration procedure. Therefore for an accurate wavefront estimate, an accurate calibration of the reference positions is essential. The effect of incorrectly measuring the reference positions for the Shack-Hartmann sensor is similar to noise on the measurements. These reference errors cannot be corrected by either an open or closed loop system since neither can distinguish the true signal from the noise. Any error in estimating the reference positions appears as an aberration in the reconstructed wavefront.

The currently used method for determining the reference positions is to build within the instrument a reference beam, which when imaged provides the unaberrated centres of the images. This is henceforth referred to as calibration with a grid reference. In this chapter, a new approach for calibrating these reference positions is proposed that, unlike grid calibration, does not require any physical hardware. This second method is to observe a single bright star and maximise the Strehl ratio with respect to the reference positions. This new method of calibration, which is performed entirely through software, is referred to as sky reference calibration throughout this chapter. The work done on this new calibration method was completed in conjunction with a number of authors, principally R.G. Lane [82]. Sky reference calibration of the Shack-Hartmann sensor is demonstrated to give equivalent performance to grid calibration using DWFS on data obtained from the SPID (SPeckle Imaging by Deconvolution) instrument at the Observatoire de Lyon [83]. Al-

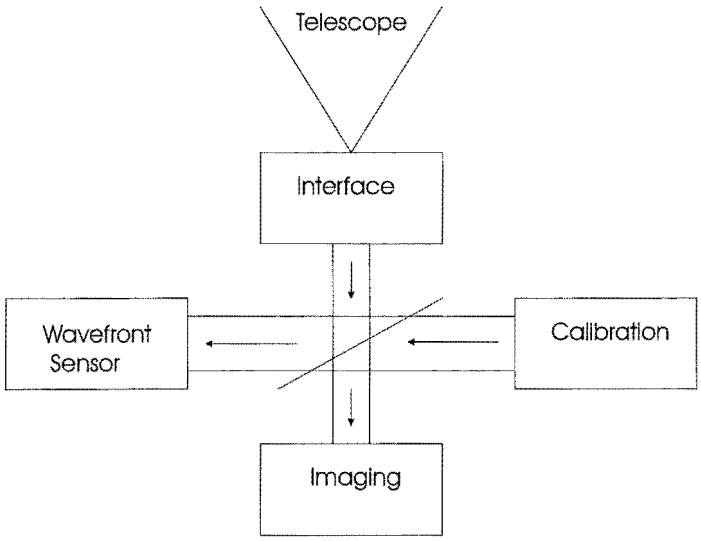

Figure 5.1 Layout of the modules of SPID

though this new approach is demonstrated using a computer post-processing scheme, it is also applicable to adaptive optics systems.

In Section 4.2, it is observed that nulls in the reconstructor, $\Theta^T\Theta$, where Θ is the interaction matrix, occur for certain Zernike modes for the Shack-Hartmann sensor. The effect of these nulls in the reconstructor on the coefficients of the Zernikes of the estimated wavefront using DWFS on data from the SPID instrument is also investigated in this chapter.

The operation of the SPID instrument is outlined in Section 5.2. The calibration of the SPID instrument for DWFS is discussed in Section 5.3. The results from using DWFS on data from the SPID instrument with the grid and sky reference calibration schemes are presented in Section 5.4. The effect of the reconstructor structure on wavefront estimation with DWFS is shown in Section 5.5. Conclusions for the work outlined in this chapter on calibration and the reconstructor effect for DWFS are reached in Section 5.6.

5.2 The SPID instrument

The SPID instrument was designed for high angular resolution astrophysics using bispectrum analysis. SPID consists of four main modules as shown in Fig. 5.1: the interface module, the wavefront sensor, the imaging module and the calibration module. The interface module collimates the beam from the telescope to create an image of the pupil at a fixed position and size. The light from the telescope is then split between the imaging and wavefront sensor modules.

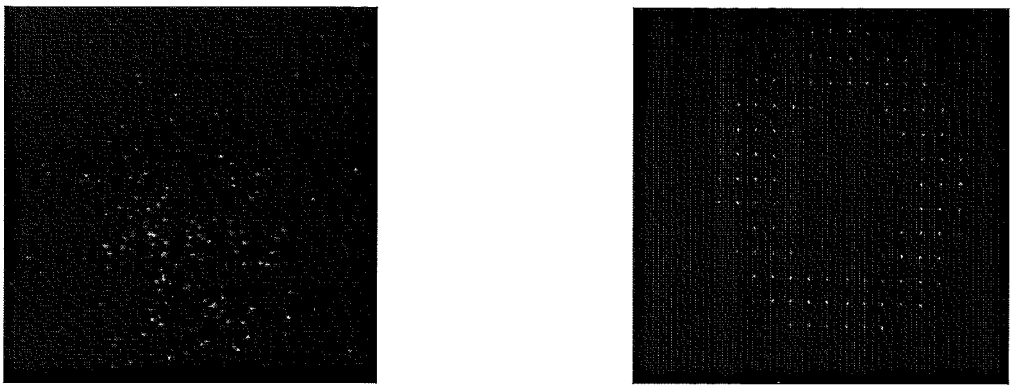

(a) (b)

Figure 5.2 The raw data captured using the SPID instrument at the Lyon observatory. (a) A single short exposure image. (b) A single Shack-Hartmann frame.

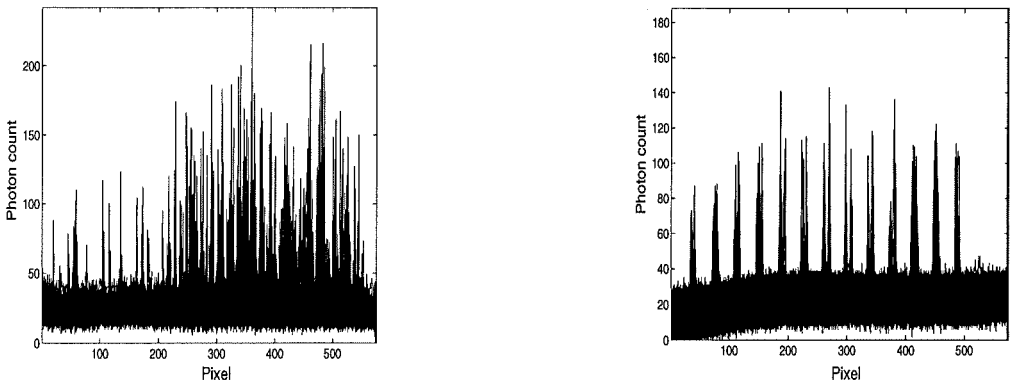

(a) (b)

Figure 5.3 Cross section of measured channels: (a) short exposure image, and (b) Shack-Hartmann.

The imaging module produces two images in each spectral channel on a photon detecting camera, CP40. An example short exposure image captured with CP40 is shown in Fig. 5.2(a). The two images are duplicated to overcome the so-called photon-counting hole [83], which arises when there is more than one concurrent photoevent at the detector. When the SPID instrument is being calibrated, one of these two images is used for calibration purposes and the other to assess the performance of the system. The imaging wavelength can be varied between 400 nm and 720 nm, and the bandwidth between 0.1 nm and 8 nm. The images formed are viewed through a video camera, which has significant measurement noise as can be seen in Fig. 5.3(a).

The wavefront sensor module consists of a Shack-Hartmann wavefront sensor. The lenslet arrays vary from 9×9 to 40×40 lenslets. The choice of the number of lenslets is determined by the seeing, r_0, and the light levels. A single Shack-Hartmann frame with a 14×14 lenslet array is shown in Fig. 5.2(b). The wavefront sensor uses a CCD detector synchronised with the image module to capture the wavefront sensing data. The noise on the Shack-

Hartmann channel is apparent in Fig. 5.3(b).

A calibration module is provided to calibrate the wavefront sensor and the imaging module. For SPID, this calibration is performed in software. The particular calibration issues for SPID are discussed in more detail in the next section.

5.3 Calibration of the SPID instrument

The calibration errors that need to be corrected for SPID can be divided into two groups: those That are common to both adaptive optics and computer post-processing, and those that are specific to computer post-processing. The first group is not improved by feedback and involves providing a good set of reference positions for the Shack-Hartmann sensor. The second is more critical in open loop processing, and ensures that the PSF estimated from the wavefront sensor has the correct orientation, sampling and scale when compared with the data gathered from the imaging channel. Both groups of calibration error can be minimised by observing a point source and maximising the Strehl ratio with respect to the considered parameter. This approach has the advantage of optimising directly the desired measure of image quality, which here is the Strehl ratio.

Ideally, the wavefront sensor should measure only the wavefront aberrations that affect the imaging channel. However, if the wavefront aberration is different on the wavefront sensing and imaging paths, then there is an unwanted aberration introduced to the wavefront estimate. This aberration is fixed and can be estimated as parameters of the system by optimising the Strehl ratio for each parameter (Zernike mode) considered.

5.3.1 Calibration errors common to adaptive optics and post-processing

One of the problems with a grid calibration of the reference positions for the centroids of the Shack-Hartmann sensor is that the CCD used to capture the wavefront sensing data is not optimal for imaging the reference beam. This is due to the presence of read noise, which is discussed in Section 3.4. Read noise increases with the number of pixels and at low light levels, and in the short exposure images, this form of noise dominates. The optimal CCD pixel size is therefore a trade-off between the quantisation noise from having a fixed number of pixels and the read noise determined by the photon count of the short exposure image. However, when the reference beam is imaged to form the reference positions, a much higher photon count is available. The read noise is hence lower and the short exposure trade-off between the quantisation and read noises is now sub-optimal. Ideally, a smaller pixel size should be used to calculate the reference positions optimally, but this cannot be done because the same CCD must be used be used for both calibration and measurement purposes.

Zernike mode	Grid calibration coefficient	Sky reference calibration coefficient
Z_4	-0.0069	0.0976
Z_5	0.0011	0.0121
Z_6	-0.0028	-0.0147
Z_7	0.0022	0.0522
Z_8	-0.0035	-0.0623
Z_9	-0.0007	-0.0077
Z_{10}	-0.0027	-0.0027
Z_{11}	-0.0070	0.0141
Z_{12}	-0.0014	-0.0018
Z_{13}	0.0003	-0.0026
Z_{14}	-0.0021	-0.0035
Z_{15}	-0.0016	0.0061

Table 5.1 The characterisation of the fixed telescope aberrations using Zernike polynomials for the grid calibration and sky reference calibration schemes.

The alternative to grid calibration of the reference positions is to consider the long exposure image from the wavefront sensing channel. This sky calibration removes the need for a calibration laser beam. The short exposure images capture the instantaneous centroid positions. These centroid positions move about the reference position with the constantly changing atmospheric turbulence. The long exposure image is the sum of the short exposure images and hence the centroids of the long exposure image are the sum of the centroids on the short exposure images. The noise on the long exposure reference centroid position from averaging N frames is $\frac{1}{N}$ times as large as that on a short exposure image.

A drawback of calculating the centroid reference positions from imaging the sky is that the image of the sky is captured through the aberrations of the telescope. This method for calculating the centroid reference positions therefore does not give the inherent aberrations of the optical system including the telescope. These aberrations are constant from frame to frame, and can be represented as a sum of Zernike polynomials excluding piston, tip and tilt. The first 12 of these modes, starting with defocus, are used here, and the coefficients of these modes for both the grid and sky reference calibration schemes are shown in Table 5.1. These coefficients are obtained by optimising the Strehl ratio from the reconstruction of a point source with respect to the values of the coefficients. Examination of the coefficients shows that the use of a reference grid produces small errors in which no Zernike mode dominates. The use of a sky reference indicates strong defocus and coma terms, which is consistent with the expected telescope aberrations.

5.3.2 Calibration errors specific to computer post-processing systems

DWFS is based on Eq.s (4.46) and (4.24). In Eq. (4.46), the data spectrum, $D(x, y)$, is formed by the Fourier Transform of the observed data, $d(u, v)$. In contrast, the OTF, $\mathcal{H}(x^{'}, y^{'})$, is computed by combining a measurement of the aperture (Fig. 3.5(b)) with a phase computed as the sum of Zernike polynomials weighted according to the coefficients computed from Eq. (4.24). The prime on the coordinates indicates that in practice the coordinates of D and $\mathcal{H}$ are rotated with respect to each other and sampled at different rates. This calibration error is overcome by introducing two parameters, ζ and ϕ, where

$$\begin{aligned} x &= \zeta[x^{'} \cos\phi - y^{'} \sin\phi] \\ y &= \zeta[x^{'} \cos\phi + y^{'} \sin\phi]. \end{aligned} \tag{5.1}$$

The Strehl ratio is optimised with respect to ζ and ϕ. Computationally, this transformation can be implemented by a process of interpolation. Rather than compute this interpolation on each data frame, it is more efficient to pre-compute the interpolated measured aperture and basis Zernike polynomials.

Another source of error is in the scaling of the interaction matrix, Θ, used in Eq. (4.24). Although the scale can be computed from the optical design, the results are improved by allowing the exact value to be optimised. This is incorporated by scaling the computed Θ by a factor β, and optimising the Strehl ratio with respect to β.

5.4 Experimental Results

In this section, a comparison of the results obtained using DWFS with the grid and sky reference calibration schemes for SPID is presented. A 20×20 Shack-Hartmann lenslet array is used, and the exposure time is chosen to be 2ms to ensure the atmosphere is essentially frozen. The object of observation is Pollux, a single bright star. A total of 1000 frames, with an average of 80 photons per frame, is used. The phase reconstructions are made using the first 100 Zernike modes (excluding piston). The centroiding algorithms used are a traditional approach, which is described by Eq. (4.4) and (4.5), and the model based approach described by Leung *et al.* [84].

Fig. 5.4(a) shows the long exposure image, and Fig. 5.4(b) the result of DWFS using model centroiding and the grid calibration. Although the image is improved, the Strehl obtained, 0.072, is not a dramatic result. The result shown in Fig. 5.4(b) corresponds to the c value of Eq. (4.46) obtained by optimising the Strehl ratio of the reconstruction after removing all negative pixels in the image and renormalising the light level. The Strehl ratio with the zeroing of negative pixels and renormalisation of light levels is denoted as the modi-

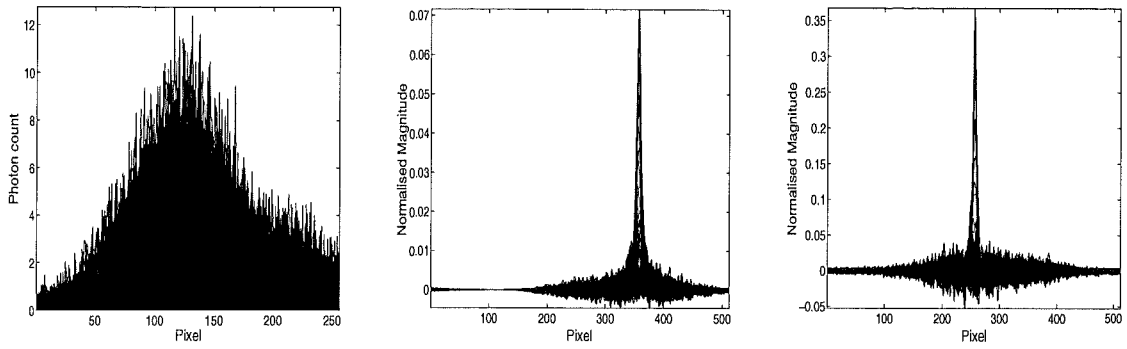

(a) (b) (c)

Figure 5.4 Cross section of : (a) the long exposure image with centroiding (the y axis is the photon count). (b) the reconstructed image obtained using the magnitude from the Wiener vector filter (the y axis is the magnitude normalised to the peak of the diffraction-limited PSF). (c) the reconstructed image obtained using the true MTF as the magnitude and the phase from the Wiener vector filter (the y axis is the magnitude normalised to the peak of the diffraction-limited PSF).

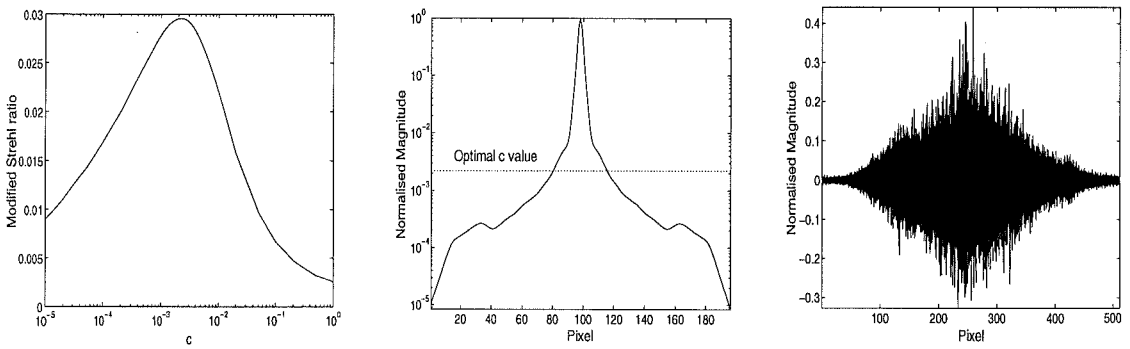

(a) (b) (c)

Figure 5.5 (a) The modified Strehl ratio obtained for differing values of the constant c of Eq (11). The values of c are normalised with respect to the maximum value of $\langle|\hat{\mathcal{H}}(x,y)|^2\rangle$. (b) The normalised magnitude of $\langle|\hat{\mathcal{H}}(x,y)|^2\rangle$ with the optimal value of c superimposed. (c) An under regularised image resulting from optimising the Strehl ratio for c directly without removing the negative pixels first.

fied Strehl ratio. Fig. 5.5(a) shows the variation in the modified Strehl ratio, the peak of which is in agreement with a visual assessment of the image quality. It is not possible to optimise c by using the conventional Strehl ratio directly, since this produces a highly under-regularised solution with the Strehl ratio determined by a random noise peak, such as in Fig. 5.5(c). The relationship of the optimal value of c, 0.0022, to $\langle|\hat{\mathcal{H}}(x,y)|^2\rangle$ is shown in Fig. 5.5(b).

Examination of the reconstructed phase, displayed in Fig. 5.6(a) and (b), shows that the principal problem in the DWFS method is a poor estimate of the object spectral magnitude, since the phase shows significant improvement. The reasons for the poor magnitude estimate have been described in Ref. [85] and it is noted that alternative techniques such as bispectrum are also not able to directly estimate the object magnitude.

Calibration	Centroiding algorithm	Fixed aberration estimation	Wiener Strehl ratio	Phase-only Strehl ratio
Grid	Model	Yes	0.0716	0.3672
Grid	Model	No	0.0674	0.3480
Grid	Traditional	Yes	0.0571	0.3069
Grid	Traditional	No	0.0562	0.3020
Sky	Model	Yes	0.0612	0.3357
Sky	Model	No	0.0259	0.1664
Sky	Traditional	Yes	0.0560	0.3264
Sky	Traditional	No	0.0260	0.1785

Table 5.2 The Strehl ratios achieved with the different calibration schemes for the two centroiding algorithms for 1000 frames of a single bright star, Pollux. The first column of Strehl ratios is calculated using the magnitude and phase obtained from the Wiener vector filter. The second column is for the Strehl ratios calculated using the phase obtained from the Wiener vector filter and using the true MTF as the magnitude.

In order to compare the accuracy of the phase estimates from Eq. (4.46), a phase only estimate is calculated by combining the phase estimate with the true MTF (Fig. 5.6(c)). The reconstructed image for this phase only estimate is shown in Fig. 5.4(c). Not surprisingly, the use of a calibration grid outperforms a sky reference when no attempt is made to estimate the fixed aberrations. The results confirm that model based centroiding produces superior reconstructions of the phase compared to traditional centroiding [84].

As expected, the estimation of the fixed aberrations makes a more significant improvement to the Strehl ratio when a sky reference is used. For the model centroiding, the improvement obtained by incorporating the fixed aberrations for the grid calibration is only 6 % whilst for the sky reference the result is a 100 % improvement. The results show that a sky reference can produce an estimate of similar quality to a laser reference, without the need for separate calibration hardware.

The improvement in the Strehl ratio is dependent on the number of frames of data that is used in the reconstruction. However, the computational complexity also increases linearly with the number of frames used. A trade-off between these two factors was made and 1000 frames used for all the reconstructions tabulated in Table 5.2. When the full 2500 frames available are used to reconstruct Pollux with a grid calibration, model centroiding and compensation for the fixed aberrations of the telescope, a Strehl of 0.4120 is achieved. This represents a 12 % improvement in performance for a 150 % increase in computation.

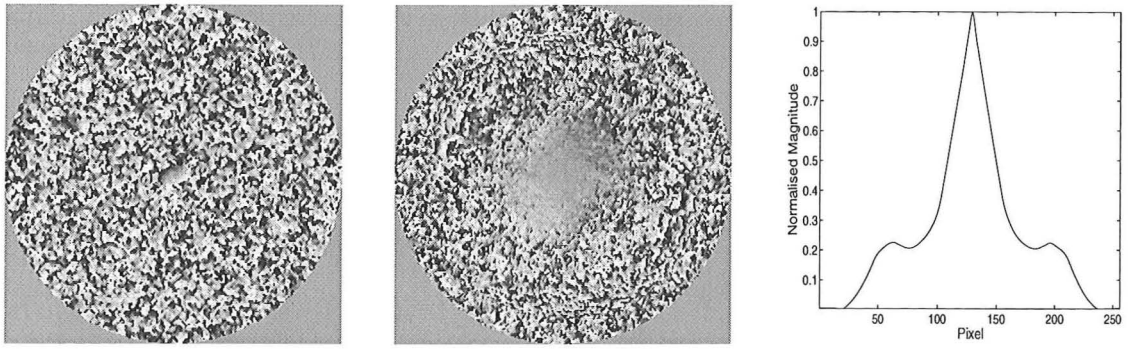

(a) (b) (c)

Figure 5.6 The phase of the object, Pollux, from (a) the long exposure image (b) using DWFS with 2500 frames of data, model centroiding, the grid calibration and compensation for the fixed aberrations. (c) The true Modulation Transfer Function (MTF).

5.5 Reconstructor Effect on a single bright star

The problem of the inability of the Shack-Hartmann wavefront sensor to reconstruct certain Zernike modes can be seen when reconstructing a single bright star using the experimental data captured with SPID and processed with DWFS, since there is a significant deviation from the theoretical predictions from Kolmogorov statistics.

The mean-squared residual phase error for the first 10 Zernike modes are tabulated in Table 3.3, and Eq. (3.75) holds for the higher order terms. The aperture averaged mean-squared phase error for each individual mode is therefore given by the difference between consecutive aperture averaged residual phase error terms. This is a monotonically decreasing sequence for the higher order terms, which means that as the Zernike order increases each mode adds less to the mean-squared phase error than the previous term.

The variance of the estimates of the coefficients of the first 100 Zernike modes, which is equivalent to the aperture averaged mean-squared phase error of these modes, is shown in Fig. 5.7. The weighting, α, between the noise and Zernike covariance matrices of Eq. (4.24) has been set to 0, and hence the reconstructor is a least-squares estimator with no prior information included. It is obvious that the theoretical ideal of a monotonically decreasing sequence is not achieved. Instead there are distinct peaks, which correspond to modes across the aperture where the wavefront sensor is insensitive and the reconstructor has amplified the noise.

The peaks in the variance curve of Fig. 5.7 are periodic with respect to the radial order, n, of the Zernike polynomials, i.e. exactly one peak occurs for each value of the radial order, which is an integral quantity. These peaks are generally present at points of low azimuthal order, m, and occur at the same modes as the nulls of Fig. 4.7 for the mean-squared value of the rows of $\Theta^T\Theta$.

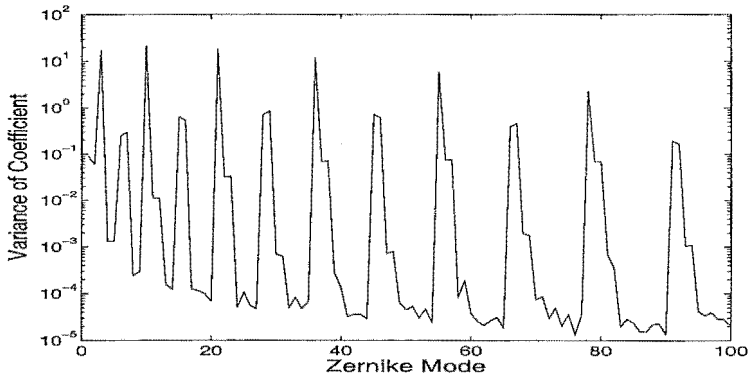

Figure 5.7 The variance of the first 100 Zernike coefficients (excluding piston) for Pollux where the weighting, α, on the prior information is 0. This reduces to a least-squares solution.

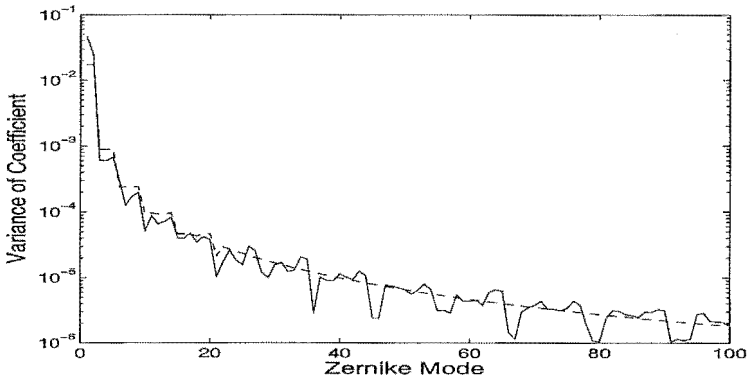

Figure 5.8 The variance of the first 100 Zernike coefficients (excluding piston) for Pollux where the weighting between the noise covariance and Zernike covariance matrices in the reconstructor is optimised. The aperture averaged mean-squared phase error predicted by Noll (dashed line) for a Fried parameter, r_0, of 11cm is superimposed.

The least-squares reconstructor results in errors in the estimation of the coefficients of the Zernike modes by up to five orders of magnitude. When α is zero, the reconstructor amplifies the modes corresponding to the nulls in $\Theta^T\Theta$ and hence amplifies the noise on the data for these modes relative to the other modes. This leads to poor estimates of these modes, which is shown by peaks in the variance of the values of the coefficients.

When the weighting, α, between the noise and Zernike covariance matrices is optimised, the Zernike modes that correspond to peaks in Fig. 4.7 now correspond to nulls, as shown in Fig. 5.8. The dashed line shown in Fig. 5.8 is the predicted mean-squared aperture averaged phase error. When the weighting between the noise and Zernike covariance matrices is optimal, the reconstructor underestimates the modes that correspond to nulls in $\Theta^T\Theta$ to avoid amplifying the effects of noise on the reconstructed wavefront.

The weighting of α, and hence the erroneous estimation of some of the Zernike modes,

also has a significant impact on the overall performance of the reconstruction, which is here given by the Strehl ratio. An optimised solution produces a Strehl ratio that is 11 times higher than a least-squares solution.

5.6 Conclusions

In this chapter, the practical methodology for calibrating a Shack-Hartmann wavefront sensor for post-processing of astronomical imaging is presented. In particular, the technique of calibrating the Shack-Hartmann sensor by optimising the Strehl ratio of an observed source, instead of using a calibration laser, is introduced. The method requires parameterisation of the optical aberrations but produces results of a similar quality at a reduced physical complexity and cost. This calibration technique can also be applied to adaptive optics systems.

The results presented in this chapter confirm previously published studies that have shown the difficulties in estimating the magnitude of the object from DWFS [86]. However, the results achieved from DWFS show a marked improvement in the estimated phase of the object over the uncompensated data.

It was shown that certain Zernike modes in the reconstructor for a Shack-Hartmann sensor are more sensitive to noise, and this can lead to errors in the estimation of the coefficients of these modes. If the weighting between the noise and Zernike covariance matrices is optimised, then these errors are avoided by underestimating these particular modes.

Chapter 6

Wavefront Sensing with a Lenslet Array at the Focal Plane

6.1 Introduction

As a wavefront propagates, geometric optics predicts that the light at each point in the wavefront travels perpendicularly to that point in the wavefront. Fig. 6.1 shows a region of the wavefront of width Δx that is propagated by a distance z. The wavefront sensing problem is to determine the displacement of the light, a, and hence the mean slope over the region of the wavefront. This linear relationship between the slope and the light displacement underlies most wavefront sensing techniques.

The estimate of displacement, and hence the mean slope over the region, can be made with an uncertainty of Δa. The term slope accuracy, σ_θ, is defined as the error in the slope measurement and it is proportional to the uncertainty of the displacement, Δa. For a pure slope over a finite aperture, it can be shown that the accuracy of the slope estimate improves as the wavefront is propagated as far as possible [45]. In practice, a lens is employed to allow a large effective propagation distance in a finite range.

In wavefront sensing, the ultimate objective is to estimate the wavefront phase. The phase difference error, σ_ϕ, (in radians) across a region in the aperture, Δx, is linearly related to the slope accuracy, σ_θ, by

$$\sigma_\phi = \frac{\sigma_\theta 2\pi \Delta x}{\lambda}, \tag{6.1}$$

where λ is the imaging wavelength.

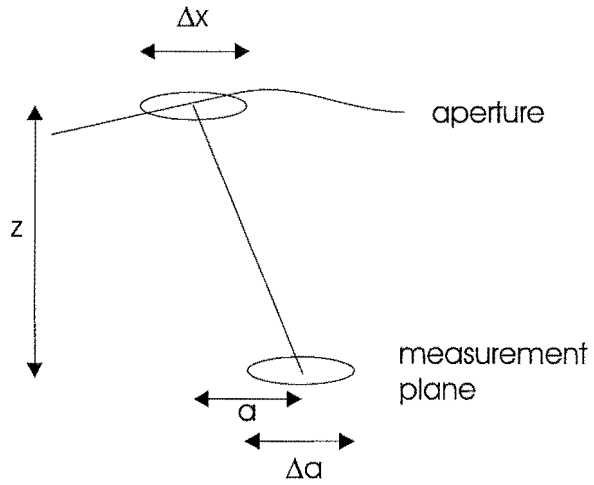

Figure 6.1 The propagation of a region of a wavefront of width Δx over a distance z allows the estimation of the displacement, a, with an uncertainty, Δa.

In the following discussion, the wavefront is assumed to emanate from a point source. If the width of the region in the aperture, Δx, is reduced, then this increases the resolution of the slope estimates in the aperture plane, but causes the light in the measurement plane to be more spread out. Consequently, the uncertainty in the displacement at the measurement plane, Δa, and hence the uncertainty in the slope at the corresponding point in the aperture, increases. Conversely, as the width of the region of the wavefront in the aperture is increased, the resolution in the aperture is degraded but the resolution with which the displacement in the focal plane can be determined improves. This inverse relationship between the resolution of the estimates at the two planes is an inherent consequence of the Fourier relationship between the two planes, and introduces a limit on the performance of the Shack-Hartmann, pyramid and curvature sensors.

Although the most accurate measurement is obtained by using the entire aperture, the wavefront is almost never in practice a pure slope. As a consequence, it is necessary to subdivide the wavefront in order to accurately model the more complicated shapes of a practical wavefront. Increasing the subdivision causes the slope measurements within a region to be less accurate. This is the fundamental trade-off that is made in all wavefront sensors.

The subdivision of the wavefront can be achieved explicitly, as in the Shack-Hartmann or pyramid sensors, by a lenslet array placed in the wavefront as shown in Fig. 6.2(a) and (b) respectively. In the curvature sensor, which is discussed in Section 4.1.2, the wavefront curvature is estimated implicitly from two defocused images of the aperture, and the effective subdivision is determined by the amount of defocus of the two images. This chapter concentrates on the explicit subdivision of the wavefront, in particular the relationship be-

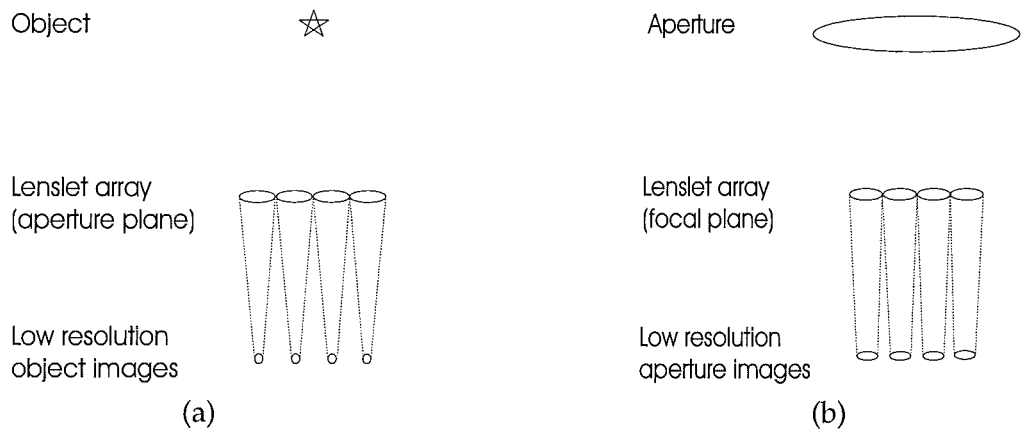

Figure 6.2 Comparison of (a) the Shack-Hartmann wavefront sensor and (b) the pyramid sensor implemented as a lenslet array.

tween the Shack-Hartmann and pyramid sensors.

As discussed in Section 4.1.1, the Shack-Hartmann sensor enforces the size of the region in the aperture directly by placing a lenslet array in the aperture plane of the telescope as shown in Fig. 6.2(a). The lenslet array subdivides the complex field in the aperture, with each lenslet forming a low resolution image of the object. The size of the lenslets in the array, d, determines the spatial resolution attainable at the aperture plane.

The slope accuracy, or slope measurement error, σ_θ, within a single subaperture for the Shack-Hartmann sensor is given by [44, 87]

$$\sigma_\theta = \frac{\theta_b}{\mathrm{SNR}}, \tag{6.2}$$

where θ_b is the effective spot (image) size and SNR is the signal-to-rms noise ratio for the slope measurement. Reducing the lenslet size, d, affects both θ_b and the SNR. For small lenslets $\theta_b \approx \lambda/d$, thus reducing d causes θ_b to increase. Substituting this approximation in Eq. (6.1) gives

$$\sigma_\phi \approx \frac{2\pi}{\mathrm{SNR}}, \tag{6.3}$$

which shows that the phase difference error across a lenslet is unaffected by θ_b.

The SNR of an image displacement measurement is a function of the number and distribution of photons available, and the level of read noise in the detector. In order to maximise the SNR, a quadrant detector is often employed [44]. For the quadrant detector, the SNR

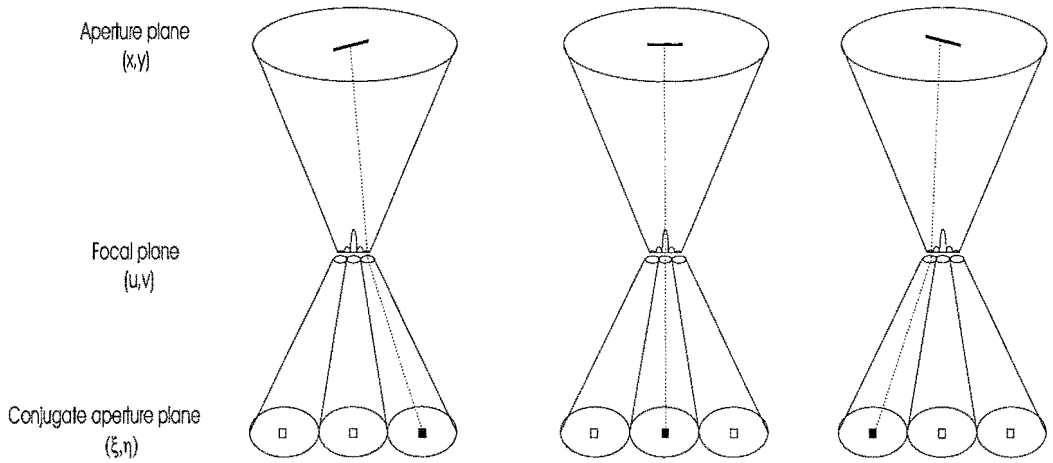

Figure 6.3 The effect of a local tilt at a point in the aperture on the corresponding point in the aperture images.

for the slope measurement is given by [87]

$$\mathrm{SNR} = \frac{N_p}{\sqrt{N_p + 4N_b + 4\sigma_e^2}}, \tag{6.4}$$

where N_p is the total number of photons in the subaperture, N_b is the number of background photons per pixel, and σ_e is the read noise per pixel. Two separate noise regimes are considered. If the detector is dominated by read noise (ie $4\sigma_e^2 \gg N_p + 4N_b$), then the SNR is inversely proportional to the level of read noise. Thus the slope measurement error, σ_θ, in this case is proportional to the level of read noise.

When photon noise from the source dominates (ie $N_p \gg \sigma_e^2 + 4N_b$), then from Eq. (6.4) the SNR is proportional to the square root of the total number of photons, $\mathrm{SNR} \propto \sqrt{N_p}$. Assuming a constant flux density, the number of photons in each subaperture is proportional to the size of the lenslets, ie $N_p \propto d^2$. Hence when photon noise dominates, the SNR $\propto d$, and substituting this in Eq. (6.2) shows that $\sigma_\theta \propto 1/d^2$. The slope measurement error, σ_θ, is inversely proportional to the lenslet diameter squared. Combining these results yields

$$\sigma_\phi \propto \frac{2\pi}{d}, \tag{6.5}$$

which shows that under the given assumptions the phase difference error across the lenslet is inversely proportional to the lenslet diameter.

An alternative method for wavefront sensing uses a lenslet array at the focal plane of the telescope with each lenslet re-imaging the aperture and forming a low resolution image of the aperture as shown in Fig. 6.2(b). A geometric optics explanation of how the slope of the wavefront is determined by a lenslet array placed in the focal plane is shown in Fig.

Figure 6.4 (a) Linear operation occurs in the Shack-Hartmann quad-cell when the image intersects all four pixels. Alternatively for the 2×2 lenslet array at the focal plane, linear operation occurs when the spot in the focal plane intersects all four lenslets. (b) Saturation occurs in the Shack-Hartmann quad-cell when the image does not intersect all four pixels. For the 2×2 lenslet array at the focal plane, saturation occurs when the spot does not intersect all four lenslets.

6.3. As the local tilt at a point in the aperture changes, the light from this point is displaced by a different amount in the focal plane, and consequently illuminates the corresponding point in the aperture image on which it falls. If the lenslets are significantly larger than the expected displacement of the image, then the measurements obtained from a 2×2 lenslet array placed in the focal plane are equivalent to the pyramid sensor, provided the common point of the lenslets corresponds to the apex of the pyramid.

The discussion so far assumes that the slope measurement for the Shack-Hartmann is linearly related to the displacement of the spot. In practice, the detector is inevitably made of pixels of finite size. The drawback of this approach is most apparent in the quad-cell detector. If the low resolution image is not present in all four pixels, Fig. 6.4(b), the sensor saturates. When operating in open loop or when starting a closed loop system, this poses a significant problem because there is only a finite region over which there is a linear relationship between the sensor response and the wavefront slope. The problem is less significant when dealing with a closed loop system that is already successfully tracking the atmospheric turbulence, as the expected range of slope errors is much reduced. The linear range of a wavefront sensor is defined here as the range of wavefront slopes over which there exists a linear relationship between the measurements and the wavefront slope. The sensitivity of the sensor is proportional to the slope of this linear function.

With the lenslet array at the focal plane, the issue is not the finite size of the detector pixels, but the finite size of the lenslets. Consider the 2×2 array of lenslets, which is the pyramid sensor configuration. When the spot in the focal plane falls on the central intersection of the four lenslets, Fig. 6.4(a), then there is a linear relationship between the sensor response and the wavefront slope. However, when the spot is not subdivided by all four lenslets, Fig. 6.4(b), the sensor saturates in a manner directly analogous to the quad-cell detector. As with the quad-cell detector, saturation is less of an issue in closed loop since the residual

aberrations are not expected to be as large as in open loop. The ability to modulate the lenslet array's position can be used to increase the linear range of the sensor but at a price in sensitivity. This is discussed further in Sections 6.2 and 6.3.

The remainder of this chapter is structured as follows. Section 6.2 outlines the mathematical properties of a lenslet in the focal plane. The use of an array of lenslets in the focal plane is discussed in Section 6.3. Section 6.4 shows simulation results in the presence of atmospheric turbulence. Conclusions for this chapter are drawn in Section 6.5.

6.2 Mathematical background

The presence of a lens in the focal plane reverses the Fourier transform relationship to produce an image in the conjugate aperture plane, described by coordinates (ξ, η). The complex field in the conjugate plane is a low-pass filtered image of the aperture. The filtering is due to the finite size of the lens, which is described mathematically as a spatial filter $h(u, v)$.

Denoting the aberrated phase of the wave as $\phi(\xi, \eta)$ and the magnitude of the complex amplitude at the aperture as $P(\xi, \eta)$, the resulting aperture image in the conjugate aperture plane, $I(\xi, \eta)$, from placing a lenslet at the focal plane is given by [49]

$$I(\xi, \eta) \propto \left| \mathcal{F}^{-1}\Big[h(u, v) \times \mathcal{F}\Big[P(\xi, \eta) \exp[j\phi(\xi, \eta)] \Big] \Big] \right|^2 . \tag{6.6}$$

Eq. (6.6) can be expanded by making use of the convolution theorem to produce

$$I(\xi, \eta) \propto \left| \mathcal{F}^{-1}\left[\mathcal{F}\left[\mathcal{F}^{-1}\Big[h(u, v) \Big] \odot \mathcal{F}^{-1}\Big[\mathcal{F}\big[P(\xi, \eta) \exp[j\phi(\xi, \eta)] \big] \Big] \right] \right] \right|^2 . \tag{6.7}$$

Using the linearity of the Fourier transform and the convolution operator Eq. (6.7) simplifies to

$$I(\xi, \eta) \propto \Big| H(\xi, \eta) \odot P(\xi, \eta) \exp[j\phi(\xi, \eta)] \Big|^2 . \tag{6.8}$$

The aperture image formed from spatial filtering in the focal plane is thus the convolution of the complex amplitude at the aperture with the IFT of the spatial filter.

Since a lenslet array traditionally consists of square lenses, a lenslet with a linear dimension of $\Delta u \times \Delta v$ centred at a point (u', v') in the focal plane is considered. The corresponding

spatial filter, $h(u,v)$, for this single lenslet is

$$h(u,v) = \begin{cases} 1 & u' - \frac{\Delta u}{2} \leq u \leq u' + \frac{\Delta u}{2} \text{ and } v' - \frac{\Delta v}{2} \leq v \leq v' + \frac{\Delta v}{2} \\ 0 & \text{otherwise} \end{cases} \tag{6.9}$$

and the IFT of this spatial filter, $H(\xi,\eta)$, can be calculated using Eq. (2.24) as:

$$H(\xi,\eta) = \Delta u \,\mathrm{sinc}(\xi\Delta u)\exp[j2\pi\xi u']\;\Delta v \,\mathrm{sinc}(\eta\Delta v)\exp[j2\pi\eta v']. \tag{6.10}$$

The aperture image formed from this lenslet in the focal plane is given by substituting Eq. (6.10) into Eq. (6.8),

$$I(\xi,\eta) \propto \left|\Delta u \,\mathrm{sinc}(\xi\Delta u)\exp[j2\pi\xi u']\;\Delta v \,\mathrm{sinc}(\eta\Delta v)\exp[j2\pi\eta v'] \odot P(\xi,\eta)\exp[j\phi(\xi,\eta)]\right|^2. \tag{6.11}$$

The aperture image formed from a single lenslet in the focal plane is the magnitude squared of the convolution of a two-dimensional sinc function with the complex amplitude in the aperture. The effect of convolving with the sinc function is to smear the aperture image $I(\xi,\eta)$, limiting the resolution with which the slopes can be determined in the aperture. The lobe width of the sinc function is determined by the width of the lenslet in the focal plane, and the phase by the position of the lenslet in the focal plane. Because of the Fourier relationship between the focal and conjugate aperture planes, as the size of the lenslets increase then the width of the main lobe of the sinc function of Eq. (6.11) decreases. Thus as the lenslet width decreases, the main lobe of the sinc increases, and the number of modes in the atmospheric turbulence that can be measured in the aperture decreases.

6.2.1 Slope filtering

It is the linear phase term of the two-dimensional sinc function in Eq. (6.11) that when convolved with the complex field in the aperture isolates the slopes in the aperture. Assuming the scintillation in the aperture is small and that the phase can be expressed as a pure tilt in the ξ direction only, the complex field in the aperture, $P(\xi,\eta)\exp[j\phi(\xi,\eta)]$, simplifies to $\exp[j2\pi k\xi]$, where k is the coefficient of the tilt aberration. Eq. (6.11) simplifies to

$$I(\xi,\eta) \propto \left|\Delta u \,\mathrm{sinc}(\xi\Delta u)\exp[j2\pi\xi u']\Delta v \,\mathrm{sinc}(\eta\Delta v)\exp[j2\pi\eta v'] \odot \exp[j2\pi k\xi]\right|^2. \tag{6.12}$$

In order to simplify the analysis of the problem the telescope is assumed to have a square aperture of dimension D. Expansion of Eq. (6.12) with Euler's identity and application of

the definition of the convolution integral yields

$$I(\xi,\eta) \propto \left| \int_{-\frac{D}{2}+\eta}^{\frac{D}{2}+\eta} \int_{-\frac{D}{2}+\xi}^{\frac{D}{2}+\xi} \left(\frac{\exp[j\pi\xi'(\Delta u + 2u')] - \exp[-j\pi\xi'(\Delta u - 2u')]}{2j\pi\xi'} \right) \right.$$
$$\left. \times \left(\frac{\exp[j\pi\eta'(\Delta v + 2v')] - \exp[-j\pi\eta'(\Delta v - 2v')]}{2j\pi\eta'} \right) \exp[j2\pi k(\xi - \xi')] \mathrm{d}\xi' \mathrm{d}\eta' \right|^2, \quad (6.13)$$

where ξ' and η' are the dummy integration variables. Computing this integral over ξ' and η' results in

$$I(\xi,\eta) \propto \left| \frac{1}{4\pi^2} \left(E_i[-\frac{j\pi}{2}(2\eta - D)(\Delta v - 2v')] - E_i[-\frac{j\pi}{2}(2\eta + D)(\Delta v - 2v')] \right.\right.$$
$$\left. -E_i[\frac{j\pi}{2}(2\eta - D)(\Delta v + 2v')] + E_i[\frac{j\pi}{2}(2\eta + D)(\Delta v + 2v')] \right)$$
$$\times \left(E_i[-\frac{j\pi}{2}(2\xi - D)(\Delta u + 2k - 2u')] - E_i[-\frac{j\pi}{2}(2\xi + D)(\Delta u + 2k - 2u')] \right.$$
$$\left. \left. -E_i[\frac{j\pi}{2}(2\xi - D)(\Delta u - 2k + 2u')] + E_i[\frac{j\pi}{2}(2\xi + D)(\Delta u - 2k + 2u')] \right) \right|^2, \quad (6.14)$$

where $E_i(x)$ is the Exponential Integral Function defined by [88]

$$E_i(x) = -\int_{-x}^{\infty} \frac{\exp[-t]}{t} \mathrm{d}t. \quad (6.15)$$

The significance of Eq. (6.14) is best seen by plotting the aperture image intensity versus the constituent variables. Since the results depend on the ratio of the diffraction-limited spot relative to the lenslet size, the lenslet is hereafter defined to be of unit dimension, $\Delta u = \Delta v = 1$. Changing D, the aperture dimension, is then used to vary the size of the diffraction-limited spot relative to this standard lenslet size.

Firstly, the intensity is plotted versus ξ, the coordinate in the conjugate aperture plane, in Fig. 6.5 for four different lenslet positions (u'=0, 1.49, 1.51 and 2) with the other variables held constant (D=10, v'=0, k=2 and η=0). These lenslet positions correspond to different relative relationships between the diffraction-limited spot and the considered lenslet. When the spot falls wholly inside the lenslet, then the aperture image intensity is approximately constant across the aperture with some ringing inside the aperture. When the spot falls outside the lenslet, the aperture image intensity is approximately zero with some ringing at the edges of the re-imaged aperture. These two cases are less useful for wavefront sensing because although they indicate a band of possible slopes, they cannot convey the exact position of the spot in the focal plane and hence slope in the aperture. However, when

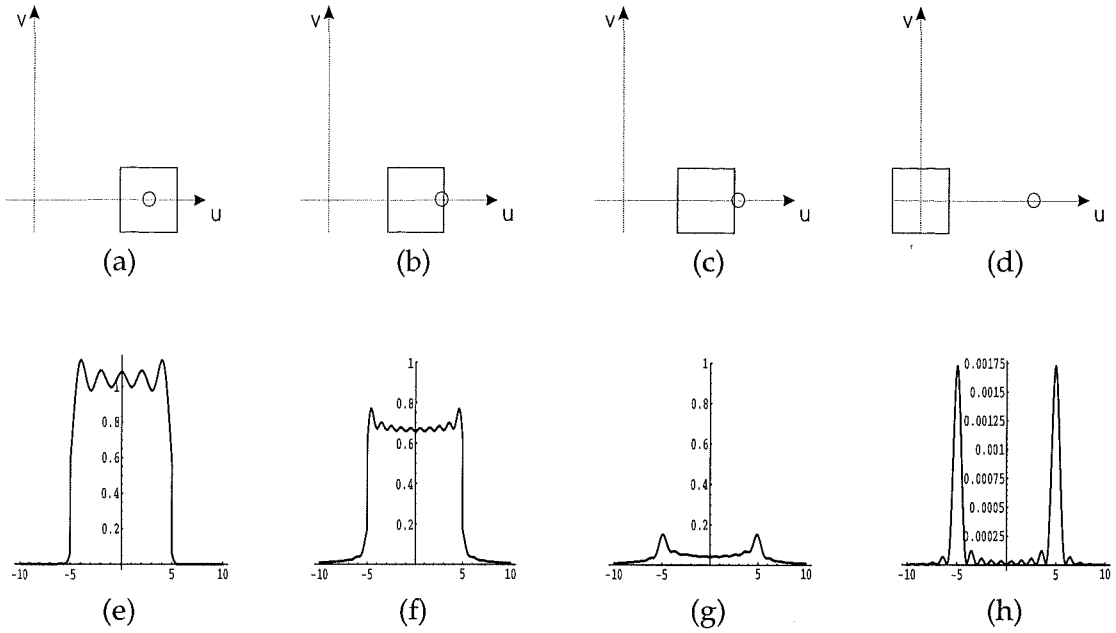

Figure 6.5 The images of the aperture for different relative positions of the lenslet and the spot in the focal plane. Assuming a wavefront tilt of magnitude k=2 and the lenslet positioned in the focal plane at (a) u'=2 such that the diffraction-limited spot falls on the centre of this lenslet, (b) u'=1.51 such that the spot falls on the edge of this lenslet with the majority of the spot falling inside this lenslet, (c) u'=1.49 such that the spot falls on the edge of the lenslet with the majority of the spot falling outside the lenslet, and (d) u'=0 such that the diffraction-limited spot falls outside this lenslet. (e)-(h) are the plots of the aperture image intensity in the conjugate aperture plane over the ξ dimension for (a)-(d) respectively.

the spot falls on the edge of the lenslet then an approximately linear relationship exists between the intensity at a point in the re-imaged aperture and the position of the spot in the focal plane as seen in Fig. 6.5(f) and (g).

The plot of image intensity versus the wavefront tilt, k, from Eq. (6.14) shows how a lenslet acts as a filter on the slopes. In Fig. 6.6 the size of the spot is reduced relative to the lenslet width by increasing D the aperture dimension. The centre of the passband of the slope filter is equal to the lenslet centre, u', and the passband width equal to the width of the lenslet, Δu, in the considered direction. When the slope of the wavefront at a given point (ξ, η) lies in the passband of the slope filter defined by the lenslet, then the intensity at the same point in the re-imaged aperture is approximately constant. If the slope at this given point (ξ, η) lies outside the passband of the slope filter of the lenslet, then the intensity at the same point in the re-imaged aperture is approximately zero. Between these two extremes there exists a region where there is an approximately linear relationship between the slope, k, and the measured intensity. The width of this cutoff region is determined by the width of the spot in the focal plane.

The largest linear region for slope estimation, shown in Fig. 6.6(d), occurs when D=2.25

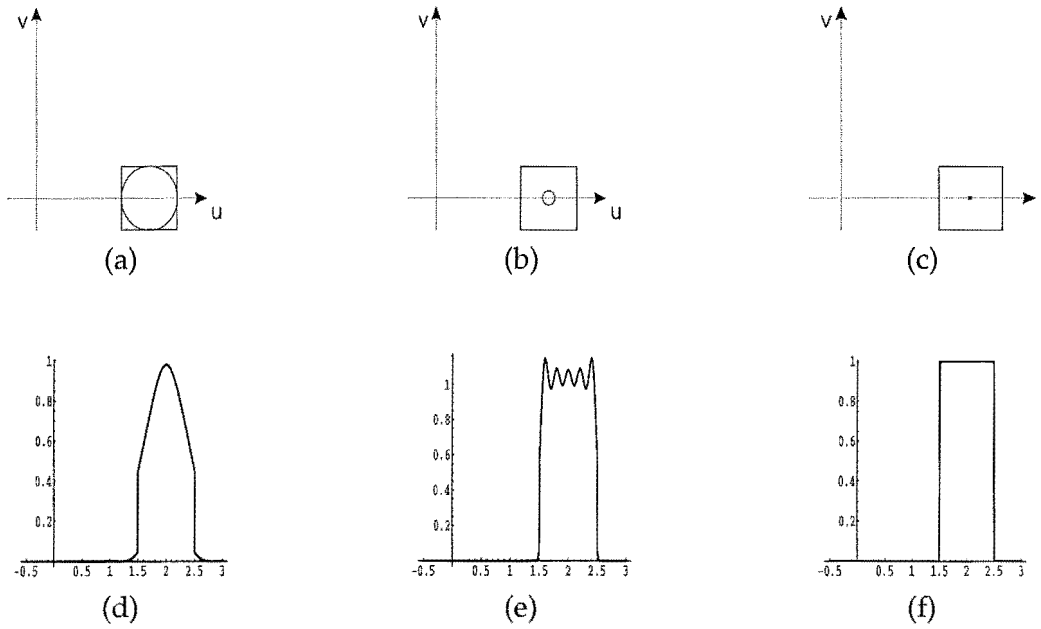

Figure 6.6 The effects on the aperture image of the relative size of the lenslet and focused spot in the focal plane. Assuming a lenslet centred at u'=2 and width Δu=1 for (a) fixed aperture size of D=2.25, and (b) fixed aperture size of D=10, and (c) an infinite sized aperture (D=∞). (d)-(f) are the plots of the aperture image intensity, $I(\xi, \eta)$, versus the magnitude of the wavefront tilt, k, for the cases described by (a)-(c) respectively.

which produces a spot the same width as the lenslet. When the spot is smaller than the lenslet, such as Fig. 6.6(e) with an aperture of D=10, there is a region, which can be considered as the passband of the filter, where the slope can only be determined to within a finite range. It can be seen from Fig. 6.6(f) that as the size of the aperture is increased in the limit to ∞, the filtering effect on the slopes tends towards an ideal filter in that there is no ringing in either the passband or at the edges of the stopband of the slopes. This case is consistent with the geometrical optics analysis, since when the aperture becomes large the diffraction-limited spot effectively becomes a point, implying the 'brick-wall' filter response as seen in Fig. 6.6(f).

The analysis presented so far and displayed in Fig.s 6.5 and 6.6 has assumed the use of narrowband light, which is the worst case scenario for operation of this wavefront sensor. In practice, wavefront sensors are operated in broadband light to utilise all the available photons. This has the effect of reducing the ringing in the re-imaged aperture of Fig. 6.5 and within the passband of the filters seen in Fig. 6.6.

Subdividing at the focal plane also affects the accuracy with which the slope over a region in the aperture can be estimated. As noted earlier, as the amount of subdivision in the focal plane is increased, ie the lenslets are made smaller, the image of the aperture becomes more blurred and the smallest region over which an independent slope in the aperture can be effectively estimated becomes larger. Hence as the lenslet size decreases, the size of the

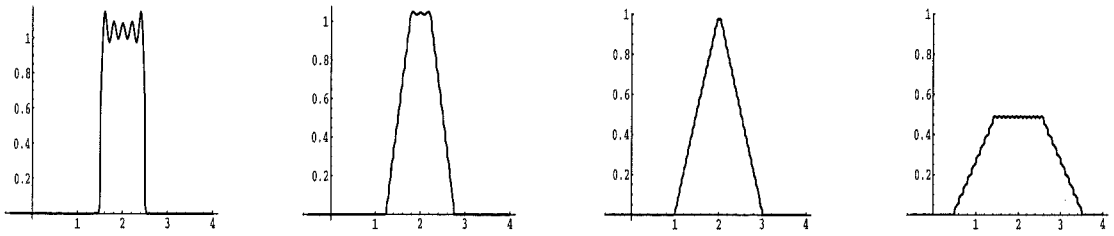

Figure 6.7 The slopes filter effect, $I(\xi,\eta)$ versus k, the magnitude of the wavefront tilt, with the lenslet centred at u'=2 and lenslet width Δu=1 using a discrete summation of the aperture images for (a) the unmodulated case, (b) modulation of width $\frac{\Delta u}{2}$, (c) modulation of width Δu, and (d) modulation of width $2\Delta u$.

pixels in the conjugate aperture plane should be increased to minimise the read noise and increase the number of photons per pixel. This increases the SNR over each region in the aperture, and consequently the slope measurement error and phase difference error over each region in the aperture decrease. Thus decreasing the lenslet size in the focal plane decreases the spatial resolution attainable in the aperture but improves the accuracy with which these estimates can be made. This is the inverse result to that of the Shack-Hartmann and results from the subdivision of the complex field being performed at the focal plane rather than at the aperture plane.

6.2.2 Modulation of the lenslet

It is desirable to have a linear relationship between the measurements and the wavefront slope over as wide a range of wavefront slopes as possible. An increase in the linear range of the lenslet array at the focal plane can be attained by modulation of the position of the lenslet array in the focal plane. Consider the effect of moving a single lenslet centred at (u',v') in the focal plane over a fixed path during the exposure time in the measurement plane. This increases the width of the linear regions in the slope filter. This modulation of the lenslet is similar to the modulation of the pyramid sensor [11]. Thus the image formed from moving the lenslet in the focal plane is an integral over u' and v', the nominal centre of the lenslet, of Eq. (6.11). For a linear modulation of width w about the nominal centre of the lenslet u' in the u dimension only, the observed aperture image is given by the continuous summation of the aperture images over all the instantaneous lenslet positions, u'', of the modulation path

$$I(\xi,\eta) \propto \int_{u'-\frac{w}{2}}^{u'+\frac{w}{2}} \Big| \Delta u \,\mathrm{sinc}(\pi\xi\Delta u)\, \exp[j2\pi\xi u''] \,\Delta v \,\mathrm{sinc}(\pi\eta\Delta v)\, \exp[j2\pi\eta v'] \odot P(\xi,\eta)\exp[j\phi(\xi,\eta)] \Big|^2 \mathrm{d}u''. \qquad (6.16)$$

The integral of Eq. (6.16) is not mathematically tractable, but can be approximated by a discrete summation of the aperture images over the modulation path. The slope filters for a variety of modulation widths with this approximation are plotted in Fig. 6.7. The modulation of the lenslet changes the properties of the slopes filter, the intensity at a particular point in the re-imaged aperture (ξ, η) versus k the wavefront slope. The slope filter for a modulated lenslet (Fig. 6.7(b), (c) and(d)) has a larger linear cutoff region between the pass and stop bands compared to the unmodulated case (Fig. 6.7(a)). The optimal case is given in Fig. 6.7(c) where the passband has zero width and there is a linear cutoff region equal to the modulation width. However, as the modulation width increases, the slope in the cutoff region decreases which signifies a decrease in the sensitivity of the slope measurement.

In the unmodulated case, the spatial resolution achievable in the aperture is determined by the width of the sinc function which is convolved with the complex field in the aperture. The width of this sinc function is determined by the width of the lenslet. The modulated aperture image of Eq. (6.16) can be thought of as the summation of the aperture images arising from all the possible lenslet positions along the modulation path. Since each of these instantaneous aperture images has a spatial resolution limited by the width of the lenslet, their summation, the modulated aperture image, also has a spatial resolution determined by the width of the unmodulated lenslet. The modulation of the lenslets thus does not affect the spatial resolution of the slope measurements in the aperture.

Each modulation cycle of the lenslet array needs to be completed while the atmosphere is essentially frozen. For this condition to hold, the modulation frequency of the lenslet array needs to be greater than the Greenwood frequency. The effects of modulation on the sensitivity of the wavefront sensor are discussed in Section 6.3.

6.3 Array of lenslets

The general case of an array of $M \times N$ square lenslets placed in the focal plane such that $\Delta u = \Delta v = d$ is now considered. The displacement of the central lenslet from the origin in the u and v directions is denoted by (δ_u, δ_v). The IFT of the $(m,n)^{th}$ lenslet, where $m = -M/2 + 1 \ldots M/2$ and $n = -N/2 + 1 \ldots N/2$, is

$$H_{m,n}(\xi,\eta) = \mathcal{F}^{-1}\Big[h_{m,n}(u,v)\Big] = \int_{(n-\frac{1}{2})d-\delta_v}^{(n+\frac{1}{2})d-\delta_v} \int_{(m-\frac{1}{2})d-\delta_u}^{(m+\frac{1}{2})d-\delta_u} \exp[j2\pi(u\xi + v\eta)]\mathrm{d}u\mathrm{d}v, \quad (6.17)$$

and by performing this integration can be shown to be

$$H_{m,n}(\xi,\eta) = d^2\ \mathrm{sinc}(\xi d)\exp\Big[j2\pi\xi(md-\delta_u)\Big]\mathrm{sinc}(\eta d)\exp\Big[j2\pi\eta(nd-\delta_v)\Big]. \quad (6.18)$$

By substituting Eq. (6.18) into Eq. (6.8), the general form of the aperture image formed by the $(m,n)^{th}$ lenslet of a lenslet array in the focal plane is

$$I_{m,n}(\xi,\eta) = \Bigg| d^2 \operatorname{sinc}(\xi d) \exp\Big[j2\pi\xi(md-\delta_u)\Big] \operatorname{sinc}(\eta d) \exp\Big[j2\pi\eta(nd-\delta_v)\Big] \odot P(\xi,\eta)\exp[j\phi(\xi,\eta)]\Bigg|^2 . \tag{6.19}$$

As noted in Appendix A, a conventional lenslet array would not adequately separate the images formed on the detector. However, despite some technical difficulties ensuring the images of the aperture do not overlap is feasible and is not discussed further here.

6.3.1 Reconstruction from aperture images

The estimates of the partial derivatives of the wavefront aberration with respect to ξ and η for an $M \times N$ array of lenslets are given by

$$\frac{\partial\phi(\xi,\eta)}{\partial\xi} \propto \left[\sum_{m=-M/2+1}^{M/2}\sum_{n=-N/2+1}^{N/2}(md-\delta_u)I_{m,n}(\xi,\eta)\right] \Bigg/ \left[\sum_{m=-M/2+1}^{M/2}\sum_{n=-N/2+1}^{N/2} I_{m,n}(\xi,\eta)\right] \tag{6.20}$$

$$\frac{\partial\phi(\xi,\eta)}{\partial\eta} \propto \left[\sum_{m=-M/2+1}^{M/2}\sum_{n=-N/2+1}^{N/2}(nd-\delta_v)I_{m,n}(\xi,\eta)\right] \Bigg/ \left[\sum_{m=-M/2+1}^{M/2}\sum_{n=-N/2+1}^{N/2} I_{m,n}(\xi,\eta)\right] \tag{6.21}$$

It is important to note here that these two gradient formulae are the generalisation of those derived by Ragazzoni [11] for the pyramid wavefront sensor, Eq.s (4.10) and (4.11). The gradient components for the pyramid can be obtained from Eq.s (6.20) and (6.21) by setting N and M as 2 and δ_u and δ_v as $\frac{d}{2}$.

6.3.2 Array of lenslets without modulation

The slope estimation curves for an unmodulated lenslet array when the lenslet array size is varied relative to the constant spot size are shown in Fig. 6.8. As the lenslets in the array are made smaller and approach the spot size, the tilt estimation curves, Fig. 6.8, become more linear which is beneficial for an open loop system. However, as noted in Section 6.2, the spatial resolution in the aperture gets worse as the lenslets are made smaller, whilst the slope accuracy over each region in the aperture improves as the lenslets are made smaller. To summarise the lenslet array operation without modulation, Fig. 6.8(a)

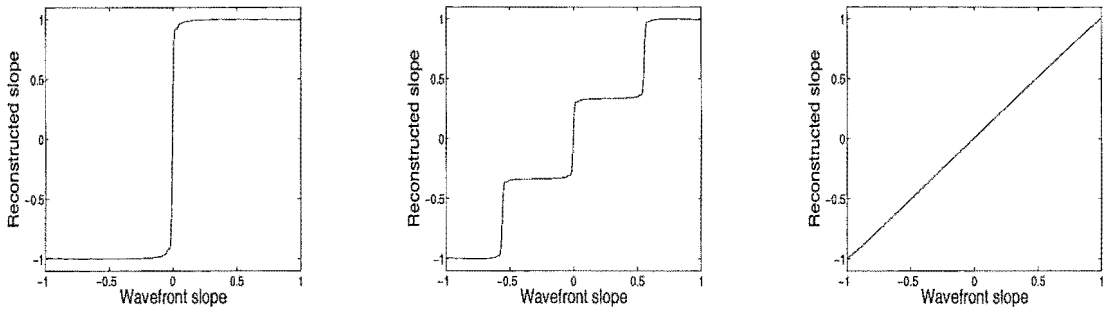

Figure 6.8 The normalised global tilt characteristics for a lenslet array in the focal plane with (a) 2×2 array of lenslets such that the spot size is less than the lenslet width, (b) 4×4 array of lenslets such that the spot size is less than the lenslet width, and (c) 64×64 array of lenslets such that the spot size is equal to the lenslet width.

and (b) are desirable since they correspond to a high resolution for the wavefront slope in the aperture and a high sensitivity. In contrast, Fig. 6.8(c) is desirable because of the low slope measurement error for each region in the aperture, and in open loop due to the large range of the linear relationship between the aperture images and the slopes. However, as shown in Appendix A, Fig. 6.8(c) corresponds to a poor resolution in the aperture slope measurement.

6.3.3 Array of lenslets with modulation

As discussed in Section 6.2.2, modulation can be used with a lenslet array to increase the linear range of operation. The global tilt characteristics for a 4×4 array symmetric about the axes in the focal plane, ie $(\delta_u, \delta_v) = (\frac{d}{2}, \frac{d}{2})$, with modulation widths of zero, $\frac{d}{2}$, d and $2d$ are shown in Fig. 6.9. When the modulation width is less than the lenslet width, there remain dead regions where the slope cannot be determined exactly. Linear performance over all wavefront slopes is achieved when the modulation width is greater than or equal to the width of the lenslet, although Fig. 6.9(d) indicates that there is little to be gained by making the modulation width greater than the lenslet width. The increased linear range is desirable in open loop and before closing the loop in a closed loop system. When the loop is successfully closed, a smaller linear range is sufficient. The modulation can then be reduced to improve the sensitivity of the sensor, and hence reduce the phase difference error within each region in the aperture.

6.3.4 Linear operation

It is possible to achieve a large linear range in two possible ways with a lenslet array at the focal plane. These are either to have the lenslet size the same as the spot size, or to modulate the array such that the modulation width is the same as the lenslet width. The modulated array, however, offers two significant advantages. Firstly, if the array is modulated then

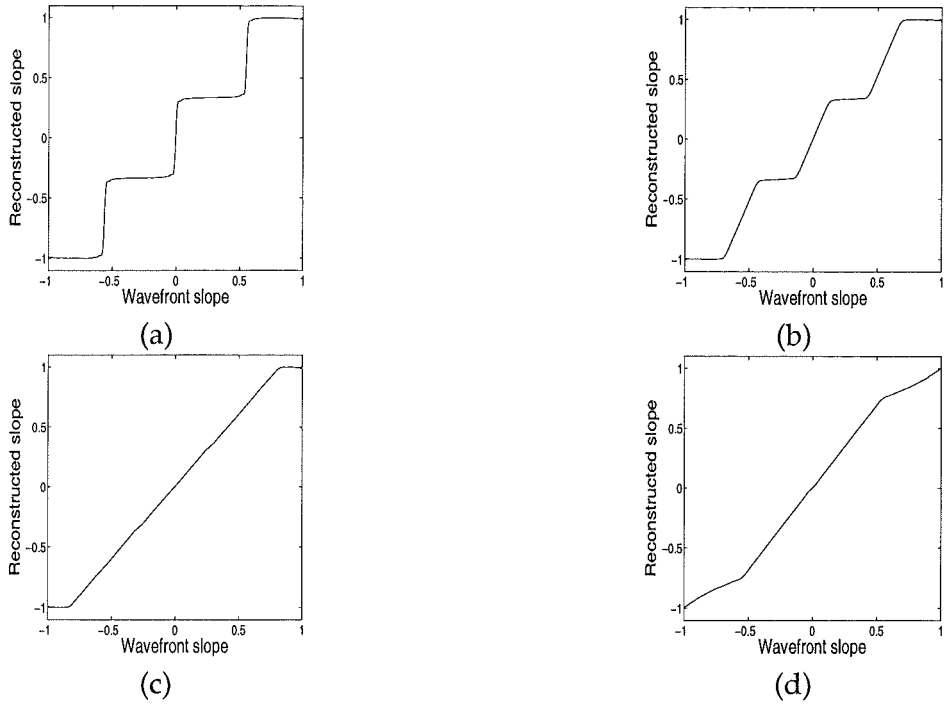

Figure 6.9 The normalised global tilt characteristics for a 4×4 lenslet array in the focal plane where the modulation width of the array is (a) zero, (b) half the width of the lenslet, (c) equal to the width of the lenslet, and (d) twice the width of the lenslet.

larger lenslets can be used and therefore a better spatial resolution for slope estimates in the aperture can be obtained. Thus the optimal case in this class is the 2×2 arrangement of lenslets, which is the equivalent of the pyramid sensor. Secondly, the modulated case does not require the spot size to be known accurately for implementation. The non-modulated array offers the advantage that no mechanical modulation is required.

6.3.5 Duality of focal plane subdivision with the Shack-Hartmann

The duality between the formation of the slope estimates from the images when subdividing in the focal plane and with the Shack-Hartmann sensor should also be noted. For the Shack-Hartmann sensor, the slope over a region (lenslet) is given by the centroid of the corresponding image. For the lenslet array at the focal plane, the slope estimate for each region (pixel) is given as a centroid of the aperture images for the corresponding region (pixel). Comparing the formulae for the slope estimates from subdivision at the focal plane (Eq.s (6.20) and (6.21)) with the traditional centroid estimator for the Shack-Hartmann sensor (Eq.s (4.4) and (4.4)), it can be seen that increasing the number of lenslets in the array in the focal plane is analogous to increasing the number of pixels used to detect each image in the Shack-Hartmann sensor. Conversely, the number of pixels used to re-image the aperture from focal plane subdivision is analogous to the number of lenslets used in the Shack-Hartmann sensor.

In the Shack-Hartmann sensor, the optimal configuration to minimise the noise is the quad-cell, which consists of 2×2 pixels per lenslet. The dual of the quad-cell is the 2×2 lenslet array at the focal plane, which is equivalent to the pyramid sensor configuration. Thus the pyramid sensor configuration is the optimal configuration for subdivision at the focal plane for the same reason, noise reduction, that the quad-cell is optimal for subdivision at the aperture plane.

6.4 Simulation results

In this section, the Shack-Hartmann and lenslet array at the focal plane are simulated in the presence of atmospheric turbulence in open loop. For both sensors, the Zernike weights, a, are estimated with Eq. (4.21), which is reproduced here,

$$\hat{a} = (C^{-1} + \Theta^T N^{-1} \Theta)^{-1} \Theta^T N^{-1} m, \tag{6.22}$$

where m are the slope estimates, Θ is the interaction matrix, and C and N are the covariance matrices of the atmosphere and noise respectively.

The atmospheric phase screens are generated using the method of Harding *et al.*, which is discussed in Section 3.2.5. The simulations are run at two levels of atmospheric turbulence: D/r_0= 8 and 12. The circular phase screens of dimension 64 × 64 pixels are placed inside 128 × 128 arrays of zeros before Fourier transforming to form the complex field at the focal plane. The signal level of the speckle images investigated is 1e4 photons per frame. The detector is assumed to be ideal, that is no read noise is added. In both cases the Bayesian least squares estimates are made using the first 100 Zernike polynomials. The Mean-Squared-Error (MSE) (rad^2) is averaged over 1000 phase screens for each sized lenslet array. The noise covariance matrices for the Shack-Hartmann sensor are those given by Welsh *et al.* [89] and the identity matrix is used for the focal plane array. The lenslet arrays at the focal plane are modulated with a diamond path of modulation width equal to the width of the lenslets in the array as outlined in Section 6.3.

The simulation results in Fig. 6.10 do show the expected trade-off between spatial resolution and slope accuracy predicted in Section 6.3 for the lenslet array at both the aperture and focal planes. For the Shack-Hartmann, the wavefront estimate initially improves as the spatial resolution improves, but as the number of lenslets increases past the optimum (6 × 6 lenslets for both D/r_0=8 and 12) the estimate becomes worse due to the degraded slope accuracy. For subdivision at the focal plane without modulation, the wavefront estimate initially improves as the number of lenslets increases due to the improved slope accuracy and increased linear range, but after the minimum (13 × 13 lenslets for D/r_0=8 and 7 × 7 lenslets for D/r_0=12) the estimate becomes worse due to the degradation in spa-

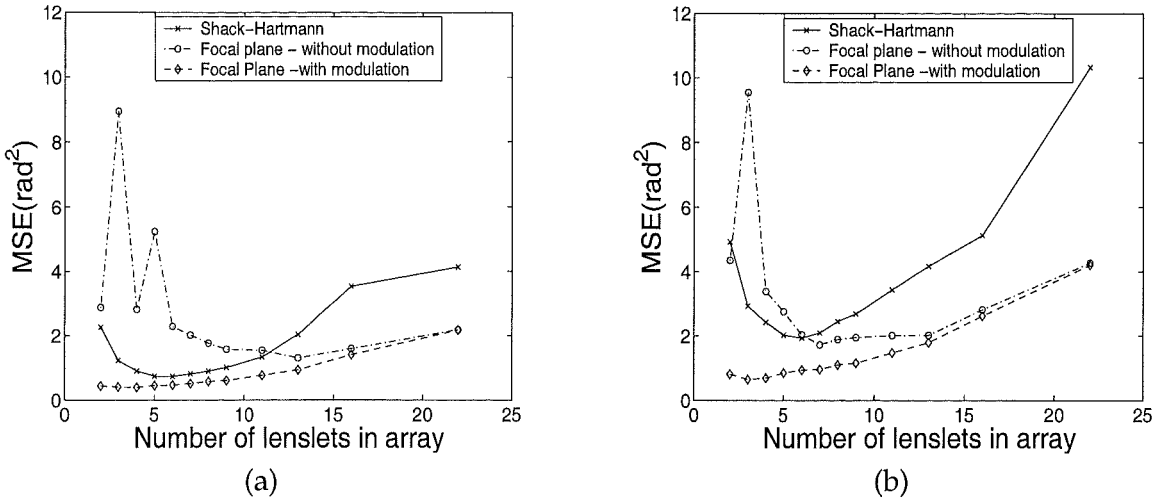

Figure 6.10 Comparison of the Mean-Squared-Error (rad^2) for different sized lenslet arrays at the aperture plane (Shack-Hartmann), and the focal plane with and without modulation, in turbulence of severity (a) D/r_0=8, and (b) D/r_0=12.

tial resolution of the slope estimates. The peaks in the focal plane subdivision without modulation curves (at 3×3 and 5×5 lenslets for D/r_0=8 and 3×3 lenslets for D/r_0=12) occur for these odd-sized arrays since the complex field in the focal plane becomes saturated in the central lenslet.

Without modulation, the performance of subdividing either the aperture or focal plane with a lenslet array is similar. At D/r_0=8, the Shack-Hartmann provides a better wavefront estimate than subdivision at the focal plane when there are fewer than 11×11 lenslets in the array. When there are more than this number of lenslets, subdivision at the focal plane is superior. At the more severe level of turbulence, D/r_0=12, this crossover point occurs when there are 6×6 lenslets in the array. This crossover point is lower at the higher D/r_0 level because the higher D/r_0 level causes the spot in the focal plane to become larger. The enlarged spot size causes the tip/tilt curve to have an increased linear range.

At both simulated levels of turbulence, subdivision at the focal plane employed in conjunction with modulation of the lenslets is superior to subdivision at either the aperture or focal planes alone, for all lenslet array sizes. The optimal arrangement for subdivision at the focal plane in open loop is with the minimum number of lenslets (four) since this provides the best spatial resolution whilst retaining a large linear range.

It is important to note that the simulation results presented in this chapter were obtained with ideal detectors, ie there is no read noise. Current detectors are, however, limited by read noise. Read noise is dependent on the number of pixels used in the sensor. If the number of pixels used to capture the image for the Shack-Hartmann sensor is the same as the number of lenslets used at the focal plane, and the number of pixels used to re-image

the aperture with the lenslet array at the focal plane is the same as the number of lenslets in the Shack-Hartmann sensor, then the total number of pixels is conserved, and this is the case for the simulations presented in this chapter. Consequently, if the ratio of the pixel size to lenslet size is the same in both sensors, it would appear that the read noise does not affect the relationships developed in this chapter between the two sensors.

6.5 Conclusion

In this chapter, a wavefront sensor has been derived from a lenslet array placed in the focal plane of the telescope. Like the pyramid sensor, this sensor operates by subdividing the complex field in the focal plane. As with the lenslet array placed in the aperture plane of a telescope, the Shack-Hartmann wavefront sensor, when the lenslet array is placed in the focal plane, there exists a trade-off between the slope accuracy and spatial resolution obtainable. In both cases this trade-off is determined by the physical size of the lenslets in the array. For the Shack-Hartmann sensor, as the lenslet size increases the spatial resolution gets worse and the slope accuracy improves. Whereas when subdividing at the focal plane, as the lenslet size increases the spatial resolution improves and the slope accuracy is degraded. This inverse relationship is due to the underlying Fourier transform relationship between the aperture and focal planes.

The two wavefront sensors are intrinsically linked; both subdivide one of a Fourier pair resulting in a trade-off between spatial resolution and slope accuracy, and both use a centroid operator to form slope estimates. The lenslet array at the focal plane, however, offers the advantage that modulation can increase the linear range of the system with respect to tilt estimation. In a closed loop system, the modulation can then be reduced as the adaptive optics start to compensate the turbulence in order to increase the sensitivity of the system.

Simulation results show that the best configuration of subdivision at the focal plane is with a 2×2 array with modulation, an arrangement equivalent to pyramid sensing. Instead of viewing the Shack-Hartmann and pyramid sensors as separate techniques, it should be noted that a duality exists between the sensors, based on the subdivision of a wavefront and then propagation of the subdivided sections.

Chapter 7

N-sided Wavefront Sensors

7.1 Introduction

The pyramid wavefront sensor, which is reviewed in Section 4.1.4, subdivides the complex field at the origin of the focal plane into quadrants with a four sided glass prism. In Chapter 6, the pyramid sensor is generalised by placing a lenslet array at the focal plane to subdivide the focal plane into an array of square sections. Another generalisation of the pyramid sensor is to subdivide the complex field in the focal plane into N equal segments at the origin of the focal plane. This class of wavefront sensor, of which the pyramid sensor is one element, is considered in this chapter. This spatial filtering of the focal plane can be realised by either an N-sided prism or lenslets of the equivalent geometry placed in the focal plane.

A three sided prism provides the minimum number of images needed to resolve the slope in two orthogonal directions. The three-sided case therefore has the advantage that it requires the least number of detector pixels to capture the aperture images. Conversely, if the number of segments, N, is increased in the limit $N \to \infty$, then the novel cone wavefront sensor is derived. The cone sensor is the member of the class that subdivides the wavefront the most, and hence can provide the most information about the wavefront aberration.

Typically the wavefront is reconstructed from the pyramid sensor measurements by forming slope estimates in the two Cartesian orthogonal directions [11, 49–52]. These slope estimates are formed as linear combinations of the aperture images from simple geometric considerations; the slope in the x direction is formed from the sum of the two images in the left half plane subtracted from the sum of the two images in the right half plane. Thus in the pyramid sensor the two slope estimates are attained by combining four pixel measurements. Some information contained in the aperture images is therefore lost.

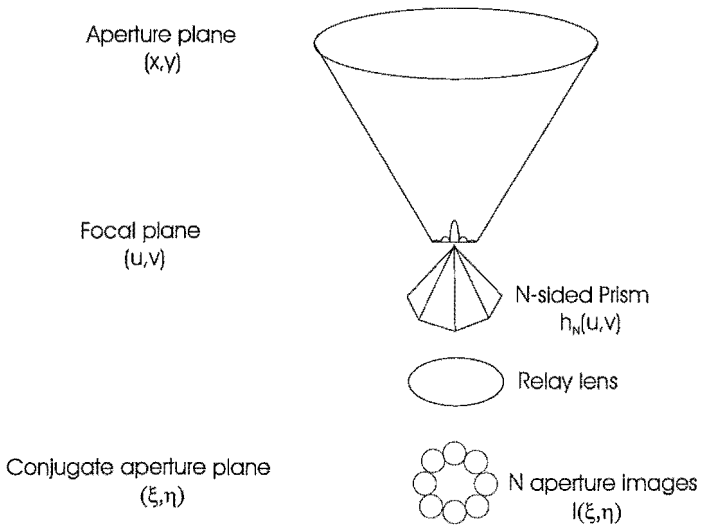

Figure 7.1 The layout for an N-sided prism wavefront sensor. The prism subdivides the complex field in the focal plane, with the sections passed through a relay lens to form N aperture images at the conjugate aperture plane.

An alternative approach, which uses all the available information directly, is to fit a set of Zernike polynomials directly to the observed measurements. Simulation results are presented in this chapter to show that reconstructing the wavefront directly from the measurements gives a better wavefront estimate than reconstructing from the slope estimates. This result leads on to the work in Chapter 8, which investigates the estimation of the wavefront phase directly from the aperture images with the use of an iterative phase retrieval algorithm.

This chapter is structured as follows. Section 7.2 introduces the mathematical background for this class of wavefront sensors. The algorithms for reconstructing the wavefront from the measurements are discussed in Section 7.3. Simulation results for both reconstruction methods in the presence of atmospheric turbulence are presented in Section 7.4. Conclusions for the work done in this chapter are drawn in Section 7.5.

7.2 Mathematical background

A prism in the focal plane subdivides the light in the focal plane. This is described mathematically as a spatial filter $h_N(u,v)$, where N is the number of sides of the prism. The presence of the relay lens after the prism in the optical path reverses the Fourier transform relationship to produce N images in the conjugate aperture plane, described by coordinates (ξ,η). The complex field in the conjugate plane is thus a low-pass filtered image of the aperture. The N-sided wavefront sensing scheme is depicted in Fig. 7.1.

The resulting aperture images in the conjugate aperture plane, $I(\xi,\eta)$, are given by Eq.

(6.8), which is repeated here

$$I(\xi,\eta) \propto \left| H_N(\xi,\eta) \odot P(\xi,\eta)\exp[j\phi(\xi,\eta)] \right|^2 . \tag{7.1}$$

The aperture images formed from spatial filtering in the focal plane are thus the convolution of the complex amplitude at the aperture with the IFT of the spatial filter.

As with the lenslet arrays in Chapter 6, modulation can be employed to increase the linear range of operation for all wavefront sensors in this class. The width of the linear range of operation is equal to the width of the modulation path, w [52]. The modulation of the prism is a physical shift of the prism (or equivalently of the light with a tip/tilt mirror) in the focal plane. The instantaneous spatial filter caused by a shift of (u'', v'') is denoted by $h_N(u-u'', v-v'')$. The IFT of the shifted spatial filter of a prism is then $H_N(\xi,\eta)\exp[j2\pi\xi u'']\exp[j2\pi\eta v'']$. The aperture images resulting from modulation are the continuous summation of all the aperture images formed over the modulation path

$$I(\xi,\eta) \propto \int\int \left| H_N(\xi,\eta)\exp[j2\pi\xi u'']\exp[j2\pi\eta v''] \odot P(\xi,\eta)\exp[\phi(\xi,\eta)] \right|^2 \mathrm{d}u''\mathrm{d}v''. \tag{7.2}$$

7.2.1 Fourier analysis of the Foucault test

The Foucault test represents the simplest subdivision of the complex field in the focal plane and can be considered the basis of all the wavefront sensors considered in this chapter. The spatial filters for the planes to the left, $h_l(u)$, and right $h_r(u)$, of the knife edge considered individually are [53]

$$\begin{aligned} h_l(u) &= \frac{1}{2}\Big(-\operatorname{sgn}(u) + 1 \Big)\exp[j2\pi bu] \\ h_r(u) &= \frac{1}{2}\Big(\operatorname{sgn}(u) + 1 \Big)\exp[-j2\pi bu], \end{aligned} \tag{7.3}$$

where the $\exp[j2\pi bu]$ term is the delay effect of the slope of the prism face and b is the slope of the prism face. The IFTs of the two spatial filters defined by Eq. (7.3) can be calculated using the definition of the IFT as

$$\begin{aligned} H_l(\xi) &= \frac{1}{j2\pi(\xi-b)} + \frac{1}{2}\delta(\xi-b) \\ H_r(\xi) &= \frac{-1}{j2\pi(\xi+b)} + \frac{1}{2}\delta(\xi+b), \end{aligned} \tag{7.4}$$

where δ is the delta function defined in Section 2.2. The aperture images formed from performing the Foucault test in the left and right half planes respectively are given by

substituting Eq. (7.4) into Eq. (7.1) yielding [53]

$$\begin{aligned} I_l(\xi,\eta) &= \left|\frac{1}{2}\delta(\xi-b)\odot P(\xi,\eta)\exp[j\phi(\xi,\eta)]+\frac{1}{j2\pi(\xi-b)}\odot P(\xi,\eta)\exp[j\phi(\xi,\eta)]\right|^2 \\ I_r(\xi,\eta) &= \left|\frac{1}{2}\delta(\xi+b)\odot P(\xi,\eta)\exp[j\phi(\xi,\eta)]+\frac{-1}{j2\pi(\xi+b)}\odot P(\xi,\eta)\exp[j\phi(\xi,\eta)]\right|^2 \end{aligned} \quad (7.5)$$

By applying the Hilbert transform and invoking the sifting property of the convolution operator with the δ function, the aperture images can be further simplified to

$$\begin{aligned} I_l(\xi,\eta) &= \left|\frac{1}{2}P(\xi-b,\eta)\exp[j\phi(\xi-b,\eta)]+\frac{1}{2}H\left\{jP(\xi-b,\eta)\exp[j\phi(\xi-b,\eta)\right\}\right|^2 \\ I_r(\xi,\eta) &= \left|\frac{1}{2}P(\xi+b,\eta)\exp[j\phi(\xi+b,\eta)]-\frac{1}{2}H\left\{jP(\xi+b,\eta)\exp[j\phi(\xi+b,\eta)\right\}\right|^2 \end{aligned} \quad (7.6)$$

The image formed in the left half plane is the squared sum of the wavefront aberration and the Hilbert transform of the aberration multiplied by j. Conversely, the image formed in the right half plane is the squared difference of the wavefront aberration and the Hilbert transform of the aberration multiplied by j.

7.2.2 Subdivision into N segments at the origin of the focal plane

The effect of subdividing the focal plane with a prism can be modelled by a filter having a piece-wise linear phase delay and a constant magnitude. If the apex is considered to be centred at the origin and have zero phase delay, then the spatial filter, $h_4(u,v)$, for the pyramid is

$$h_4(u,v)=\exp[j2\pi b(|u|+|v|)], \quad (7.7)$$

where b is again the slope of the pyramid face.

The IFT of Eq. (7.7) can be calculated by finding the IFTs of the four quadrants individually and adding the results to give

$$H_4(\xi,\eta)=\frac{b^2}{\pi^2(b-\xi)(b+\xi)(b-\eta)(b+\eta)}. \quad (7.8)$$

Clearly, $H_4(\xi,\eta)$ tends to ∞ at $\xi=\pm b$ and $\eta=\pm b$. These singularities are caused by the edges of the pyramid which produce discontinuities in the first derivative of the phase. The images formed from the pyramid are given by substituting Eq. (7.8) into Eq. (7.1),

$$I(\xi,\eta)=\left|\frac{b^2}{\pi^2(b-\xi)(b+\xi)(b-\eta)(b+\eta)}\odot P(\xi,\eta)\exp[j\phi(\xi,\eta)]\right|^2. \quad (7.9)$$

This results in four images of the aperture centred at the singularities given by $(\xi,\eta) = (-b,b),(b,b),(b,-b)$ and $(-b,-b)$. The generalisation of this result is that the N aperture images formed from an N-sided prism are positioned at the vertices of an N-sided regular polygon.

The form of the aperture images when the pyramid is modulated are given by substituting Eq. (7.9) into Eq. (7.2)

$$I(\xi,\eta) \propto \int\int \left| \frac{b^2}{\pi^2(b-\xi)(b+\xi)(b-\eta)(b+\eta)} \exp[j2\pi\xi u''] \exp[j2\pi\eta v''] \right. \\ \left. \odot P(\xi,\eta) \exp[j\phi(\xi,\eta)] \right|^2 \mathrm{d}u''\mathrm{d}v'', \quad (7.10)$$

where u'' and v'' are the instantaneous position of the pyramid vertex in the modulation path.

The spatial filters of the prism sensors with an even number of sides can be described mathematically by the sum of the magnitude of linear combinations of u and v. For example, the eight sided prism is defined by

$$h_8(u,v) = \exp[j2\pi b(|u+v| + |v-u| + |u| + |v|)]. \quad (7.11)$$

The phase filters for the prisms with odd numbers of sides need to be described by piecewise functions. For example, the spatial filter for the three sided case is defined by

$$h_3(u,v) = \begin{cases} \exp[j2\pi b(-2u)] & -\frac{\pi}{3} < \arctan(u/v) < \frac{\pi}{3} \\ \exp[j2\pi b(u-\sqrt{3}v)] & \frac{\pi}{3} < \arctan(u/v) < \pi \\ \exp[j2\pi b(u+\sqrt{3}v)] & \text{otherwise.} \end{cases}$$

In order to reduce the physical size of the detector required to capture the aperture images, the slope of the prism face, b, should be chosen such that the resulting aperture images are as closely spaced as possible without overlapping. The numbering convention for the aperture images adopted here, and shown in Fig. 7.2, is to number them in ascending order clockwise, starting with the top-left image.

7.2.3 Fourier analysis of the cone wavefront sensor

Taking the sequence of phase functions to the limit for N-sided prisms gives the cone sensor

$$h_\infty(u,v) = \exp[j2\pi b(\sqrt{u^2+v^2})], \quad (7.12)$$

Figure 7.2 The numbering of the aperture images for (a) the three sided case, and (b) the four sided case (pyramid sensor).

which produces an annular image. Since $h_\infty(u,v)$ is circularly symmetric, the IFT of the spatial filter for the cone can be computed using the inverse Hankel transform, which is defined in Section 2.5.6, and is reproduced here

$$G(r) = 2\pi \int_0^\infty g(\rho) J_0(2\pi\rho r)\, \rho \mathrm{d}\rho. \tag{7.13}$$

For the cone $h_\infty(\rho)$ is

$$h_\infty(\rho) = \exp[j2\pi b\rho], \tag{7.14}$$

and substituting this into Eq. (7.13) gives

$$H_\infty(r) = 2\pi \int_0^\infty \rho \exp[j2\pi b\rho] J_0(2\pi\rho r) \mathrm{d}\rho. \tag{7.15}$$

This integration can be performed using the following identity [88]

$$\int_0^\infty x^{m+1} \exp[-\alpha x] J_n(\beta x) \mathrm{d}x = (-1)^{m+1} \beta^{-n} \frac{\mathrm{d}^{m+1}}{\mathrm{d}\alpha^{m+1}} \left[\frac{(\sqrt{\alpha^2+\beta^2} - \alpha)^n}{\sqrt{\alpha^2+\beta^2}} \right], \tag{7.16}$$

and substituting $m = n = 0$, $\alpha = -j2\pi b$ and $\beta = 2\pi\rho$ gives the inverse Hankel transform of the spatial filter effect of the cone wavefront sensor

$$H_\infty(r) = \frac{-j8\pi^2 b}{(-4\pi^2 b^2 + 4\pi^2 r^2)^{3/2}}. \tag{7.17}$$

The magnitude of Eq. (7.17) is plotted in Fig. 7.3 for a slope, b, of 1 (ie 45°).

The image formed from the cone wavefront sensor without modulation is given by combining Eq.s (7.17) and (7.1)

$$I(\xi,\eta) = \left| \frac{-j8\pi^2 b}{(4\pi^2(-b^2+\xi^2+\eta^2))^{3/2}} \odot P(\xi,\eta) \exp[j\phi(\xi,\eta)] \right|^2. \tag{7.18}$$

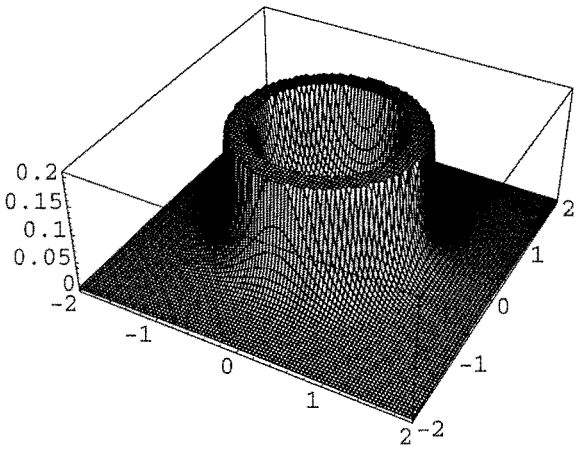

Figure 7.3 The IFT of the spatial filter describing the cone wavefront sensor with a face slope, b, of 1.

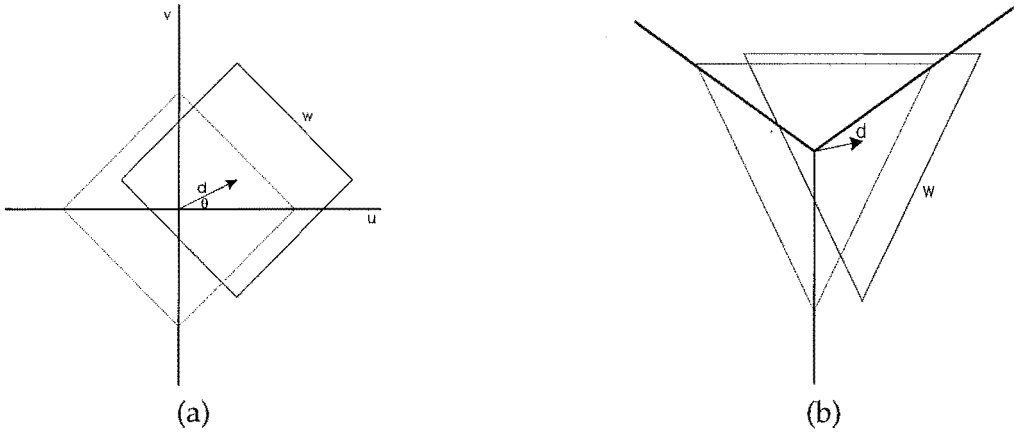

Figure 7.4 The modulation paths (solid lines) displaced by a distance d at an angle θ to the u axis in the focal plane from their rest positions (dotted lines) by a tip-tilt aberration for (a) the pyramid sensor (diamond path) and (b) the three sided prism (three sided path). The bold lines signify the lines of subdivision in the focal plane.

The image formed by the cone wavefront sensor is annular, like the magnitude of the IFT of the cone's spatial filter in Fig. 7.3.

7.2.4 Optimal modulation paths

Ragazzoni [11] noted that for the pyramid sensor, the optimal modulation path is diamond shaped (Fig, 7.4(a)) since this leads to a linear relationship between the displacement in the focal plane (and hence wavefront slope) and the estimated slopes. The confirmation that the diamond path does lead to a linear relationship between the spot displacement (s_u, s_v) and the estimated wavefront slope $(\partial\phi(\xi,\eta)/\partial\xi, \partial\phi(\xi,\eta)/\partial\eta)$ for the pyramid is shown in Appendix B. Also in Appendix B, the optimal path for the three-sided case is shown to be an equilateral triangle (Fig. 7.4(b)). The generalisation of the three and four sided cases is

that the optimal modulation path for an N-sided prism is a regular N-sided polygon. The optimal modulation path for the cone sensor is therefore a circular path.

In practice, the pyramid is modulated with a circular, rather than diamond, path since this is mechanically easier to produce. The circular path leads to a non-linear relationship between the wavefront slope and the measurements for the pyramid and the other members of this class, apart from the cone. However, the relationship is approximately linear for small wavefront slopes. In closed loop, the linear approximation provided by the circular path will drive the deformable mirror in the correct direction and the wavefront estimate will still converge to the true wavefront. The cone sensor has the advantage over other members of the class of wavefront sensors considered in this chapter that when using the circular path, which is mechanically the easiest to produce, there is a linear relationship between the wavefront slope and the measurements.

Modulation of the cone sensor with a circular path produces a phase shift of $H_\infty(\xi,\eta)$ by $\exp[j2\pi\xi u'']\exp[j2\pi\eta v'']$. Thus the aperture image resulting from modulation is given by the integral over the entire modulation path

$$I(\xi,\eta) = \int\int \left| \frac{-j8\pi^2 b \exp[j2\pi\xi u'']\exp[j2\pi\eta v'']}{(4\pi^2(-b^2+\xi^2+\eta^2))^{3/2}} \odot P(\xi,\eta)\exp[j\phi(\xi,\eta)] \right|^2 \mathrm{d}u''\mathrm{d}v''. \quad (7.19)$$

7.3 Reconstruction algorithms

The algorithms for estimating the wavefront from the aperture images are discussed in this section. The wavefront can be reconstructed from estimates of the wavefront slope calculated from the aperture images, or directly from the aperture images themselves. For an N-sided wavefront sensor, estimating the wavefront slope from the aperture images reduces N sets of measurements to two slope estimates. Some information contained in the aperture images is therefore inherently lost.

7.3.1 Reconstruction from slope estimates

Ragazzoni [11] generated formulae for the orthogonal slope estimates from the four aperture images for the pyramid sensor using simple geometrical considerations, Eq.s (4.10) and (4.11), which are repeated here

$$\frac{\partial\phi(\xi,\eta)}{\partial\xi} \propto \Big[I_1(\xi,\eta) - I_2(\xi,\eta) - I_3(\xi,\eta) + I_4(\xi,\eta)\Big] \Big/ \Big[\sum_{i=1}^{4} I_i(\xi,\eta)\Big] \quad (7.20)$$

$$\frac{\partial\phi(\xi,\eta)}{\partial\eta} \propto \left[I_1(\xi,\eta) + I_2(\xi,\eta) - I_3(\xi,\eta) - I_4(\xi,\eta)\right] \Big/ \left[\sum_{i=1}^{4} I_i(\xi,\eta)\right]. \tag{7.21}$$

Similar equations for the orthogonal slope components of the wavefront aberration can be derived from geometrical considerations for the class of N-sided oscillating prisms. Two specific cases are considered here: the three-sided and eight-sided representing reflectionally asymmetric and reflectionally symmetric cases respectively. The cone wavefront sensor is a special case since there are not distinct images as with the other wavefront sensors in this class. Thus a similar reconstruction procedure from geometric considerations is not possible. Instead, a reconstruction procedure directly from the images is proposed in the following subsection.

The three-sided oscillating prism produces three images situated at the vertices of an equilateral triangle as shown in Fig 7.2(a). Three slope vectors can be calculated by the difference between each pair of images. Eq.s (7.22) and (7.23) can then be formed by resolving these slope vectors into their constituent ξ and η components,

$$\frac{\partial\phi(\xi,\eta)}{\partial\xi} \propto \left[\frac{3}{2}\left(I_3(\xi,\eta) - I_2(\xi,\eta)\right)\right] \Big/ \left[\sum_{i=1}^{3} I_i(\xi,\eta)\right] \tag{7.22}$$

$$\frac{\partial\phi(\xi,\eta)}{\partial\eta} \propto \left[\frac{\sqrt{3}}{2}\left(2I_1(\xi,\eta) - I_2(\xi,\eta) - I_3(\xi,\eta)\right)\right] \Big/ \left[\sum_{i=1}^{3} I_i(\xi,\eta)\right]. \tag{7.23}$$

The eight-sided prism produces eight images located at the vertices of a regular octagon. Since the aperture images are arranged symmetrically in both the ξ and η directions, as they are with the pyramid sensor, the ξ slope estimate is simply the difference between the sum of the images on the right half plane and the sum of those on the left half plane,

$$\begin{aligned}\frac{\partial\phi(\xi,\eta)}{\partial\xi} \propto \Big[&I_1(\xi,\eta) - I_2(\xi,\eta) - I_3(\xi,\eta) - I_4(\xi,\eta) - I_5(\xi,\eta) \\ &+I_6(\xi,\eta) + I_7(\xi,\eta) + I_8(\xi,\eta)\Big] \Big/ \left[\sum_{i=1}^{8} I_i(\xi,\eta)\right]\end{aligned} \tag{7.24}$$

and similarly for the η dimension,

$$\begin{aligned}\frac{\partial\phi(\xi,\eta)}{\partial\eta} \propto \Big[&I_1(\xi,\eta) + I_2(\xi,\eta) + I_3(\xi,\eta) - I_4(\xi,\eta) - I_5(\xi,\eta) \\ &-I_6(\xi,\eta) - I_7(\xi,\eta) + I_8(\xi,\eta)\Big] \Big/ \left[\sum_{i=1}^{8} I_i(\xi,\eta)\right].\end{aligned} \tag{7.25}$$

In each of the above cases the weights of the first I Zernike polynomials, $\hat{a}$, are estimated with a Bayesian reconstructor, Eq. (4.21), reproduced here

$$\hat{a} = (C^{-1} + \Theta^T N^{-1} \Theta)^{-1} \Theta^T N^{-1} m, \tag{7.26}$$

where m is a vector consisting of the orthogonal slope estimates and C and N are the turbulence and noise covariance matrices as previously defined. The interaction matrix, Θ, is formed from the partial derivatives of the first I Zernike polynomials with respect to ξ and η.

7.3.2 Reconstruction directly from the aperture images

The pyramid, and the rest of the class of N-sided wavefront sensors, are linear over a range of slopes determined by the width of the modulation path. Hence if the wavefront sensor is perturbed with each of the first I Zernike modes scaled so that the sensor is still in its linear region, then the perturbations of the N resulting images are linear and can form a basis for reconstruction. Eq. (7.26) is again used for reconstruction but with Θ calculated from the images produced from each of the first I Zernike modes individually rather than the first I Zernike derivatives. The vector of measurements m is formed from the images rather than the slope estimates. In this new approach, a Bayesian least squares fit of the measured image is made to the images produced from each of the I Zernike modes. Reconstruction directly from the images is applicable to any of the N-sided oscillating prisms including the cone. The advantage of this method is that no information is discarded before the slope measurements are calculated.

The disadvantage of reconstructing directly from the aperture images is that it is more computationally intensive than reconstructing from the slope estimates. For the Bayesian reconstruction of Eq. (7.26), there is an increase in the size of both the m and Θ matrices when reconstructing from the aperture images rather than the slope estimates. For the pyramid sensor with aperture images of dimension $K \times K$ pixels and estimating the coefficients of I Zernike modes, the matrix of measurements m increases from dimension $2K^2 \times 1$ to $4K^2 \times 1$. Likewise, the interaction matrix Θ increases in size from $2K^2 \times I$ to $4K^2 \times I$ when reconstructing directly from the measurements as opposed to from the slope estimates.

7.4 Simulation results

In this section, simulation results are presented for the four examples of subdivision of the focal plane considered in the previous section. Firstly, the performance of these four wavefront sensors with respect to tip-tilt estimation is investigated. Then simulation of

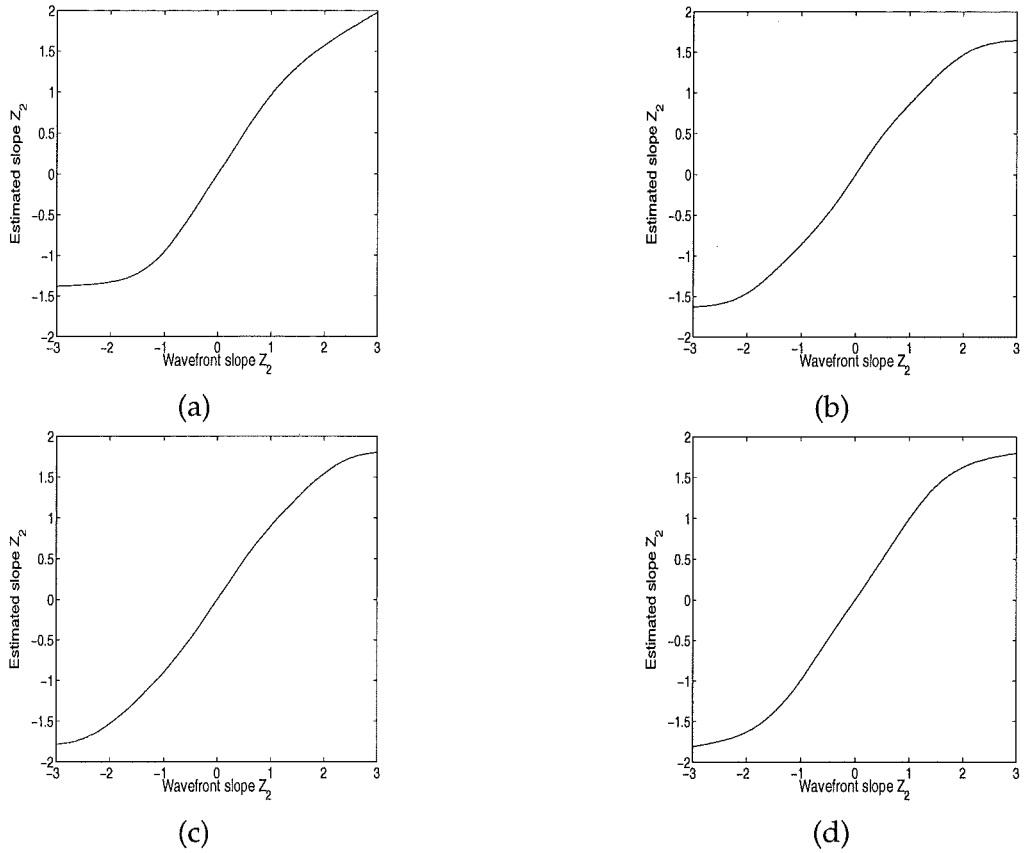

Figure 7.5 The global tip (Z_2) performance reconstructed directly from the images for (a) the three sided prism, (b) the pyramid, (c) the eight-sided prism and (d) the cone wavefront sensor.

these four sensors in the presence of atmospheric turbulence, and reconstructed with the two reconstruction algorithms, is discussed.

7.4.1 Tip-tilt performance

The tip-tilt performance of the N-sided prisms is investigated here. The coefficients of the tip and tilt are both increased linearly (ie the spot is moved along the path defined by $\alpha(Z_2 + Z_3)$). The coefficients of tip and tilt are then estimated at each point using the image method, and plotted in Fig.s 7.5 and 7.6 respectively. The width of the modulation path, w, is the same for all four sensors.

Fig.s 7.5 and 7.6 show that all four of the N-sided prisms considered do attain linear performance in two orthogonal directions. The three-sided case has a smaller linear range of tilt, but not tip, operation than the other sensors along this path. This asymmetric saturation of the three-sided case is due to the path (at 45° to the ξ axis) being asymmetric with respect to the axes of subdivision (Fig. 7.4(a)).

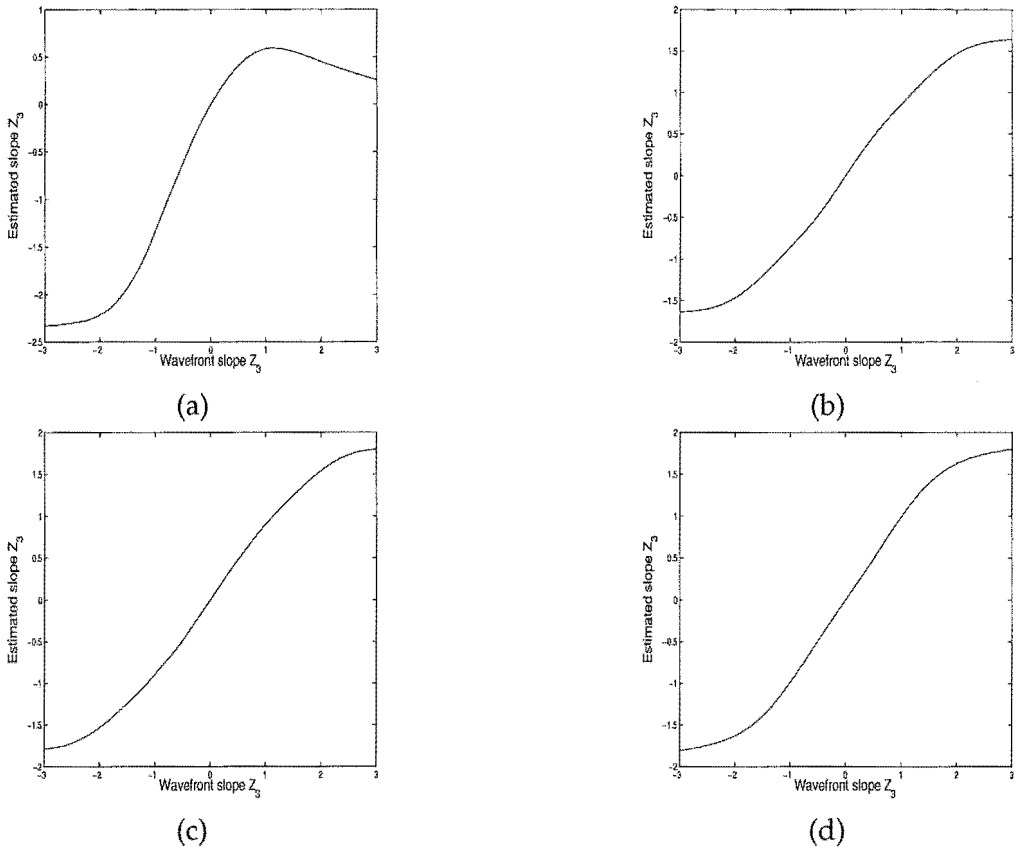

Figure 7.6 The global tilt (Z_3) performance reconstructed directly from the images for (a) the three sided prism, (b) the pyramid, (c) the eight-sided prism and (d) the cone wavefront sensor.

7.4.2 Atmospheric turbulence

The performance of these four wavefront sensors in atmospheric turbulence is also simulated for both reconstruction procedures. The phase screens are generated using the method of Harding *et al.*, which is described in Section 3.2.5. The severity of the atmospheric turbulence is set to $D/r_0 = 0.5$, where D is the aperture diameter and r_0 is the Fried parameter. This level of turbulence is chosen so that all four sensors remain in the linear range of operation as outlined in Section 7.2.4. Each of the four prisms is modulated with the same modulation width and its optimal modulation path.

In these simulations, the detectors used to detect the aperture images are assumed to be ideal, that is there is no read noise on the measurements. The noise on the measurements results only from the quantum nature of light, which is modelled as a Poisson random variable. The levels of Poisson photon noise on the speckle images investigated are 1e4 and 1e6 photons per frame.

The Mean-Squared Error (MSE) for the four wavefront sensors are averaged over 500 phase screens. For comparison, the mean-squared phase of the wavefront at the aperture is 0.85

rad^2. The phase reconstruction is made using the first 40 Zernike modes. The minimum achievable mean-squared error with 40 Zernike modes is 0.0038 rad^2.

Sensor	Photon Count	
	1e4 Photons	1e6 Photons
3-sided	0.0305 ± 0.0009	0.0292 ± 0.0009
4-sided (pyramid)	0.0192 ± 0.0006	0.0181 ± 0.0006
8-sided	0.0191 ± 0.0003	0.0176 ± 0.0003
∞-sided (cone)	-	-

Table 7.1 Mean-squared error (rad^2) in the reconstructed wavefront (± the standard error in the mean) for N-sided prism wavefront sensors for residual turbulence of D/r_0=0.5 reconstructed from the slope estimates.

The results presented in Table 7.1 for reconstruction from the slope estimates show that the three-sided case is inferior to the pyramid and eight-sided case. The latter two have equivalent performance. Table 7.2 shows that when reconstructing directly from the image measurements, as the number of sides of the prism increases, the MSE decreases. This is more evident at the higher photon level where the cone has the best performance with a significantly lower MSE than the pyramid.

Sensor	Photon Count	
	1e4 Photons	1e6 Photons
3-sided	0.0172 ± 0.0008	0.0128 ± 0.0008
4-sided (pyramid)	0.0120 ± 0.0004	0.0076 ± 0.0004
8-sided	0.0120 ± 0.0002	0.0060 ± 0.0002
∞-sided (cone)	0.0116 ± 0.0001	0.0053 ± 0.0001

Table 7.2 Mean-squared error (rad^2) in the reconstructed wavefront (± the standard error in the mean) from N-sided prism wavefront sensors for residual turbulence of D/r_0=0.5 reconstructed directly from the image measurements.

The similarity of the performance between the pyramid and eight-sided case when reconstructed from the estimated slopes is not unexpected since ultimately they are reduced to two slope measurements. However, when the measurements are used directly, more subdivision of the focal plane is beneficial.

The simulation results show that reconstructing directly from the aperture images provides a significantly more accurate wavefront estimate than reconstructing from the slope estimates. This is true for the 3-sided, 4-sided and 8-sided cases and at both levels of photon noise investigated. As noted previously, this improved wavefront estimate does come at a cost in computational complexity.

In the simulations presented in this section, the detectors are assumed to be ideal. In this case, the limiting noise is due to the quantum nature of light. However, current detectors are also subject to read noise. When the read noise on the detector dominates over the photon noise, it is expected that the sensor in the class that has the least number of pixels required to detect the aperture images minimises the read noise and produces the best wavefront estimate. The least number of images, and hence pixels, required to estimate the wavefront slope in two orthogonal directions is achieved by subdividing the focal plane in three with a three-sided prism.

7.5 Conclusion

In this chapter, a whole class of wavefront sensors is derived that subdivide the complex field at the origin of the focal plane into N equal segments. Simulation results in the presence of photon, but not read, noise show that at higher photon counts the performance improves with increased subdivision. The cone (∞ sides) sensor performs the best. The cone sensor has the added advantage that it does not require the images formed by the sensor to be physically separated. It is also the sensor in the class that is mechanically the easiest to modulate and get a linear response. Conversely, when read noise dominates over photon noise, it is expected that the sensor with the least number of pixels required to detect the aperture images, which is the three-sided case, will provide the best wavefront estimate.

An improved method for reconstructing the wavefront directly from the images rather than the estimated slopes has been proposed for pyramid type sensors. With this new method, simulations indicate a significant improvement in the reconstruction quality results from an increased subdivision of the focal plane. By estimating the wavefront directly from the aperture images, no information contained in the images is lost in estimating the wavefront slope in two orthogonal directions. This inherent information contained in the aperture images is exploited in the next chapter, Chapter 8, by performing phase retrieval in conjunction with subdivision at the focal plane and using the aperture images as a constraint.

Chapter 8

Phase Retrieval from Subdivision of the Focal Plane with a Lenslet Array

8.1 Introduction

Phase retrieval, and in particular the Gerchberg-Saxton (GS) and error-reduction (ER) algorithms, are introduced in Section 4.5.1. The difficulties with direct phase retrieval, such as slow convergence and the twin image problem, which are discussed in Section 4.5.1, mean that in practice wavefront sensors are employed to linearise the relationship between the phase and the measurements. However, there is an inherent loss of information in these devices since only part of the available measurements are used to reconstruct the wavefront. For example, with the Shack-Hartmann wavefront sensor, only the centroids of the low resolution images are used to estimate the wavefront. Phase retrieval in conjunction with a wavefront sensor can utilise all the available information from the wavefront sensor. The main drawback is that as an iterative phase retrieval procedure the algorithm is significantly more computationally intensive than the linear phase estimate provided by a conventional linear wavefront sensing scheme.

Phase retrieval from subdividing the aperture with the Shack-Hartmann sensor has been proposed by a number of authors [90–95]. Since the maximum phase error within each subaperture is smaller, phase retrieval within a subaperture is a simpler task. However, this approach still suffers from the twin image ambiguity problem [90], with the ambiguity occurring within each lenslet rather than over the entire aperture. In Chapter 6, a wavefront sensor based on subdividing the complex field in the focal plane with a lenslet array, and re-imaging the aperture at the conjugate aperture plane is proposed. In this chapter, a phase retrieval algorithm that uses a lenslet array at the focal plane to subdivide the complex

field at the focal plane is considered.

This approach provides the advantage over conventional phase retrieval, and phase retrieval using Shack-Hartmann sensor measurements, that the algorithm iterates between three Fourier planes instead of two, and thus the phase estimate is more heavily constrained. It is readily apparent that the subdivision at the focal plane removes any confusion between an object and its twin.

Phase retrieval from subdivision of the focal plane with a lenslet array can be used as either an open loop computer post-processing scheme or to drive the deformable mirror in a closed loop adaptive optics system. For the phase retrieval algorithm to operate in closed loop, the wavefront estimate must converge to an acceptable level within the coherence time of the atmosphere.

The importance of the choice of starting point for phase retrieval algorithms has been noted [95], and for phase retrieval from subdivision of the focal plane with a lenslet array this choice differs depending on whether the system is operating in open loop or closed loop. In a closed loop system, a good initial estimate of the wavefront phase is the previous estimate of the phase. In an open loop phase retrieval algorithm, the obvious starting point is the estimate provided from the linear approximation obtained from the measurements using Eq.s (6.20) and (6.21). It is possible to improve this initial estimate significantly when it is used as the starting point for the iterative phase retrieval, without the need for modulation. As a consequence, the sensitivity of the measurements is maintained.

The proposed phase retrieval algorithm is presented in Section 8.2. Simulation results are presented in Section 8.3 and the major findings of this chapter are summarised in Section 8.4.

8.2 Phase retrieval algorithm

Two phase retrieval algorithms based on the GS and ER algorithms and that take into account the physical subdivision of the lenslet array are proposed. The two algorithms are described in block diagram form by Fig. 8.1 for an array of $2M \times 2N$ lenslets. The quantities depicted in Fig. 8.1 are as follows: $G(x, y)$ is the complex field in the aperture, $g(u, v)$ is the total complex field in the focal plane, $g_{m,n}(u, v)$ is the section of the focal plane subdivided by the (m,n)th lenslet, $I_{mn,}(\xi, \eta)$ is the complex field at the conjugate aperture plane corresponding to the (m,n)th lenslet in the array. The dashed variables are used to show that the variable has satisfied the necessary constraints. The spatial filter effect, $h_{m,n}(u, v)$, of the (m,n)th lenslet is defined as 1 inside the lenslet and 0 outside it.

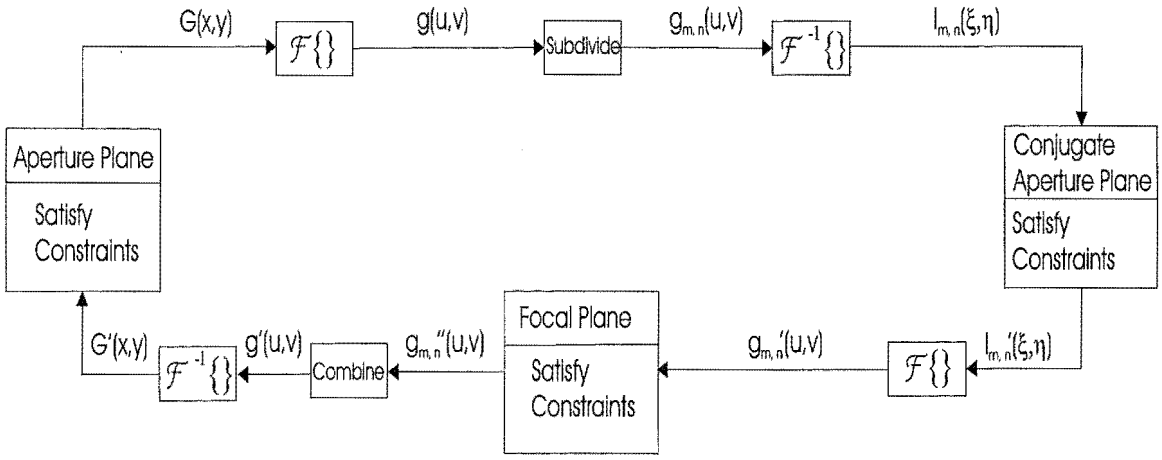

Figure 8.1 Block diagram of the phase retrieval approach from subdivision at the focal plane.

The important point of difference to note in comparison with the conventional GS/ER diagram, Fig. 4.11, is that phase retrieval from subdivision at the focal plane applies constraints at three Fourier planes rather than the two planes utilised by the traditional GS and ER.

The GS implementation of phase retrieval with subdivision at the focal plane can be summarised in nine steps:

(1) The current estimate of the complex field in the aperture, $G_k(x, y)$, is Fourier transformed to form $g(u, v)$, the complex field in the focal plane.

(2) The complex field in the focal plane, $g(u, v)$, is subdivided into $2M \times 2N$ sections forming $g_{m,n}(u, v)$.

(3) Each of $g_{m,n}(u, v)$ is inverse Fourier transformed to form $I_{m,n}(\xi, \eta)$, the complex field from each lenslet in the conjugate aperture plane.

(4) The magnitudes of $I_{m,n}(\xi, \eta)$ are made to conform with the measured moduli to form $I'_{m,n}(\xi, \eta)$.

(5) Each of $I'_{m,n}(\xi, \eta)$ is Fourier transformed to re-form the complex field sections in the focal plane, $g'_{m,n}(u, v)$.

(6) Steps (4) and (5) cause $g'_{m,n}(u, v)$, the estimated complex field sections in the focal plane, to spread to regions outside the known physical bounds of each lenslet. The spatial filter $h_{m,n}(u, v)$ defines a support constraint which can be enforced by multiplying the complex field estimated in the focal plane, $g'_{m,n}(u, v)$, to form $g''_{m,n}(u, v)$.

This effectively zeroes the complex field outside the known region of the focal plane occupied by the lenslet.

(7) The focal plane sections, $g''_{m,n}(u,v)$, are combined to form $g'(u,v)$, the overall complex field in the focal plane.

(8) The complex field in the focal plane, $g''(u,v)$, is inverse Fourier transformed to form $G'(x,y)$, the complex field in the aperture.

(9) $G'_k(x,y)$ is made to conform with the known object modulus, forming the new estimate of the complex field in the aperture, $G_{k+1}(x,y)$.

The ER implementation of phase retrieval with subdivision at the focal plane differs from its GS counterpart only in step (9). Instead of applying the magnitude in the aperture plane, a support constraint is applied based on the known aperture size. The new estimate of the complex field in the aperture, $G_{k+1}(x,y)$, is formed from making $G'_k(x,y)$ conform with the object support constraint:

$$G_{k+1}(x,y) = \begin{cases} G'_k(x,y) & (x,y) \notin \gamma \\ 0 & (x,y) \in \gamma, \end{cases} \tag{8.1}$$

where γ is the set that includes all the points outside the known aperture.

8.3 Simulation results

In this section, the phase retrieval algorithm is simulated in open loop in the presence of atmospheric turbulence. The atmospheric phase screens are generated using the method of Harding *et al.*, which is described in Section 3.2.5. The circular phase screens of dimension 32×32 pixels are placed inside 64×64 arrays of zeros before Fourier transforming to form the complex field at the focal plane. The severity of the atmospheric turbulence is set to $D/r_0 = 8$, where D is the aperture diameter and r_0 is the Fried parameter. The level of Poisson noise on the speckle images investigated are 5000 photons per frame. The algorithm is terminated after 200 iterations for each phase screen to allow for a fair comparison of all cases. As can be seen in Fig. 8.3, the choice of 200 iterations allows almost complete convergence for all four levels of subdivision simulated.

Three different starting points for the phase retrieval algorithm are tried for each phase screen: a starting phase of all zeros, the starting phase generated from the linear combination of the aperture images (Eq.s (6.20) and (6.21)), and the true starting point. The latter cannot be used in practice, but can be used to provide a reference by which the performance of the other two starting points can be judged. The starting phase estimate obtained

from the slope vectors provided by the linear wavefront sensing formulae is made using a Bayesian least squares reconstructor (Eq. 4.22)) to estimate the first 40 Zernike polynomials.

Array	Iteration	Starting phase		
		Zero	Linear estimate	True
2×2	Initial	0.013 ± 0.001	0.168 ± 0.004	1.000 ± 0.000
	After 200	0.085 ± 0.003	0.371 ± 0.007	0.696 ± 0.002
4×4	Initial	0.013 ± 0.001	0.223 ± 0.004	1.000 ± 0.000
	After 200	0.190 ± 0.006	0.654 ± 0.006	0.777 ± 0.001
8×8	Initial	0.013 ± 0.001	0.337 ± 0.004	1.000 ± 0.000
	After 200	0.271 ± 0.003	0.697 ± 0.007	0.722 ± 0.001
16×16	Initial	0.013 ± 0.001	0.160 ± 0.005	1.000 ± 0.000
	After 200	0.277 ± 0.015	0.519 ± 0.014	0.608 ± 0.006

Table 8.1 The mean Strehl ratios ($\pm$ the standard error in the mean) obtained for phase retrieval using the GS algorithm with arrays of 2×2, 4×4, 8×8, and 16×16 lenslets at the focal plane with turbulence of severity D/r_0=8 and 5000 photons per screen.

Array	Iteration	Starting phase		
		Zero	Linear estimate	True
2×2	Initial	0.013 ± 0.001	0.168 ± 0.004	1.000 ± 0.000
	After 200	0.032 ± 0.001	0.166 ± 0.004	0.490 ± 0.002
4×4	Initial	0.013 ± 0.001	0.223 ± 0.004	1.000 ± 0.000
	After 200	0.080 ± 0.003	0.388 ± 0.006	0.655 ± 0.002
8×8	Initial	0.013 ± 0.001	0.339 ± 0.003	1.000 ± 0.000
	After 200	0.206 ± 0.005	0.613 ± 0.003	0.690 ± 0.001
16×16	Initial	0.013 ± 0.001	0.161 ± 0.005	1.000 ± 0.000
	After 200	0.310 ± 0.013	0.531 ± 0.010	0.640 ± 0.004

Table 8.2 The mean Strehl ratios ($\pm$ the standard error in the mean) obtained for phase retrieval using the ER algorithm with arrays of 2×2, 4×4, 8×8, and 16×16 lenslets at the focal plane with turbulence of severity D/r_0=8 and 5000 photons per screen.

The Strehl ratios are averaged over 1000 screens for the 2×2, 4×4 and 8×8 arrays. The mean Strehl ratio for the 16×16 array is averaged over 200 phase screens only due to the increased computational complexity of the increased subdivision. These mean Strehl ratios are tabulated in Tables 8.1 and 8.2 for the GS and ER routines respectively. The uncertainty values tabulated are the standard errors in the mean.

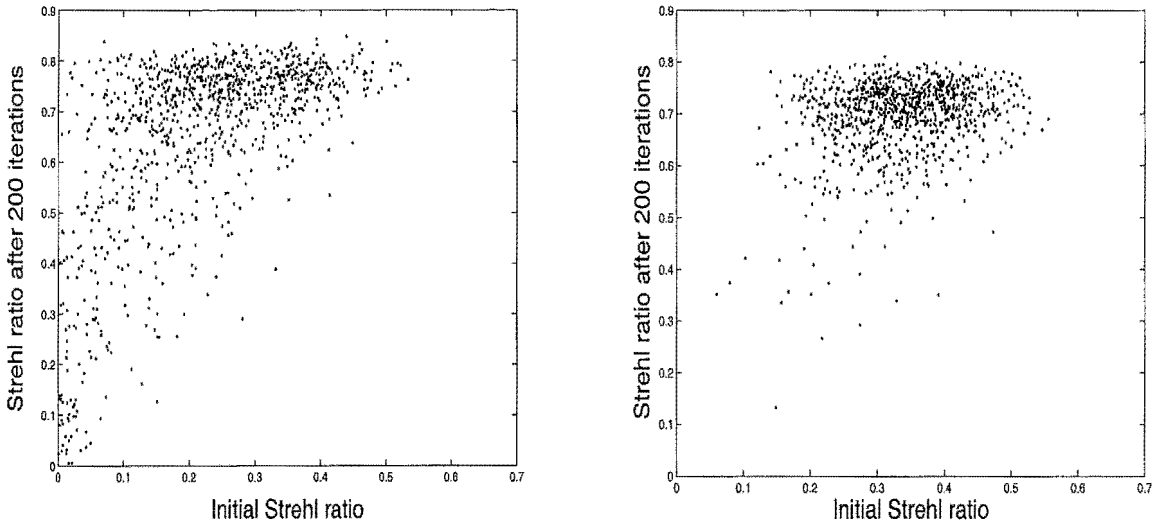

Figure 8.2 The Strehl after 200 iterations for the GS method versus the initial Strehl from the linear estimate at D/r_0=8 for 1000 screens with an array of (a) 4×4, and (b) 8×8 lenslets.

It is clear from Tables 8.1 and 8.2 that the GS implementation of phase retrieval with subdivision at the focal plane achieves better results than the ER implementation. This is not surprising since the GS method assumes the magnitude of the wavefront is correctly known, whereas the ER method uses only the support. The latter is however applicable only when the level of scintillation cannot be assumed to be negligible.

The performance of the algorithm is dependent on the amount of subdivision in the focal plane from the lenslet array. Arrays with fewer elements cannot determine the slope at each point in the aperture as accurately as those with more elements. However, the arrays with fewer elements can provide greater resolution about the slope in the aperture. At the simulated level of turbulence, $D/r_0 = 8$, the optimal amount of subdivision of the focal plane is with an 8×8 array of lenslets. This result is true for both the GS and ER implementations when starting with the initial estimate provided by the linear wavefront sensing formulae.

The phase estimate provided by the linear wavefront sensing formulae yields a better result for all four different sized lenslet arrays than from starting with zero phase for the both the GS and ER implementations. Fig. 8.2 shows the relationship between the initial estimate from the linear wavefront sensing formulae and the retrieved phase for the 4×4 and 8×8 arrays for the GS case. It is important to note that the result from phase retrieval is rarely worse (less than 1 percent of the time) than the initial estimate provided by the linear wavefront sensing formulae. For the 4×4 case, the Strehl after 200 iterations of phase retrieval is dependent on the quality of the initial estimate. When the initial estimate is poor (Strehl less than 0.1), the Strehl after phase retrieval is variable, ranging between

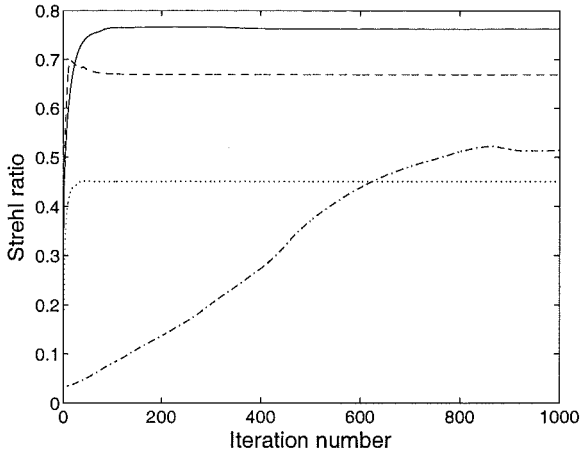

Figure 8.3 The Strehl ratio at each iteration using the GS method of phase retrieval with subdivision at the focal plane for one phase screen of severity D/r_0=8, and 5000 photons for the 2×2 (dash-dotted), 4×4 (solid), 8×8 (dashed) and 16×16 (dotted) lenslet arrays with the starting estimate provided by the linear estimate.

0.005 and 0.85. However, when the initial estimate is good (Strehl greater than 0.4), the Strehl after phase retrieval is usually significantly improved (always greater than 0.5). The dependence on the quality of the initial estimate is not as marked for the 8×8 case.

It is also interesting to note from Fig. 8.2 that although the mean Strehl for the 8×8 case is significantly higher than that of the 4×4 case, the highest Strehls obtained with the 4×4 array are higher than the highest with the 8×8 array. These cases arise when the phase screen falls in the linear part of the tip-tilt curve (Fig. 6.8(b)) for the 4×4 array and benefit from the reduced subdivision, and hence reduced loss of information, of the 4×4 array compared with the 8×8 array. However, the majority of the cases for the 8×8 array fall in the saturation regions of Fig. 6.8(b), which is why the mean of the 4×4 array is worse than that of the 8×8 array.

With the optimal case of an 8×8 array for the GS implementation, the mean Strehl starting from the linear estimate and the mean Strehl starting from the true phase (0.697 cf. 0.722) are very close, indicating that in most cases the algorithm reaches the same local maximum for both starting points. Fig. 8.3 shows that as the algorithm progresses, the Strehl generally increases, although the overshoot in the 2×2 and 8×8 cases indicates some over-fitting of the data. The use of regularisation can be considered to overcome this problem [95]. Fig. 8.3 also shows that convergence to the local maximum is faster when there is a greater amount of subdivision at the focal plane.

The simulations presented in this chapter have assumed only a phase aberration, and not a magnitude aberration (scintillation). It is possible to estimate the magnitude aberration and incorporate it into the GS form of this algorithm. The magnitude at the aperture can be

measured by splitting some of the light from the aperture with a beam-splitter and imaging the aperture. Alternatively, a low-resolution image of the aperture can be obtained from the mean of the aperture images provided by the lenslet array. This second method has the advantage that no photons are used in estimating the magnitude of the aperture. This measured magnitude at the aperture can then be applied as a constraint in the aperture plane in the GS algorithm.

As with the simulations presented in the two previous chapters, the simulation results for the phase retrieval algorithm were obtained under the assumption of ideal detectors. With current detectors there exists non-trivial levels of read noise. In this case, the larger the amount of subdivision of the focal plane, which produces more images at the conjugate aperture plane and hence requires more detector pixels to capture the aperture images, the more read noise is introduced into the system. Thus the level of read noise of the detector will affect the choice of the optimal number of lenslets in the focal plane for this phase retrieval algorithm.

8.4 Conclusion

In this chapter, a phase retrieval algorithm in conjunction with a lenslet array at the focal plane has been shown to provide a simple method for improving a wavefront estimate. This phase retrieval algorithm can, in almost all cases, provide a more accurate estimate of the wavefront than from the linear estimate obtained from the wavefront sensing formulae. This method also avoids the twin image ambiguity problem that limits the ability of phase retrieval in conjunction with the Shack-Hartmann wavefront sensor. Starting this phase retrieval algorithm from the linear combination of the aperture images is far superior to starting from zero phase. The performance of the algorithm is dependent on the amount of subdivision at the focal plane, with the optimal choice of the size of lenslet array a trade-off between slope accuracy and the loss of information due to subdivision.

Chapter 9

Conclusions and Future Work

This thesis investigates methods for improving the estimation of wavefronts that have been aberrated by the earth's atmosphere. The purpose of this chapter is to summarise and draw together the original material of this thesis, contained in Chapters 5, 6, 7 and 8. A number of areas for further research have arisen as a consequence of the work done in this thesis. These future research topics are outlined in Section 9.2.

9.1 Conclusions

The problem in astronomical imaging is that wavefronts from astronomical objects incur a phase distortion as they pass through the earth's atmosphere. This phase aberration causes a loss in resolution in images captured with ground-based telescopes. The phase aberration can be compensated in real-time with a closed loop adaptive optics system, or with an open loop computer post-processing algorithm. This thesis has made contributions to both adaptive optics, particularly in the field of wavefront sensing, and computer post-processing, with a new phase retrieval algorithm.

The pyramid wavefront sensor can be generalised by placing a lenslet array at the focal of the telescope. The use of a lenslet array at the focal plane allows the duality between the Shack-Hartmann and pyramid sensors to be shown. This duality arises as the two wavefront sensing schemes subdivide each of a Fourier transform pair: the complex fields at the aperture (Shack-Hartmann) and focal (pyramid) planes, with a lenslet array. In particular, the number of lenslets used in the focal plane is analogous to the number of pixels used to detect each image in the Shack-Hartmann, and the number of pixels used to detect each image from the lenslet array at the focal plane is analogous to the number of lenslets used in the Shack-Hartmann sensor. Also, both sensors estimate the slope with a centroid operator.

A trade-off between the attainable spatial resolution and slope accuracy exists for both the lenslet array at the focal plane and the Shack-Hartmann sensor. In both cases the trade-off is determined by the size of the lenslets in the array. Simulation results for atmospheric phase screens show equivalent performance between the lenslet array at the aperture and focal planes in open loop. When the lenslet array at the focal plane is modulated, which increases its linear range of operation, the wavefront estimate is better than either the lenslet array at the aperture plane or focal plane without modulation.

The pyramid wavefront sensor estimates the wavefront by subdividing the complex field in the focal plane into quadrants with a four-sided glass prism and producing four images of the aperture. Yet it is possible to estimate the wavefront by subdividing the complex field in the focal plane into any N equal segments, and producing N aperture images, where $N \geq 3$. Simulation results at high photon levels show that an increased amount of subdivision at the focal plane yields an improved wavefront estimate, with the cone sensor, ∞ sides, providing the best wavefront estimate. The three-sided prism, which is the least number of sides required to estimate the wavefront slope in two orthogonal directions, has the advantage that it requires the least number of pixels to detect the aperture images, and this is significant when the detector is limited by read noise.

For the pyramid sensor, estimating the wavefront directly from the aperture images is shown to give an improved wavefront estimate over the conventional method of estimating the wavefront from the slope estimates, which are formed from the aperture images. This is because some information contained in the aperture images is inherently lost when the four vectors of measurements are reduced to two vectors of slope estimates. Estimating the wavefront directly from the aperture images is applicable to all members in the class of N-sided wavefront sensors.

A phase retrieval algorithm based on subdivision of the focal plane with a lenslet array is shown to significantly improve the wavefront estimate that can be attained as a linear combination of the aperture images. This algorithm applies constraints at three Fourier planes, unlike conventional phase retrieval or phase retrieval in conjunction with the Shack-Hartmann sensor, which only apply constraints at two planes. By subdividing at the focal plane, the modulus ambiguity between an object and its twin, which hampers other phase retrieval algorithms, is removed.

A new method for calibrating the reference positions for the Shack-Hartmann sensor provides results of equivalent quality, but without the physical hardware currently employed. This new method operates by optimising the Strehl ratio of an observed source, rather than using a calibration laser. This calibration technique is applicable to both computer post-processing and adaptive optics systems.

9.2 Future research

The most scope for future research resulting from work done in this thesis is in the practical implementation of the concepts described in Chapters 6, 7 and 8. Although the 2×2 lenslet array at the focal plane and the pyramid sensor are theoretically equivalent, one or other may have a practical advantage that can only be determined experimentally. In particular, the pyramid sensor loses light at the intersections between the prism faces, and the lenslet array at the focal plane will also lose light at the intersection between the lenslets. Yet it is unclear without experimental testing which of the two sensors will be more severely affected.

As noted previously, a drawback of the pyramid sensor is that light is lost at the intersections between the prism faces. However, this loss is largely ignored in the literature. When comparing prisms with differing numbers of sides, and hence numbers of intersections between the sides, this loss needs to be incorporated, and can only be measured in an experimental set-up. Also, the simulations comparing prisms with differing numbers of sides, and hence aperture images, in Chapter 7 assume the detectors are ideal. With present detectors this assumption is not valid, and more significantly, the total read noise will depend on the number of detector pixels required.

The phase retrieval algorithm from subdivision of the focal plane can only be used in a closed loop adaptive optics system if the wavefront can be estimated to a sufficient level of accuracy while the atmosphere is still essentially frozen. This algorithm needs to be implemented on specialised DSP hardware to determine whether closed loop operation is indeed possible.

In Chapter 6, a duality between the Shack-Hartmann and pyramid sensor implemented as a lenslet array is shown to exist. A stated advantage of the pyramid sensor over the Shack-Hartmann sensor is that modulation of the pyramid, or alternatively the lenslets at the focal plane, can increase the linear range of operation. The dual of the lenslets at the focal plane of the pyramid sensor are the pixels used to detect the images in the Shack-Hartmann sensor. Thus modulation of the pixels, or equivalently light onto the pixels with a tip-tilt mirror, can increase the linear range of operation of the Shack-Hartmann sensor. This modulation of the Shack-Hartmann sensor needs to be analysed and its performance in comparison to modulation of the pyramid sensor quantified.

In Chapter 6, the lenslet array at the aperture (Shack-Hartmann sensor) and focal (pyramid sensor) planes are only considered in terms of open loop operation, for which they have equivalent performance. However, in closed loop operation the lenslet array at the focal plane offers a significant advantage. With the lenslet array at the focal plane, as the

loop is successfully closed, the residual wavefront aberrations become smaller and consequently the complex field (spot) in the focal plane becomes narrower, and approaches the diffraction-limited core. The sensitivity of the measurements with the lenslet array at the focal plane is inversely proportional to the size of the spot in the focal plane, so the sensitivity of the lenslet array at the focal plane improves in closed loop operation. There is no corresponding increased sensitivity in the Shack-Hartmann sensor as the loop is successfully closed.

As noted in Section 4.4.2, for the Shack-Hartmann sensor the spots in each subaperture are elongated when viewing a LGS, and this creates an error in the centroid measurement. The variations on the pyramid sensor considered in this thesis, namely the lenslet array at the focal plane and the N-sided prisms, should be analysed to see whether they offer any inherent advantage over the Shack-Hartmann sensor for this problem.

A further improvement to the Shack-Hartmann sensor is to shift the lenslets in the aperture in order to increase the spatial resolution of the wavefront estimate. The slope measurements across each of the lenslets are taken for each shifted position of the lenslet array. These slope measurements can then be combined to form an estimate of the phase across the aperture with greater resolution. Four displacements of the lenslet array by $(0,0)$, $(\frac{d}{2},0)$, $(0,\frac{d}{2})$ and $(\frac{d}{2},\frac{d}{2})$ can improve the spatial resolution by a factor of two. This shifting of the lenslet array, like the modulation of the pyramid sensor, can be realised with a tip-tilt mirror.

Appendix A

Practical Considerations for the Lenslet Array at the Focal Plane

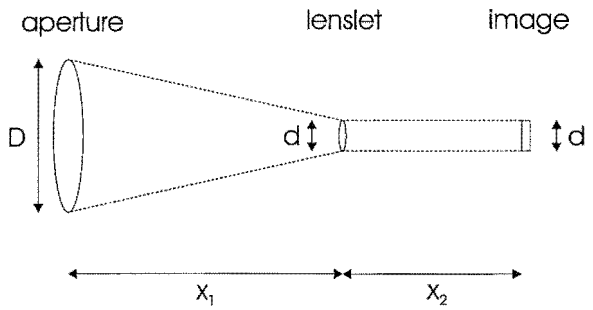

Figure A.1 The optical layout of a lenslet of width d and focal length x_2 at the focal plane of an aperture of diameter D and focal length x_1.

The optical layout for a lenslet at the focal plane is shown in Fig. A.1. The telescope aperture is of diameter D and focal length x_1. The lenslet, of width d, is placed at the focal plane and the aperture image is captured at the conjugate aperture plane a distance x_2 away from the focal plane. The focal length of the lenslet, f_l, is given by

$$\frac{1}{f_l} = \frac{1}{x_1} + \frac{1}{x_2}, \tag{A.1}$$

and since typically $x_2 \lll x_1$, then $f_l \approx x_2$. As stated in Section 6.3, for a large linear range of the array without modulation, the lenslet width is required to be equivalent to the width of the main lobe of the spot in the focal plane, $\frac{2.44\lambda x_1}{D}$. This condition is satisfied by

$$d = \frac{2.44\lambda x_1}{D}. \tag{A.2}$$

With no tilt applied to the aperture images, the maximum width that each image can be

without the images overlapping is d. Geometric considerations of Fig. A.1 gives

$$\frac{d}{D} = \frac{x_2}{x_1}. \tag{A.3}$$

Substituting Eq. (A.2) in to Eq. (A.3) and solving for d, the lenslet width, we find that

$$d = \frac{2.44\lambda x_2}{d} = 2.44\lambda F_2, \tag{A.4}$$

where F_2 is the focal number of the lenslet. Eq. (A.4) gives the design constraint on the size of the image in the conjugate aperture plane. The blurring of the aperture image is given by

$$d = 2.44\lambda F_2 = \frac{2.44\lambda x_2}{d}, \tag{A.5}$$

which means that the blurring in the conjugate aperture plane is equal to the size of the image in the conjugate aperture plane. Thus no resolution within the aperture is obtainable if the lenslet width is to be the same as the spot size.

To overcome this problem a displacement needs to be introduced to each of the images of the aperture. This displacement of the images can be achieved by either the use of prisms in a similar manner to the pyramid sensor, such as with a pyramid array, or by combining a tilt term directly into each of the lenslets in the array.

Appendix B

Optimal Modulation Paths

Consider a wavefront with a tip-tilt aberration that causes a displacement of the modulation path by a distance d at an angle θ to the u axis of the focal plane as shown in Fig. 7.4(a). The modulation path has a width w. In all cases, the spot and, hence path, displacement is given by (s_u, s_v)=$(d\cos\theta, d\sin\theta)$. The intensity formed in each of the four images is assumed to be proportional to the length of the modulation path in the respective subdivided quadrant. This implicitly assumes the spot size is zero. The aperture images are therefore found by applying the sine rule to find the length of each segment in Fig. 7.4(a) yielding

$$\begin{aligned} I_1 &= w - \sqrt{2}d\cos\theta + \sqrt{2}d\sin\theta \\ I_2 &= w + \sqrt{2}d\cos\theta + \sqrt{2}d\sin\theta \\ I_3 &= w + \sqrt{2}d\cos\theta - \sqrt{2}d\sin\theta \\ I_4 &= w - \sqrt{2}d\cos\theta - \sqrt{2}d\sin\theta. \end{aligned} \tag{B.1}$$

Substituting the image values in Eq. (B.1) into Eq.s (7.20) and (7.21) yields:

$$\begin{aligned} \frac{\partial\phi(\xi,\eta)}{\partial\xi} &= \frac{\sqrt{2}d\cos\theta}{w} \\ \frac{\partial\phi(\xi,\eta)}{\partial\eta} &= \frac{\sqrt{2}d\sin\theta}{w}. \end{aligned} \tag{B.2}$$

The ratio of the displacement of the modulation path to the estimated slope value in both the ξ and η dimensions is

$$\begin{aligned} s_u \Big/ \frac{\partial\phi(\xi,\eta)}{\partial\xi} &= d\cos\theta \Big/ \frac{\sqrt{2}d\cos\theta}{w} = \frac{w}{\sqrt{2}} \\ s_v \Big/ \frac{\partial\phi(\xi,\eta)}{\partial\eta} &= d\sin\theta \Big/ \frac{\sqrt{2}d\sin\theta}{w} = \frac{w}{\sqrt{2}}, \end{aligned} \tag{B.3}$$

which is the same value in both directions and independent of θ and d. Since the ratio of the displacement to the estimated slope is constant and the same in both directions, the diamond path is indeed the optimal path for the pyramid sensor.

Similarly for the three-sided case, the three aperture images are given by the length of the modulation path in each of the three subdivided sections. Applying the sine rule to find these lengths and simplifying yields

$$\begin{aligned} I_1 &= w + 2\sqrt{3}d\sin\theta \\ I_2 &= w + 3d\cos\theta - \sqrt{3}d\sin\theta \\ I_3 &= w - \sqrt{3}d\sin\theta - 3d\cos\theta. \end{aligned} \tag{B.4}$$

The wavefront slopes are found by substituting these values into Eq.s (7.22) and (7.23),

$$\begin{aligned} \frac{\partial\phi(\xi,\eta)}{\partial\xi} &= \frac{3d\cos\theta}{w} \\ \frac{\partial\phi(\xi,\eta)}{\partial\eta} &= \frac{3d\sin\theta}{w}. \end{aligned} \tag{B.5}$$

The ratio of the displacement to the estimated slope values for the three-sided case with equilateral modulation is

$$\begin{aligned} s_u \Big/ \frac{\partial\phi(\xi,\eta)}{\partial\xi} &= d\cos\theta \Big/ \frac{3d\cos\theta}{w} = \frac{w}{3} \\ s_v \Big/ \frac{\partial\phi(\xi,\eta)}{\partial\eta} &= d\sin\theta \Big/ \frac{3d\sin\theta}{w} = \frac{w}{3}, \end{aligned} \tag{B.6}$$

which is similarly independent of d and θ and the same in both directions. Thus the regular three-sided (equilateral) modulation path is the optimum one for the three-sided prism.

References

[1] National Aeronautics and Space Administration website, http://www.hubble.nasa.gov (2004).

[2] Starfire Optical Range website, http://www.sor.plk.af.mil/images/binary.htm (1999).

[3] H. W. Babcock, "The Possibility of compensating astronomical seeing," Pub. Astron. Soc. Pac. **65**, 229-236 (1953).

[4] M. Schock, D. Le Mignant, G. A. Chanan, P. L. Wizinowich and M. A. van Dam, "Atmospheric turbulence characterization with the Keck adaptive optics systems. I. Open-loop data," Appl. Opt. **42**, 3705-3720 (2003).

[5] C. E. Max, S. S. Olivier, H. W. Friedman, K. An, K. Avicola, B.V. Beeman, H. D. Bissinger, J. M. Brase, G. V. Erbert, D. T. Gavel, K. Kanz, M. C. Liu, B. Macintosh, K. P. Neeb, J. Patience, and K. E. Waltjen, "Image improvement from a sodium-layer laser guide star adaptive optics system," Science **277**, 1649-1652 (1997).

[6] D. Barnaby, E. Spillar, J. C. Christou and J. D. Drummond, "Measurements of binary stars with the starfire optical range adaptive optics systems," Astron. J. **119**, 378-389 (2000).

[7] H. Takami, N. Takato, Y. Hayano, M. Iye, S. Oya, Y. Kamata, T. Kanzawa, Y. Minowa, M. Otsubo, K. Nakashima, W. Gaessler and D. Saint-Jacques, "Performance of Subaru Cassegrain Adaptive Optics system," Pub. Astron. Soc. Japan **56**, 225-234 (2004).

[8] R. Irwan, "Wavefront estimation in astronomical imaging," PhD thesis, University of Canterbury (1999).

[9] Canada-France-Hawaii Telescope website, http://www.cfht.hawaii.edu/Instruments/Imaging/AOB/pictures.html (1996).

[10] Starfire Optical Range website,
http://www.sor.plk.af.mil/images/exper/jpeg/satcomp.jpg (1999).

[11] R. Ragazzoni, "Pupil plane wavefront sensing with an oscillating prism," J. Mod. Opt. **43**, 289-293 (1996).

[12] S. S. Haykin, *Communication sytems*, 3rd edition, Wiley, New York (1994).

[13] R. N. Bracewell, *The Fourier transform and its applications*, 2nd edition, McGraw-Hill, Singapore (1986).

[14] R. H. T. Bates and M. J. McDonnell, *Image restoration and reconstruction*, Clarendon press, Oxford (1986).

[15] H. Anton, *Elementary linear algebra*, 5th edition, Wiley, New York (1987).

[16] J. W. Cooley and J. W. Tukey, "An Algorithm for the Machine Calculation of Complex Fourier Series," Math. Comput. **19**, 297-301 (1965).

[17] W. Mendenhall and R. J. Beaver, *Introduction to probability and statistics*, 8th edition, PWS-KENT, Boston (1991).

[18] A. Papoulis, *Probability, random variables, and stochastic processes*, 2nd edition, McGraw-Hill, New York (1984).

[19] J. C. Dainty, "Optical effects of atmospheric turbulence" in *Laser Guide Star Adaptive Optics for Astronomy*, N. Ageorges and J. C. Dainty, eds. (Kluwer, Dordrecht, The Netherlands, 2000), pp. 1-21.

[20] M. C. Roggemann and B. Welsh, *Imaging through turbulence*, CRC Press, Boca Raton, Fla. (1996).

[21] P. A. Tipler, *Physics*, 2nd edition, Worth Publishers, New York (1982).

[22] M. A. van Dam, "Wave-front sensing for adaptive optics in astronomy," PhD thesis, University of Canterbury (2002).

[23] M. R. Teague, "Deterministic phase retrieval: a Green's function solution," J. Opt. Soc. Am. **73**, 1434-1441 (1983).

[24] M. A. van Dam and R. G. Lane, "Extended analysis of curvature sensing," J. Opt. Soc. Am. A **19**, 1390-1397 (2002).

[25] M. A. Van Dam and R. G. Lane, "Wave-front sensing from defocused images by use of wave-front slopes," Appl. Opt. **26**, 5497-5502 (2002).

[26] J. Goodman, *Introduction to Fourier optics* McGraw-Hill, New York (1996).

[27] R. K. Tyson, *Introduction to adaptive optics*, SPIE Press, Bellingham, Washington (2000).

[28] D. L. Fried, "Atmospheric turbulence optical effects: understanding the adaptive-optics implications" in *Adaptive Optics for Astronomy*, D. M. Alloin and J.-M. Mariotti, eds. (Kluwer, Dordrecht, The Netherlands, 1994), pp. 25-58.

[29] D. L. Fried, "Optical resolution through a randomly inhomogenous medium for very long and very short exposures," J. Opt. Soc. Am. A **56**, 1376-1379 (1966).

[30] R. G. Lane, A. Glindemann and J. C. Dainty, "Simulation of a Kolmogorov phase screen," Waves in Random Media **2**, 209-224 (1992).

[31] F. Roddier, "Theoretical Aspects", in *Adaptive Optics in Astronomy*, F. Roddier, ed. (Cambridge University Press, Cambridge, 1999), pp. 25-56.

[32] D. L. Fried, "Statistics of a geometric representation of wavefront distortion," J. Opt. Soc. Am. A **55**, 1427-1435 (1965).

[33] F. Roddier, "The effect of atmospheric turbulence in optical astronomy," in *Progress in Optics*, E. Wolf, ed. (North-Holland, Amsterdam, 1981), pp. 283-376.

[34] R. Noll, "Zernike polynomials and atmospheric turbulence," J. Opt. Soc. Am. A **66**, 207-211 (1976).

[35] C. M. Harding, R. A. Johnston and R. G. Lane, "Fast simulation of a Kolmogorov phase screen," Appl. Opt. **38**, 2161-2170 (1999).

[36] R. Johnston, "Inverse problems in astronomical imaging," PhD thesis, University of Canterbury (2000).

[37] J. Primot, G. Rousset and J.C. Fontanella, "Deconvolution from wave-front sensing: a new technique for compensating turbulence-degraded images," J. Opt. Soc. Am. A **7**, 1598-1608 (1990).

[38] F. Roddier, "Imaging through the atmosphere", in *Adaptive Optics in Astronomy*, F. Roddier, ed. (Cambridge University Press, Cambridge, 1999), pp. 9-24.

[39] R. A. Muller and A. Buffington, "Real-time correction of atmospherically degraded telescope images through image sharpening," J. Opt. Soc. Am. **64**, 1200-1210 (1974).

[40] J. R. Fienup and J. J. Miller, "Aberration correction by maximising generalized sharpness metrics," J. Opt. Soc. Am. A **20**, 609-620 (2003).

[41] R. Irwan and R. G. Lane, "Analysis of optimal centroid estimation applied to Shack-Hartmann sensing," Appl. Opt. **38**, 6737-6743 (1999).

[42] National Optical Astronomy Observatory website http://www.ctio.noao.edu (2001).

[43] R.G. Lane and M. Tallon, "Wave-front reconstruction using a Shack-Hartmann sensor," J. Opt. Soc. Am. A **31**, 6902-6908 (1992).

[44] G. A. Tyler and D. L. Fried, "Image-position error associated with a quadrant detector," J. Opt. Soc. Am. **72**, 804-808 (1982).

[45] M. A. van Dam and R. G. Lane, "Wave-front slope sensing," J. Opt. Soc. Am. A **17**, 1319-24 (2000).

[46] F. Roddier, "Curvature sensing and compensation: a new concept in adaptive optics," Appl. Opt. **27**, 1223-1225 (1988).

[47] F. Roddier, "Wavefront sensing and the irradiance transport equation," Appl. Opt. **29**, 1402-1403 (1990).

[48] F. Roddier, M. Northcott and J. E. Graves, "A simple low-order adaptive optics system for near-infrared applications," Publ. Astron. Soc. Pac. **103**, 131-149 (1991).

[49] S. Esposito, A. Riccardi, "Pyramid wavefront sensor behavior in partial correction adaptive optic systems," A. & A. **369**, L9-L12 (2001).

[50] R. Ragazzoni, J. Farinato, "Sensitivity of a pyramidic wave front sensor in closed loop adaptive optics," A. & A. **350**, L23-L26 (1999).

[51] I. Iglesias, R. Ragazzoni, Y. Julien and P. Artal, "Extended source pyramid wave-front sensor for the human eye," Opt. Express **10**, 419-428 (2002).

[52] R. Ragazzoni, E. Diolaiti and E. Vernet, "A pyramid wavefront sensor with no dynamic modulation," Opt. Comms. **208**, 51-60 (2002).

[53] R. Gale Wilson, "Wavefront-error evaluation by mathematical analysis of experimental Foucault-test data," Appl. Opt. **14**, 2286-2297 (1975).

[54] E. P. Wallner, "Optimal wave-front correction using slope measurements," J. Opt Soc. Am. A **73**, 1771-1776 (1983).

[55] N. F. Law, R. G. Lane, "Wavefront estimation at low light levels," Opt. Comms. **126**, 19-24 (1996).

[56] E. N. Ribak, "Deformable morrors," in *Adaptive Optics for Astronomy*, D. M. Alloin and J.-M. Mariotti, eds. (Kluwer, Dordrecht, The Netherlands, 1994), pp. 149-161.

[57] M. Séchaud, "Wave-front compensation devices," in *Adaptive Optics in Astronomy*, F. Roddier, ed. (Cambridge University Press, Cambridge, 1999), pp. 57-90.

[58] A. Quirrenbach, "Adaptive optics with lase guide stars: basic concepts and limitations," in *Laser Guide Star Adaptive Optics for Astronomy*, N. Ageorges and J. C. Dainty, eds. (Kluwer, Dordrecht, The Netherlands, 2000), pp. 23-50.

[59] R. Foy and A. Labeyrie, "Feasibility of adaptive telescope with laser probe," A. & A. **152**, L29-32 (1985).

[60] R. Foy, "The tilt problem - multiwavelength," in *Laser Guide Star Adaptive Optics for Astronomy*, N. Ageorges and J. C. Dainty, eds. (Kluwer, Dordrecht, The Netherlands, 2000), pp. 147-167.

[61] C. E. Max, "Laser guide star operational issues," in *Laser Guide Star Adaptive Optics for Astronomy*, N. Ageorges and J. C. Dainty, eds. (Kluwer, Dordrecht, The Netherlands, 2000), pp. 89-106.

[62] M. Le Louarn, R. Foy, N. Hubin and M. Tallon, "Laser guide star for 3.6 and 8-m telescopes: performance and astrophysical implications," Mon. Not. R. Astron. Soc. **295**, 756-768 (1998).

[63] M. Le Louarn, N. Hubin, M. Sarazin and A. Tokovinin, "New challenges for adaptive optics: extremely large telescopes," Mon. Not. R. Astron. Soc. **317**, 535-544 (2000).

[64] D. L. Fried, "Focus anisoplanatism in the limit of infinitely many artificial-guide-star reference spots," J. Opt. Soc. Am. A **12**, 939-949 (1995).

[65] R. Foy, "The cone effect," in *Laser Guide Star Adaptive Optics for Astronomy*, N. Ageorges and J. C. Dainty, eds. (Kluwer, Dordrecht, The Netherlands, 2000), pp. 107-123.

[66] E. Viard, M. Le Louarn and N. Hubin, "Adaptive optics with four laser guide stars: correction of the cone effect in large telescopes," Appl. Opt. **41**, 11-20 (2002).

[67] D. C. Johnston and B. M. Welsh, "Analysis of multiconjugate adaptive optics," J. Opt. Soc. Am. A **11**, 394-407 (1994).

[68] D. Bello, J. M. Conan, G. Rousset, and R. Ragazzoni, "Signal to noise ratio of layer-oriented measurements for multiconjugate adaptive optics," A. & A. **410**, 1101-1106 (2003).

[69] J. R. Fienup, "Reconstruction of an object from the modulus of its Fourier transform," Opt. Lett. **3**, 27-29 (1978).

[70] J. R. Fienup, "Phase retrieval algorithms: a comparison," Appl. Opt. **21**, 2758-2769 (1982).

[71] R. W. Gerchberg and W. O. Saxton, "A Practical algorithm for the determination of phase from image and diffraction plane picture," Optik **35**, 237-246 (1972).

[72] R. G. Lane, "Phase retrieval using conjugate gradient minimization," J. Mod. Opt. **38**, 1797-1813 (1991).

[73] J. R. Fienup and C. C. Wackerman, "Phase-retrieval stagnation problems and solutions," J. Opt. Soc. Am. A **3**, 1897-1907 (1986).

[74] R. A. Gonsalves, "Phase retrieval and diversity in adaptive optics", Opt. Eng. **21**, 829-832 (1982).

[75] R. G. Paxman and J. R. Fienup, "Optical misalignment sensing and image reconstruction using phase diversity," J. Opt. Soc. Am. A **5**, 914-923 (1988).

[76] W.K. Pratt, "Generalised Wiener filter computation techniques", IEEE Trans. Compt. **C-21**, 636-641 (1972).

[77] A. Rosenfeld and A.C. Kak, *Digital Picture Processing, Vol. 1*, 2nd edition, Academic Press Inc., New York (1982).

[78] J. M. Conan, L. M. Mugnier, T. Fusco, V. Michau, and G. Rousset, "Myopic deconvolution of adaptive optics images by use of object and point-spread function power spectra," Appl. Opt. **37**, 4614-4622 (1998).

[79] W. Y. V. Leung and R. G. Lane, "Post-processing of partially compensated imagery by recursive inverse filtering," Opt. Comms. **215**, 37-52 (2003).

[80] D. R. Gerwe, D. J. Lee and J. D. Barchers, "Supersampling multiframe blind deconvolution resolution enhancement of adaptive optics compensated imagery of low earth orbit satellites," Opt. Eng. **41**, 2238-2251 (2002).

[81] M. J. Northcott, "Performance estimation and system modeling", in *Adaptive Optics in Astronomy*, F. Roddier, ed. (Cambridge University Press, Cambridge, 1999), pp. 155-168.

[82] R. G. Lane, M. Tallon, E. Thiebaut, R. M. Clare, "Diffraction limited image restoration by post-compensation from simultaneous speckle and wavefront sensing observations," in *Adaptive optical system technologies II*, P. L. Wizinowich and D. Bonaccini, eds., Proc. SPIE **4839**, 1142-1153 (2002).

[83] S. Altarac, M. Tallon, E. Thiébaut and R. Foy, "Speckle interferometry. Data acquisition and control for the SPID instrument," IEEE Trans. Nucl. Sci. **45**, 2057-2061 (1998).

[84] W.-Y.V. Leung, M. Tallon and R.G. Lane, "Centroid estimation by model-fitting from undersampled wavefront sensing images," Opt. Comms. **201**, 11-20 (2001).

[85] W.-Y.V. Leung, R. M. Clare and R.G. Lane, "Blind deconvolution of speckle images constrained by wavefront sensing data," in *Image reconstruction from incomplete data II*, P. J. Bones, M. A. Fiddy and R. P. Millane, eds., Proc. SPIE **4792**, 44-55 (2002).

[86] M.C. Roggemann, B.M. Welsh and J. Devey, "Biased estimators and object-spectrum estimation in the method of deconvolution from wavefront sensing," Appl. Opt. (33), 5754-5763 (1994).

[87] B. L. Ellerbroek and D. W. Tyler, "Adaptive optics sky coverage calculations for the Gemini-North telescope," Pub. Ast. Soc. Pac. **110**, 165-185 (1998).

[88] I. S. Gradshteyn and I. M. Ryzhik, *Table of Integrals Series and Products*, Academic Press, New York (1965).

[89] B. M. Welsh and C. S. Gardner, "Performance analysis of adaptive-optics systems using laser guide stars and slope sensors," J. Opt. Soc. Am. A **6**, 1913-1923 (1989).

[90] R. G. Lane and R. Irwan, "Phase retrieval as a means of wavefront sensing," in *Proceedings of the International Conference on Image Processing*, B. R. Hunt and R. M. Gray, eds. (IEEE Computer Society Press, Los Alamitos, Calif., 1997), pp. 242-245.

[91] R. C. Cannon, "Global wave-front reconstruction using Shack-Hartmann sensors," J. Opt. Soc. Am. A **12**, 2031-2039 (1995).

[92] M. C. Roggemann, T. J. Schulz and C. W. Ngai, "Joint processing of Hartmann sensor and conventional image measurements to estimate large aberrations: theory and experimental results," Appl. Opt. **38**, 2249-55 (1999).

[93] T. Takahashi and H. Takajo, "Global wavefront reconstruction from its intensity distribution in the focal plane and Shack-Hartmann sensor images," Opt. Eng. **38**, 1960-64 (1999).

[94] M. A. van Dam and R. G. Lane, "Theoretical performance of phase retrieval on a subdivided aperture," Opt. Eng. **41**, 1387-1395 (2002).

[95] R. Irwan and R. G. Lane, "Phase Retrieval with prior information," J. Opt. Soc. Am. A **15**, 2302-2311 (1998).